

VOLUME I  
LABORATORY MODEL DEVELOPMENT

NASA CR-144917

(NASA-CR-144917-Vol-1) ANNULAR MOMENTUM  
CONTROL DEVICE (AMCD) . VOLUME 1: LABORATORY  
MODEL DEVELOPMENT Final Report (Ball Bros.  
Research Corp.) 108 p HC \$5.50 CSCL 131  
N76-19457  
Unclas  
G3/37 20655

---

FINAL REPORT

**ANNULAR MOMENTUM CONTROL DEVICE  
(AMCD)**

PREPARED FOR

NATIONAL AERONAUTICS AND SPACE ADMINISTRATION  
LANGLEY RESEARCH CENTER  
HAMPTON, VIRGINIA



Aerospace Division  
BOULDER, COLORADO 80302



F76-02

NASA CR-144917

FINAL REPORT

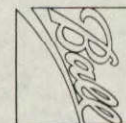
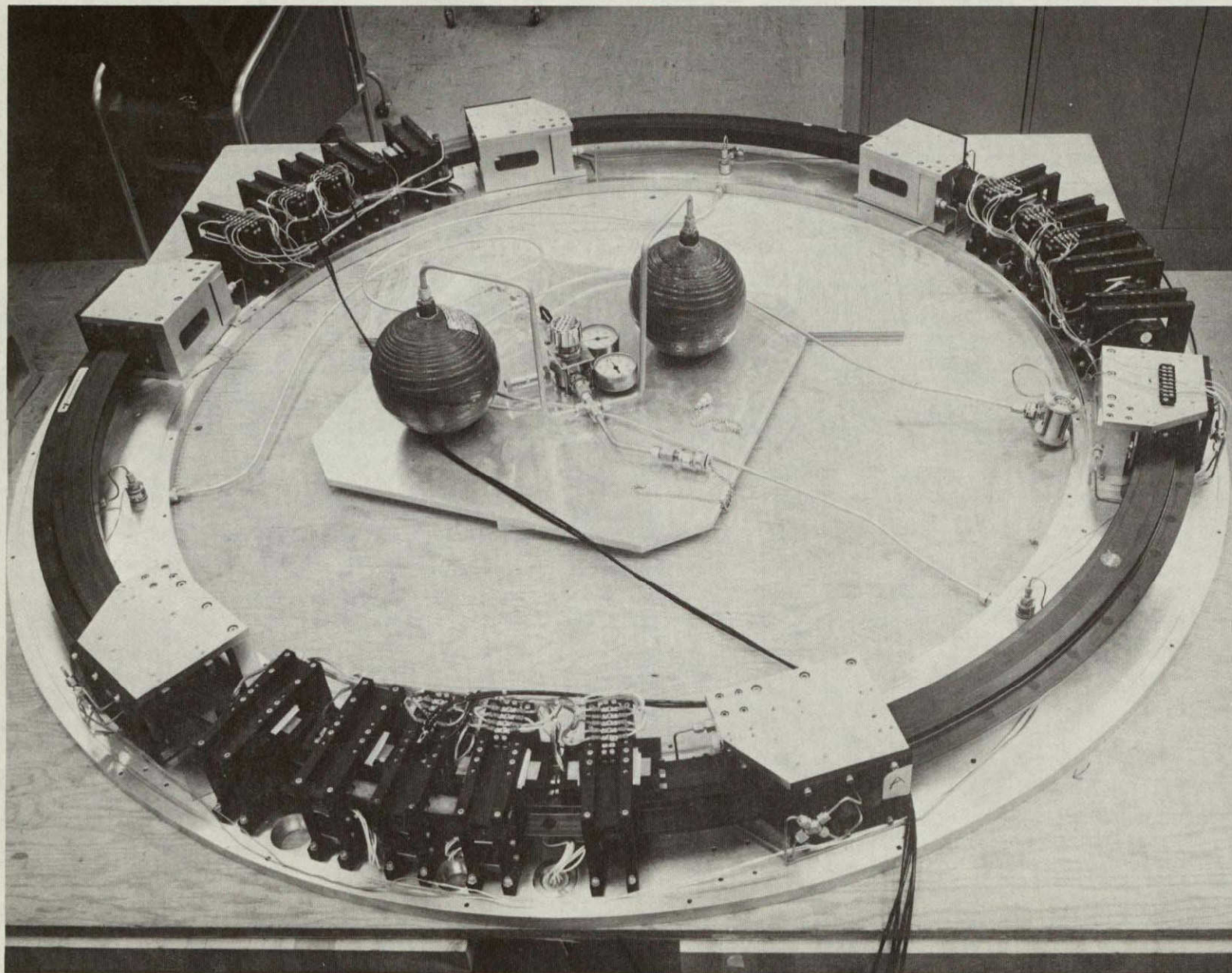
ANNULAR MOMENTUM CONTROL DEVICE (AMCD)

VOLUME I: LABORATORY MODEL DEVELOPMENT

Prepared under Contract No. NAS 1-12529 by  
Ball Brothers Research Corporation  
Boulder, Colorado 80302

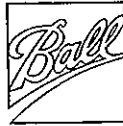
for

NATIONAL AERONAUTICS AND SPACE ADMINISTRATION



F76-02

The AMCD in Final Stages of Assembly



## SUMMARY

The annular momentum control device (AMCD) is a thin hoop-like wheel with neither shaft nor spokes (see Frontispiece). The wheel floats in a magnetic field and can be rotated by a segmented motor. Potential advantages of such a wheel are low weight, configuration flexibility, a wheel that stiffens with increased speed, vibration isolation, and increased reliability.

The AMCD is nearly 2 meters (6 feet) in diameter. An annular aluminum baseplate supports the entire wheel assembly. Vacuum operation is possible by enclosing the wheel in an annular housing attached to the baseplate. The rotor or "rim" has a diameter of about 1.6 meters (63 inches) and consists principally of graphite-epoxy composite material. It weighs 22.5 kilograms (49.5 pounds) and is strong enough to be spun at 3000 rpm. At this speed, it can store 2200 N-m-s (3000 ft-lb-sec) of angular momentum. A system of pneumatic bearings can support the rim in the event of a magnetic suspension failure.

The magnetic suspension system supports the rim both axially and radially at three points. Combinations of permanent magnets and electromagnets at each of the three suspension stations exert forces on ferrite bands imbedded in the rotating rim. The magnetic gaps are about 0.25 cm (0.1 inch) above, below, and inside the rim. The gaps are maintained by servo loops with 50 hertz bandwidths that respond to error signals generated by inductive sensors. The servo loops can be operated in either "positioning" or "zero-power" modes.

The rim is accelerated and decelerated by a large diameter, segmented, brushless d.c. motor. Electromagnet stator segments are placed at each suspension station and interact with samarium cobalt permanent magnets placed every 7.3 cm (2.9 inches) along the periphery of the rim. Commutation is achieved by Hall sensors that detect the passing permanent magnets.



Volume I of this report describes the analysis, design, fabrication, and testing of the laboratory model of the AMCD. Volume II contains a conceptual design and set of dynamic equations of a gimbaled AMCD adapted to a Large Space Telescope (LST). Such a system could provide maneuver capability and precision pointing by means of one external gimbal, wheel speed control, and small motions of the rim within the magnetic gap.

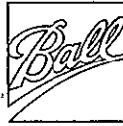


## TABLE OF CONTENTS

| <u>Section</u> |                                | <u>Page</u> |
|----------------|--------------------------------|-------------|
|                | SUMMARY                        | ii          |
|                | ACKNOWLEDGMENTS                | v           |
| 1.0            | INTRODUCTION                   | 1-1         |
| 2.0            | THE AMCD CONCEPT               | 2-1         |
| 3.0            | MECHANICAL SYSTEMS             | 3-1         |
|                | 3.1 Rim                        | 3-1         |
|                | 3.2 Back-Up Air Bearing System | 3-17        |
| 4.0            | SUSPENSION SYSTEM              | 4-1         |
|                | 4.1 System Description         | 4-1         |
|                | 4.2 Performance                | 4-12        |
| 5.0            | DRIVE SYSTEM                   | 5-1         |
|                | 5.1 System Description         | 5-1         |
|                | 5.2 Magnet Selection           | 5-1         |
|                | 5.3 Core and Winding Design    | 5-2         |
|                | 5.4 Motor Commutation          | 5-3         |
|                | 5.5 Motor Control Electronics  | 5-3         |
|                | 5.6 Torque Calculations        | 5-4         |

## APPENDICES

| <u>Appendix</u> |   | <u>Page</u> |
|-----------------|---|-------------|
| A               | CURRENT DRIVER EQUATIONS AND TRANSFER FUNCTIONS | A-1         |
| B               | THE WAHOO CONCEPT                               | B-1         |
| C               | SOME ADDITIONAL SERVO INSIGHTS                  | C-1         |



## ACKNOWLEDGMENTS

The AMCD development to date has been the result of the efforts of a great many people. At BBRC, Frank Manders with help from Dick Mathews lead the mechanical design and fabrication effort, Dick Woolley strongly influenced the magnetic design and overall configuration, Jerry Wedlake developed the drive system, Glen King performed the dynamic analyses and Dave Giandinoto designed much of the interfacing electronics and did the final system integration.

At Cambion, Paul Simpson managed the magnetic suspension work with technical consulting provided by Joe Lyman and Lloyd Perper.

The rim fabrication at Bristol was headed by Tom Laidlaw with analytical assistance from Keith Kedward.

Analytic design of the back-up bearings at Shaker Research was conducted by Dr. Coda Pan and Warren Waldron.

The "customer" had a strong influence on the final system. At Goddard Space Flight Center, Phil Studer provided valuable suggestions on all magnetic aspects and the drive motor in particular. The primary influences and directions came, of course, from Nelson Groom and Dr. Willard Anderson of Langley Research Center who conceived of the AMCD and fostered its development.

My thanks to all of these people.

Carl Henrikson  
AMCD Project Manager



## 1.0 INTRODUCTION

The AMCD concept was originated at the Langley Research Center of the National Aeronautics and Space Administration (Reference 1). Analysis, design, fabrication, and testing of development hardware was begun under contract to Ball Brothers Research Corporation in July of 1973. The contract was jointly sponsored by the Langley Research Center and the Goddard Spaceflight Center. The contract work statement was also a joint effort with the Goddard Spaceflight Center providing technical inputs on the magnetic bearings and drive motor portions. Hardware was delivered in February of 1975.

Several key subcontractors were used by BBRC during the program. Principal among these were:

1. Cambridge Thermionic Corporation (Cambion), Cambridge, Massachusetts - Development of the magnetic suspension system.
2. Bristol Aerospace Limited, Winnipeg, Canada - Analysis and fabrication of the rim.
3. Shaker Research Corporation, Ballston Lake, New York - Design of the back-up air-bearing system.

These subcontractors performed well and made major contributions to the success of the program. One subcontract did not go well and caused a major delay in the program. Failure of the subcontractor for the baseplate and vacuum enclosure to meet flatness requirements necessitated rejection of the parts and placement of the subcontract with another firm.

This report is a description of the major hardware items and their design considerations. Details of the "as-delivered" hardware may be found in the Operations and Maintenance Manual that was delivered with the hardware.





The report is divided into four main parts covering the concept, the mechanical systems, the suspension system, and the drive system. Appendices are used to cover some of the details of the servo control loops.



## 2.0 THE AMCD CONCEPT

A purely annular wheel has many advantages. Principal among these is that all the rotating mass is at the greatest radius and hence can produce the greatest angular momentum storage. The shaft and spokes of a conventional wheel add weight but very little angular momentum storage.

Ball-bearing annular wheels have never been tried and for one obvious reason: The losses associated with a large diameter ball bearing would be intolerable. In order to make annular wheels practical, a low-loss magnetic suspension of the rotor (or rim) is necessary. This, then, is the AMCD concept: a narrow, annular rim supported by a magnetic suspension system.

Several other advantages accrue from the AMCD concept. First of all, conventional size constraints are removed. The wheel does not have to operate in an enclosure to preserve lubricants. If the diameter is increased greatly, the space is not wasted because a spacecraft or part of a spacecraft can be placed inside the wheel. Furthermore, motivation exists to go to larger wheels. It can be shown that for a given stress level in the rim, the mass efficiency of the rim increases as the diameter increases. The offsetting effects of increased stator weight can be alleviated by using basic spacecraft structure to support the stator elements. A further advantage of larger diameter is increased moment arm for spin and precessional torquing.

Another set of advantages of the AMCD concept is a result of the relatively thin annular rim. The stresses in such a shape are predominantly circumferential so that the structure lends itself to filament or tape wound composite materials. Furthermore, as spin rate increases, the rim tends to flatten and reduce dynamic imbalance. Also, it tends to become "stiffer" so that structural



resonant frequencies increase. In fact, it can be shown that the conventional crossover frequency of a spinning wheel at which the spin frequency becomes equal to the rotor structural frequency cannot occur for an AMCD. The structural frequencies are always greater than spin frequency no matter how limber the rim is at zero spin rate.

The use of a magnetic suspension gives rise to another set of advantages. First, the suspension is relatively soft and forms a sort of isolator between the rim and the spacecraft to which it is attached. Any vibrations of the rim will be greatly attenuated. This effect can be enhanced by proper filtering at multiples of spin rate. The suspension is also a smooth, linear force-producing system without mechanical nonlinearities such as stiction. The result is that small, precision precessional torques can be created by gimbaling the rim in the magnetic gaps. The final advantage is related to the long life and, perhaps even more important, predictable long-life capability of a magnetic suspension system vis-a-vis a ball bearing. Ball bearing lifetimes are short, dependent on number of revolutions, rotational speed, and very susceptible to contamination. The lifetime of a magnetic suspension is a function of the failure rate of electronic components, an area that has been the subject of a great deal of study. Moreover, redundant suspensions are fairly simple to mechanize.



### 3.0 MECHANICAL SYSTEMS

The AMCD Mechanical Systems consist of 1) the rotor (or "rim"), 2) the back-up air bearing system and 3) the mounting base and vacuum enclosure.

The rim provides the angular momentum storage capability for the system. Embedded into the rim are ferrite rings and samarium cobalt permanent magnets. Three ferrite rings, composed of segments, located on each axial surface and on the inside radial surface react with the magnetic suspension system. Seventy-two permanent magnets, located near the periphery of the rim react with the segmented drive system.

The back-up air bearing system, initiated in the event of a magnetic suspension failure, is designed to slow and support the rim. The design provides hydrostatic air pads for radial control and hydrodynamic air pads for axial control.

The mounting base and vacuum enclosure completely surround the rim, magnetic suspension and motor components, and provide the mounting points for the torque measuring fixture brackets. The annular mounting base supports the magnetic suspension and motor lattice structure. The annular vacuum enclosure, U-shaped in cross-section, is bolted to the mounting base providing the capability to operate the rim in a vacuum and to add structural rigidity. The vacuum environment is necessary to reduce rim air drag.

#### 3.1 Rim

The final rim configuration, Figure 3-1 shows that all components embedded into the rim are completely supported. The distance between the permanent magnets and ferrite bands is maximized within the dimensional constraints of the rim.

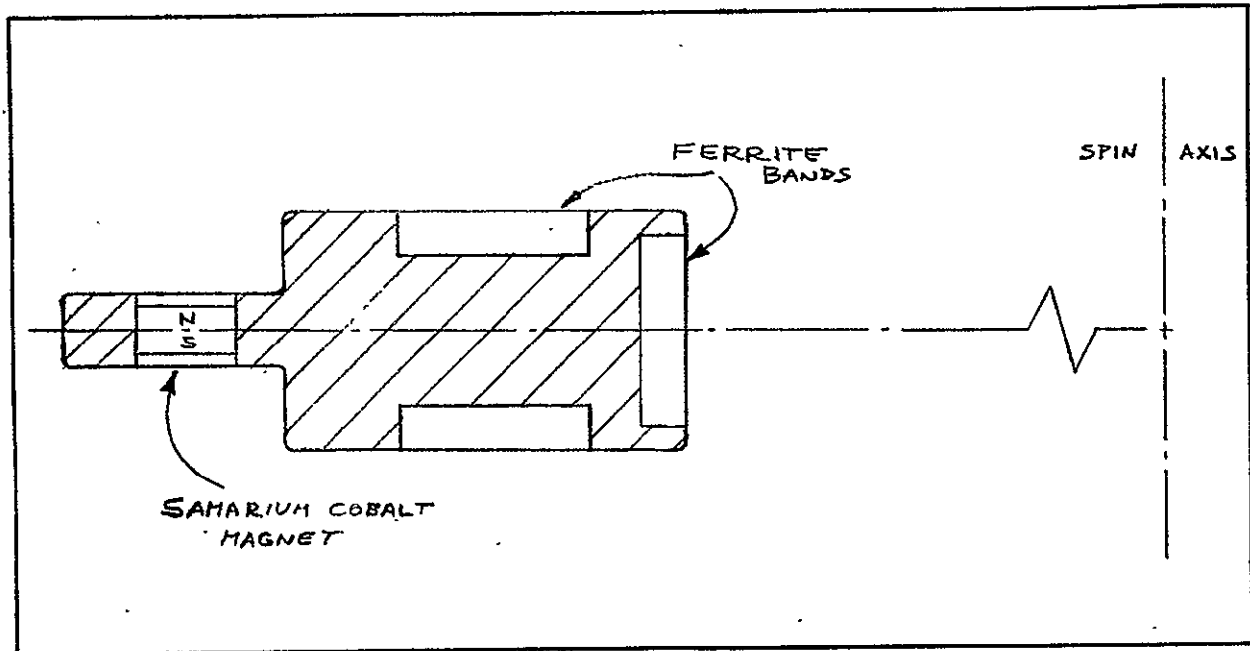


Figure 3-1 Rim Configuration

"Centrifugal" accelerations cause forces on the embedded components which are reacted directly by the base rim material minimizing the stresses on the adhesive which bonds the components to the rim. The samarium cobalt permanent magnets are spaced a minimum of 0.85 inches from the closest ferrite band to minimize the coupling between the permanent magnets and the magnetic suspension system.

The primary function of the rim is to provide maximum angular momentum storage capacity within dimensional and weight constraints. The selection of the rim material, graphite filament - epoxy laminate, is consistent with this function. The specific momentum of a flywheel ( $H/M$ ) is related to material characteristics of the rim as follows:

$$H/M \propto \sqrt{\sigma/\rho} \quad (3-1)$$



where  $\sigma$  is working stress in flywheel

$\rho$  is flywheel material density

Hence, a high-strength, low-density material is ideal for a low-weight flywheel.

Table 3-1 shows the relationship of material ultimate tensile strength to material density for acceptable rim materials.

Table 3-1  
RIM MATERIAL STRENGTH TO DENSITY RATIO

| <u>MATERIAL</u>     | <u>STRENGTH/DENSITY (IN <math>\times 10^6</math>)</u> |
|---------------------|---|
| Graphite A-S/Epoxy  | 3.6   |
| Glass/Epoxy         | 3.4   |
| Boron/Epoxy         | 3.1   |
| Graphite M-S/Epoxy  | 3.0   |
| Graphite HM-S/Epoxy | 1.8   |
| Beryllium*          | 1.0   |
| 6Al-4V Titanium*    | 1.0   |
| 7075 Aluminum*      | 0.8   |

\*Not in Composite Form

Graphite AS fiber - epoxy laminate, therefore, will provide the largest specific momentum for the system. Graphite filament-epoxy laminate also has a relatively high elastic modulus ( $16 \times 10^6$  PSI), thus providing relatively low radial growth at high speeds. Furthermore, graphite-epoxy laminate is non-magnetic and non-conducting, essential characteristics for low drag operation of the magnetic suspension system.



### 3.1.1 Rim Description

The rim consists of three bands of ferrite material, made up of 180 segments each, and 72 samarium cobalt permanent magnets embedded and bonded into the AS graphite filament - DX210 epoxy rim material. Figure 3-2 shows the rim dimensions.

The ferrite rings and permanent magnets are bonded to the basic rim with Fuller 7004 adhesive. The rim is composed of two basic rectangular cross-sections, the first, and larger, contains the bulk of the graphite-epoxy material and the ferrite bands; the second, smaller, section contains the remaining material and the samarium cobalt permanent magnets.

The larger section has a cross-section 5.3 cm (2.1 inches) in radial length by 3.18 cm (1.25 inches) deep, with an inner diameter of 154 cm (60.8 inches). Three channels are machined into this section 2.54 cm (1.0 inches) wide by 0.57 cm (0.225 inches) deep, to contain the ferrite bands. The smaller section, integral with the larger, is axially centered, 2.8 cm (1.1 inches) in radial length by 0.95 cm (0.375 inches) deep, with an outer diameter of 171 cm (67.25 inches). This section contains 72 holes which contain the permanent magnets.

The samarium cobalt permanent magnets are 1.4 cm (0.55 inches) in diameter by 0.64 cm (0.25 inches) long. The axial and radial ferrite segments are shown in Figures 3-3 and 3-4, respectively.

The ferrite segments are machined from Ferroxcube 3C5 material. The axial segment is slightly keystone in shape to minimize gap distances. Each segment occupies 2 degrees of the band circumference.

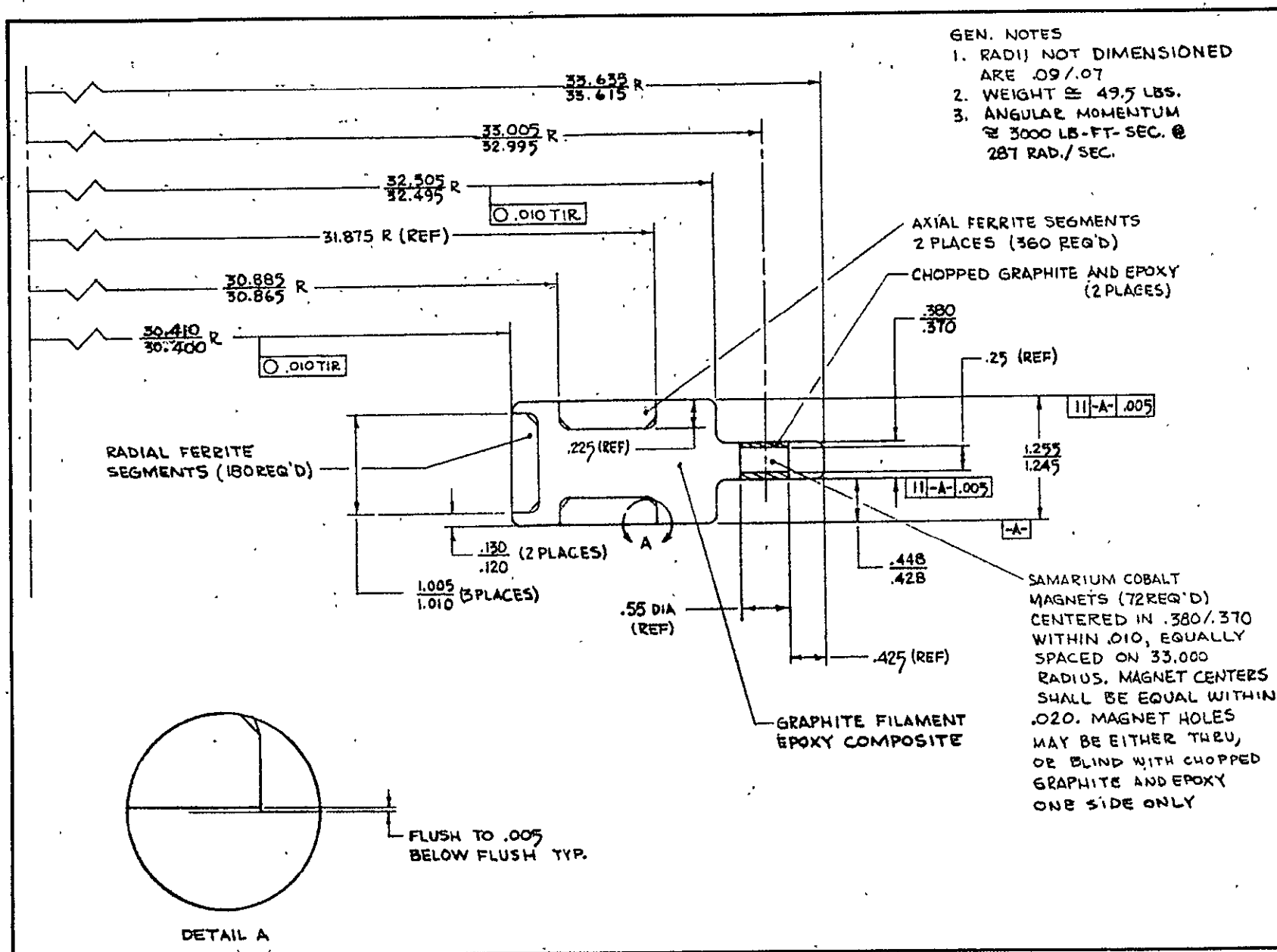


Figure 3-2 Rim Dimensions



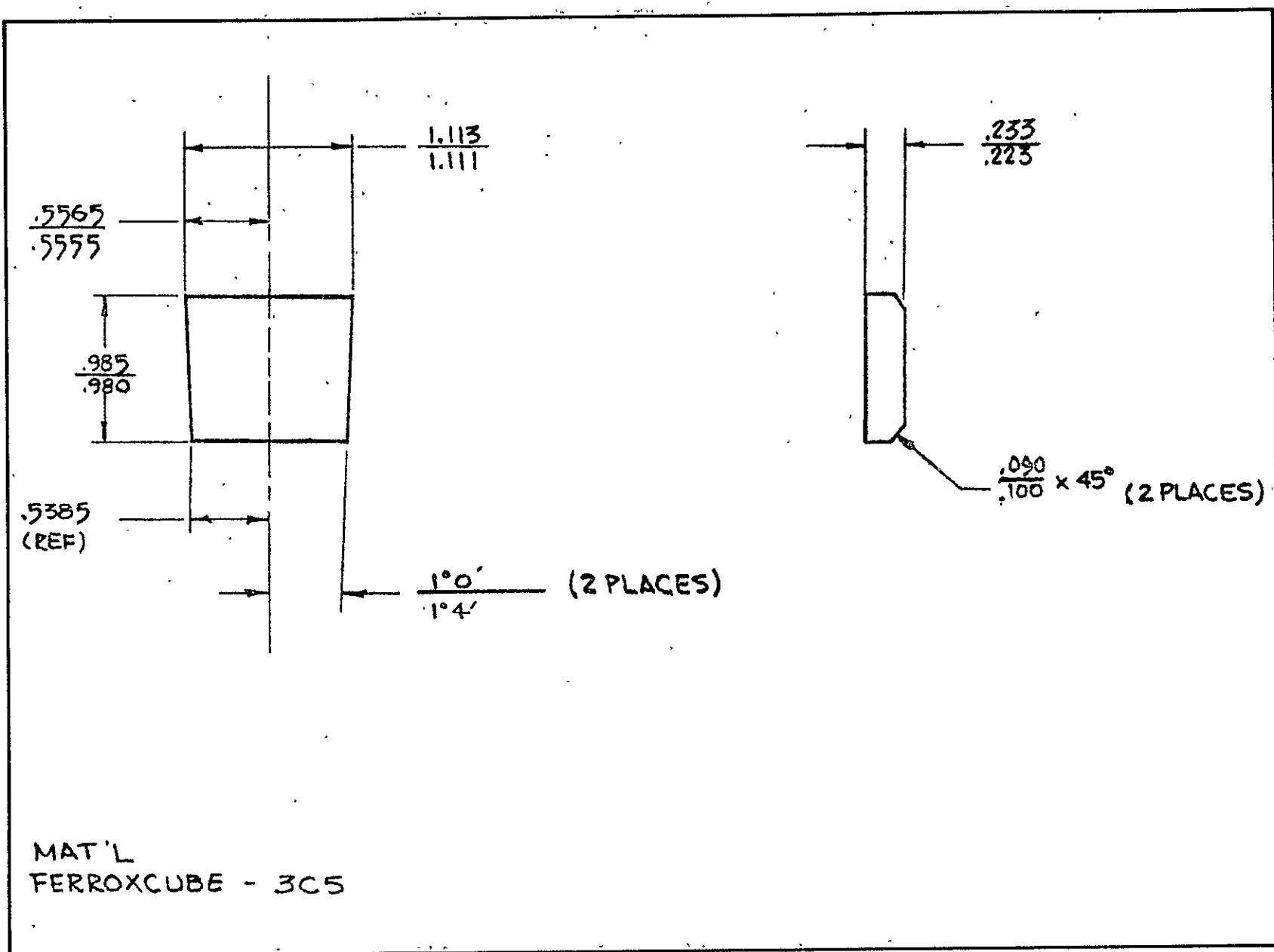
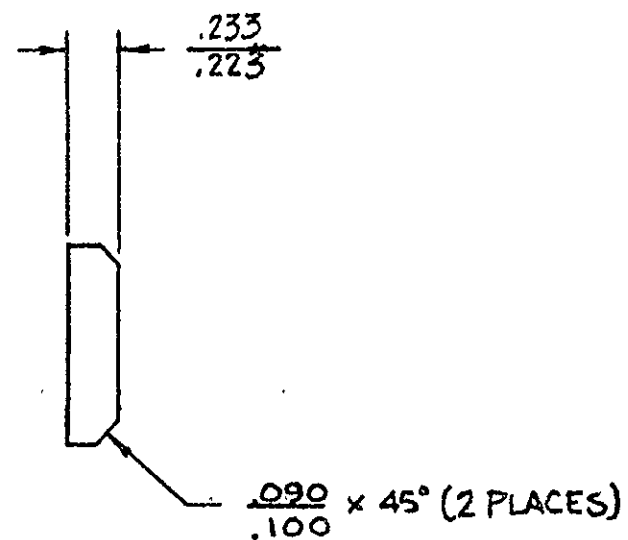
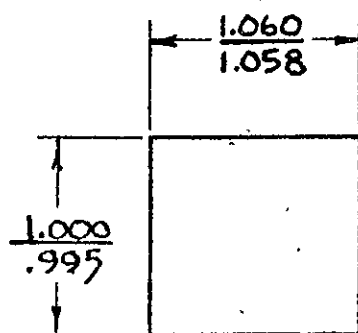


Figure 3-3 Axial Ferrite Segment



MAT'L  
FERROXUBE - 3CS



F76-02

Figure 3-4 Radial Ferrite Segment.

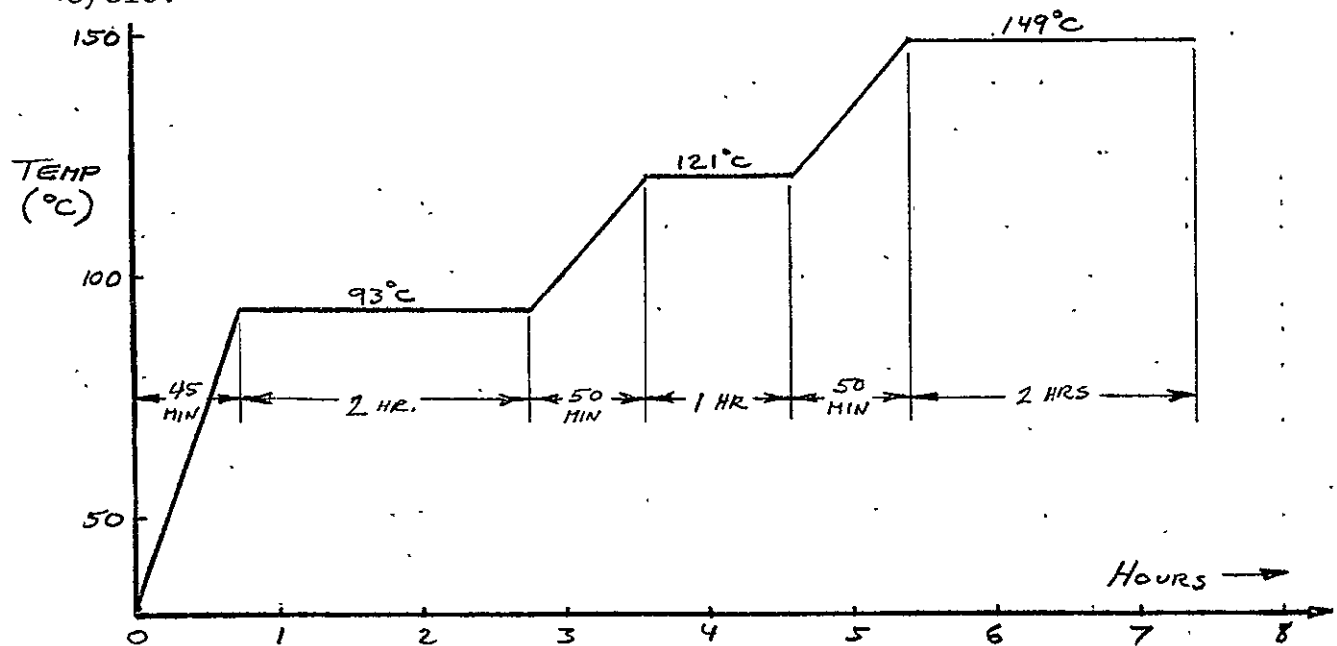


The radial segment is rectangular in cross-section and when bonded in place produces a small wedge-shaped gap between segments. Each radial segment represents 2 degrees of the band circumference.

### 3.1.2 Rim Fabrication

The AMCD rim was fabricated by Bristol Aerospace Limited, Winnipeg, Canada. The material, AS graphite filament tape impregnated with DX210 resin, was wrapped on a special tool producing 100 percent circumferential fibers with a volume fraction of graphite of 55 percent.

The oversized cross-section rim was wound in 15 separate layers. Each layer was "B" stage cured with the following temperature cycle.



The post cure, after the fifteenth layer, was identical to the "B" stage cure except, the temperature was increased to 177°C in 50 minutes and held at 177°C for 2 hours after the 149°C exposure.



Figure 3-5 shows the specially constructed tool, containing heaters and insulation for "B" stage and final cure cycles.

The rim was removed from the tool and machined to nearly the final dimensions including ferrite channels and permanent magnet holes. These operations are shown in Figures 3-6 and 3-7.

The ferrite segments and magnets were bonded in place with Fuller 7004 adhesive and cured. The magnets were placed in the rim with alternating North-South poles and the ends were covered with a 0.16 cm (1/16 inch) thickness of chopped AS graphite-DX210 resin and cured. After final cure, the rim was machined (by grinding) to final dimension. The rim was coated with a 0.005 cm (0.002 inch) thick layer of Fuller 7220 adhesive as a final step to minimize rim water absorption. Figure 3-7A shows the final rim results.

### 3.1.3 Rim Analysis

The rim analysis, conducted by Bristol Aerospace, predicted the rim maximum stress and radial growth to be  $38,250 \text{ N/cm}^2$  (55,434 PSI) and .3 cm (0.117 inches), respectively.

The rim was modelled using axisymmetric finite elements using the ANSYS system. The model characterizes the heterogeneity of the structure (including the ferrite bands and magnets) and the orthotropic elastic properties of the graphite-epoxy composite.

The results of the analysis are summarized in Table 3-2 and in Figures 3-8, 3-9 and 3-10 at a rim speed of 366 meters per second (1200 feet per second).



F76-02

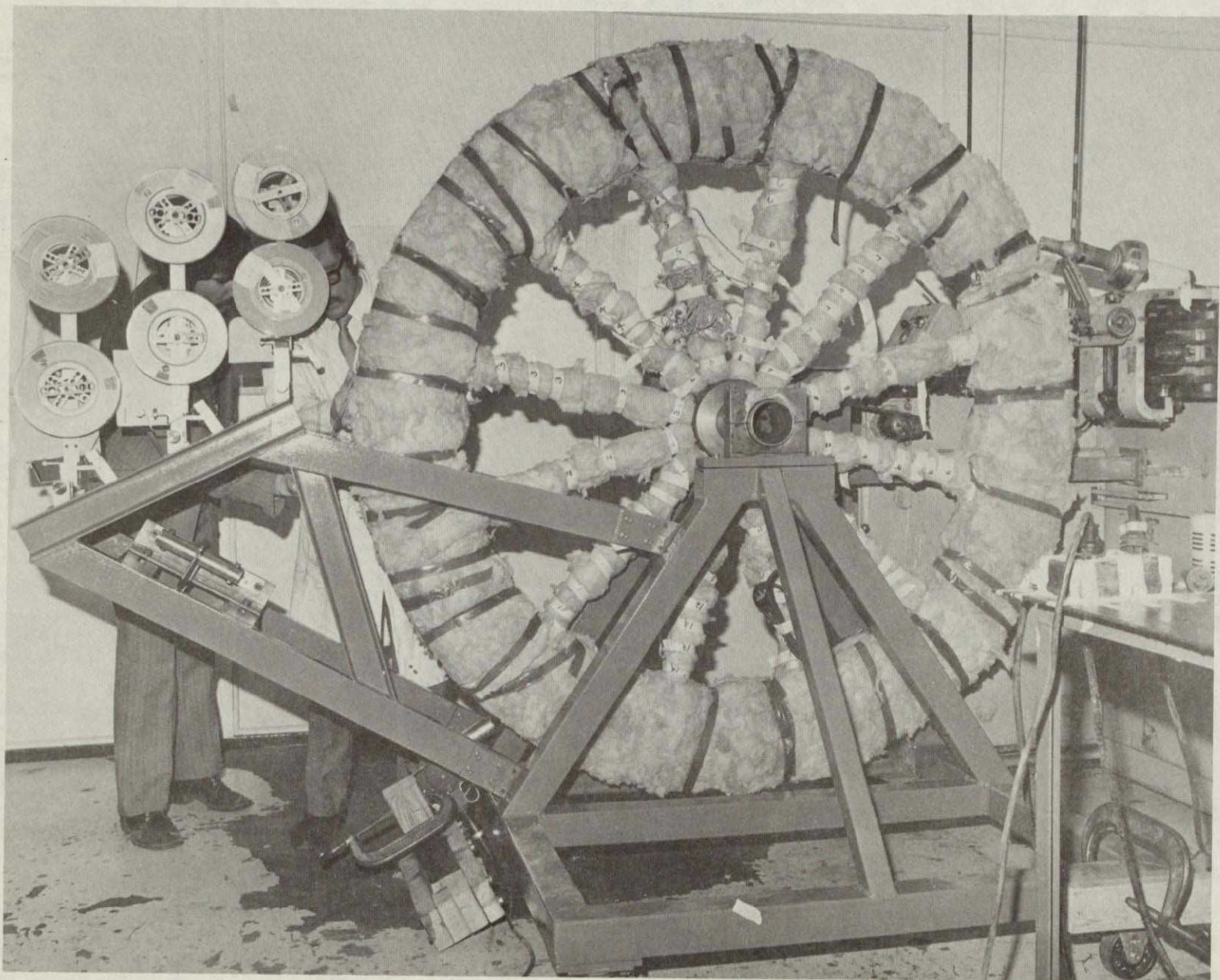


Figure 3-5 Lay-up Tool

ORIGINAL PAGE IS  
OF POOR QUALITY





F76-02

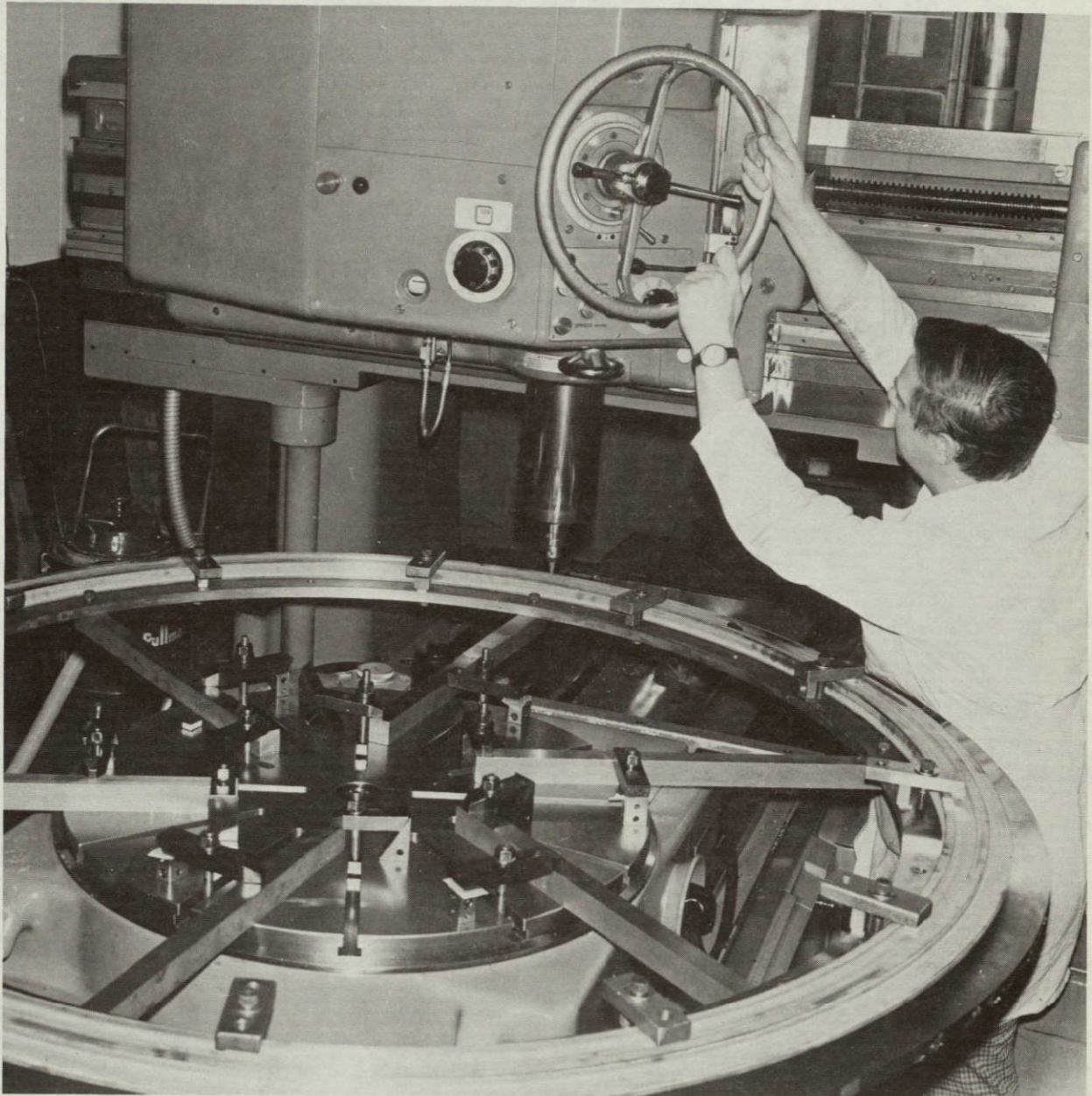


Figure 3-6 Rim Machining Operations





F76-02

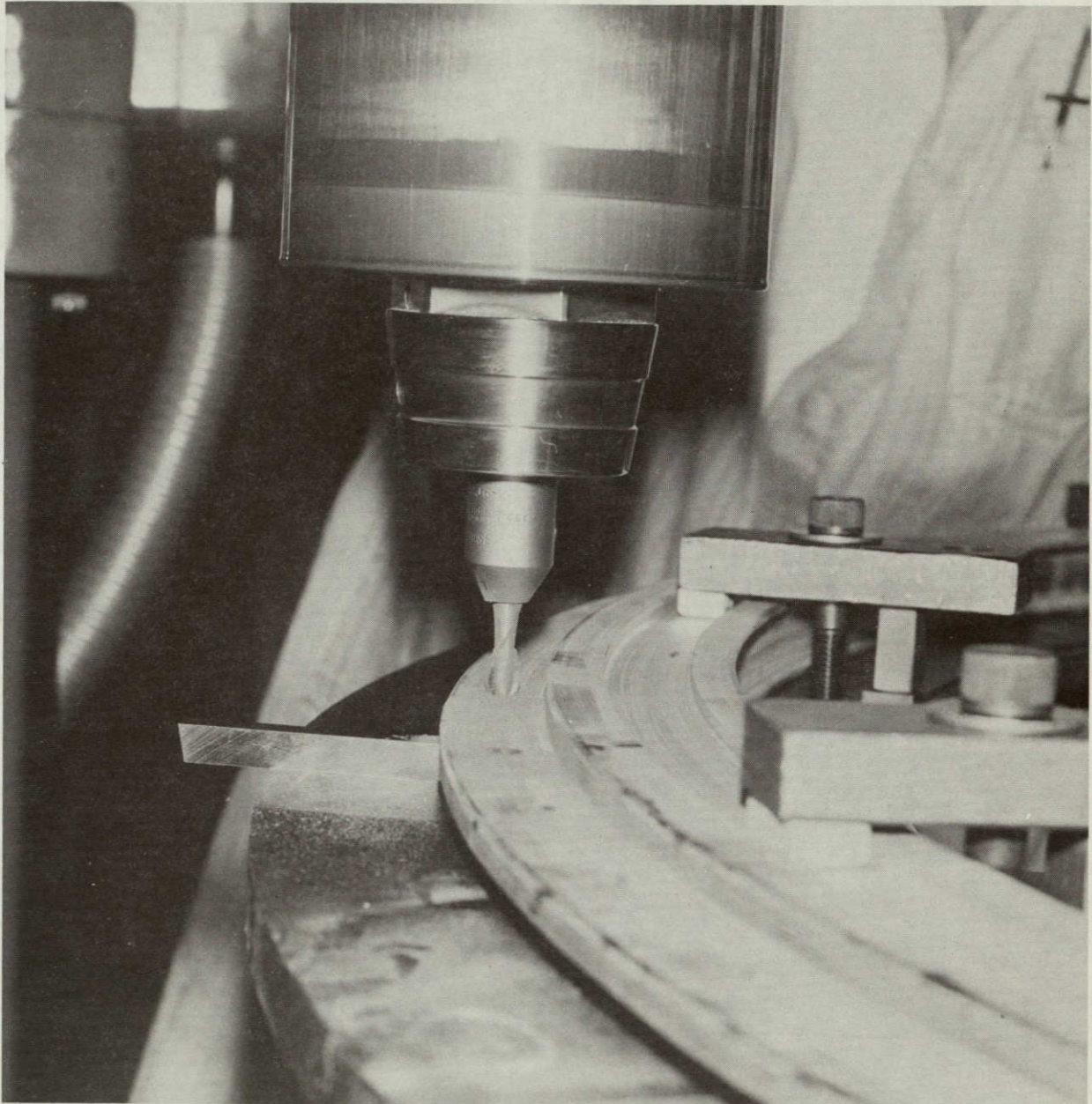


Figure 3-7 Drilling Permanent Magnet Holes in the Rim



| STRESS COMPONENT             | LOCATION                       | MAGNITUDE (PSI)                |
|------------------------------|--------------------------------|--------------------------------|
| Radial or 'X' stress         | carbon/epoxy<br>"              | +460 (max)*<br>-891 (min)      |
| Axial or 'Y' stress          | carbon/epoxy<br>"              | +491 (max)*<br>-433 (min)      |
| Shear or 'XY' stress         | carbon/epoxy<br>"              | +390 (max)<br>-176 (min)       |
| Hoop or 'Z' stress           | carbon/epoxy<br>"              | +55,434 (max)<br>0 (min)       |
| Radial Displacement (inches) | inner surface<br>outer surface | +0.1166 (max)<br>-0.1130 (min) |

Table 3-2

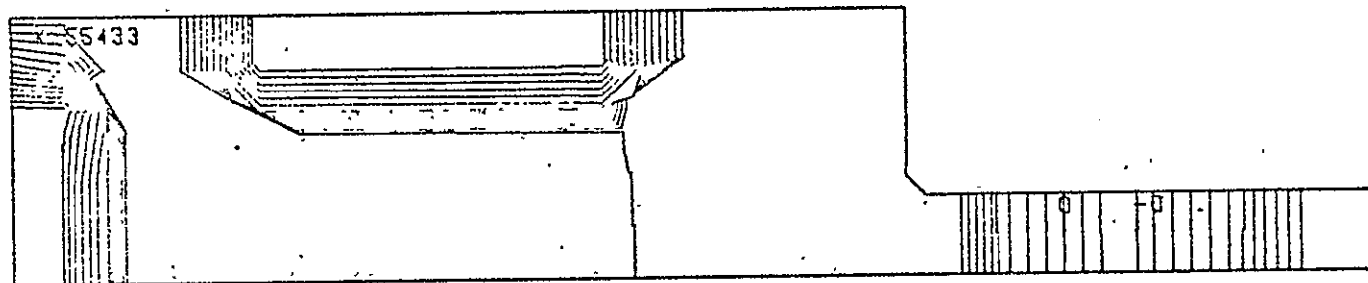
MAXIMUM VALUES OF STRESS/DISPLACEMENT  
AT 1200 FT/SEC. RIM SPEED



STEP=

ITERATION= 1

4000.00



AMCO ANALYSIS BRISTOL AEROSPACE LTD. OCT. 73

HOOP STRESS ANSYS 5

Figure 3-8 'Z' or Hoop Stress Contour Plot



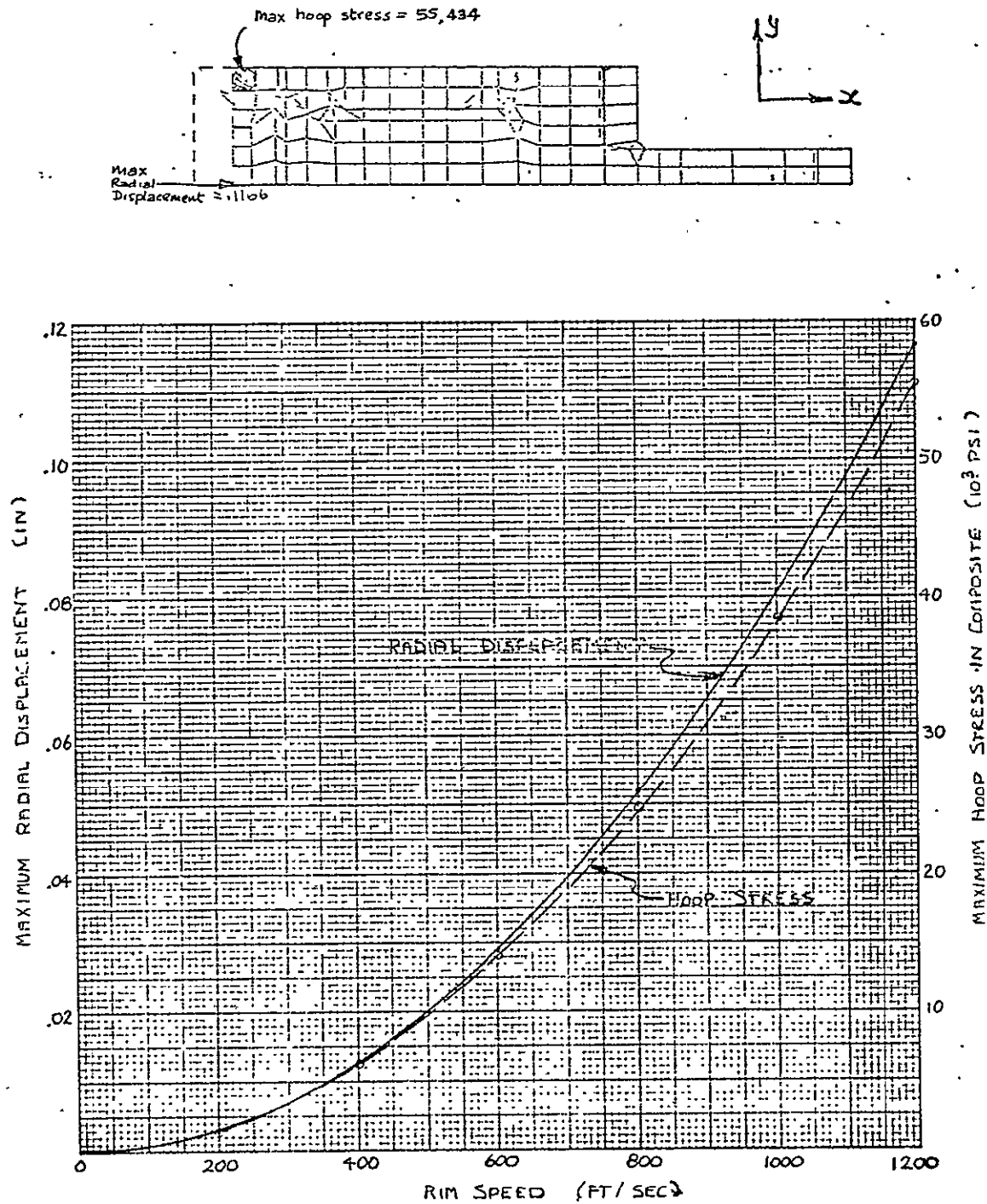
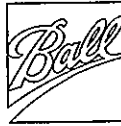


Figure 3-9 Hoop Stress and Growth With Speed

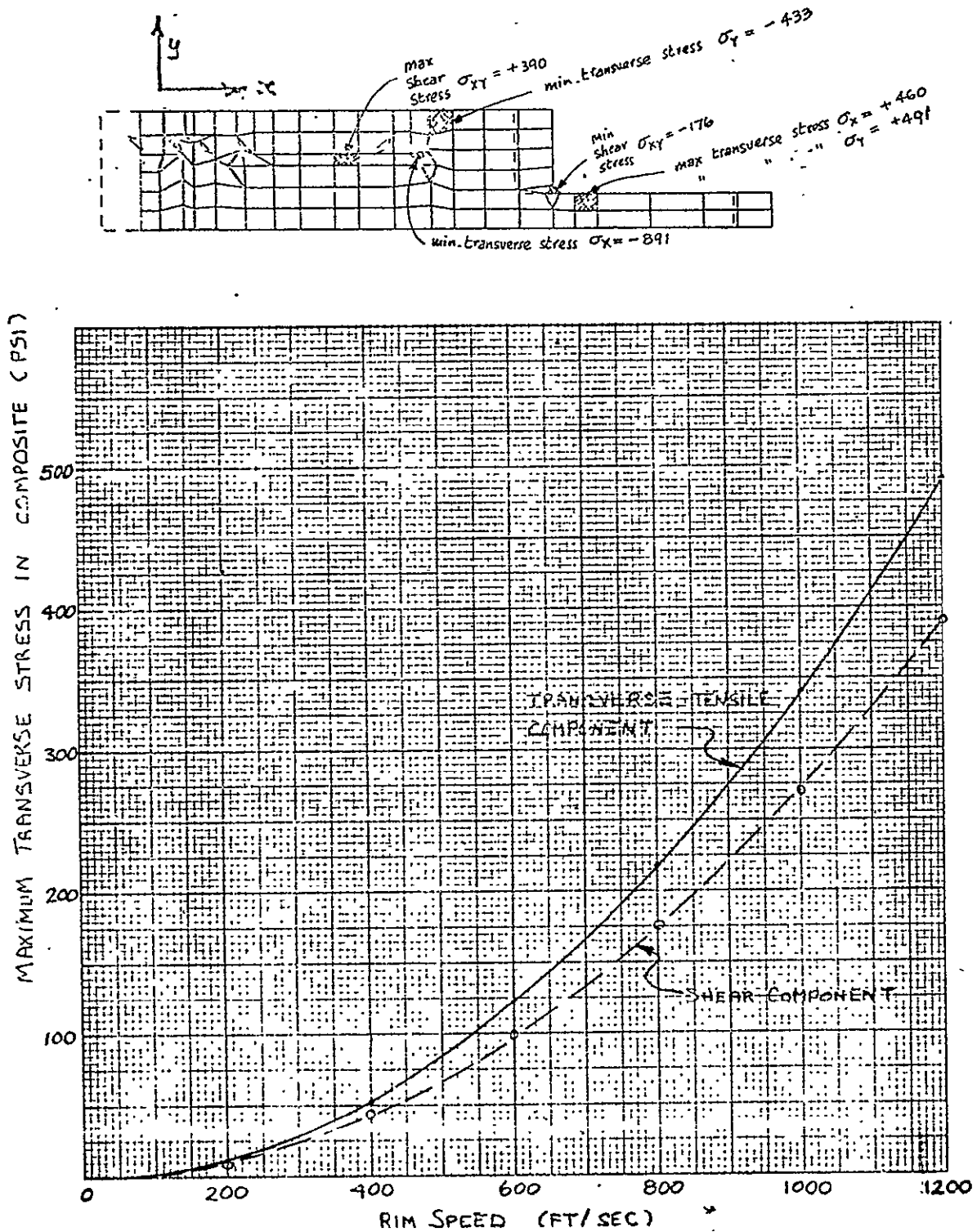


Figure 3-10. Transverse Stress Components With Speed



Figure 3-8 shows the computer-drawn plot of constant hoop tensile stress contours, the maximum being  $38,252 \text{ N/cm}^2$  (55,438 PSI) occurring at the top and bottom inside corner.

Figure 3-9 shows the relationship of radial growth and hoop stress as a function of rim tip speed.

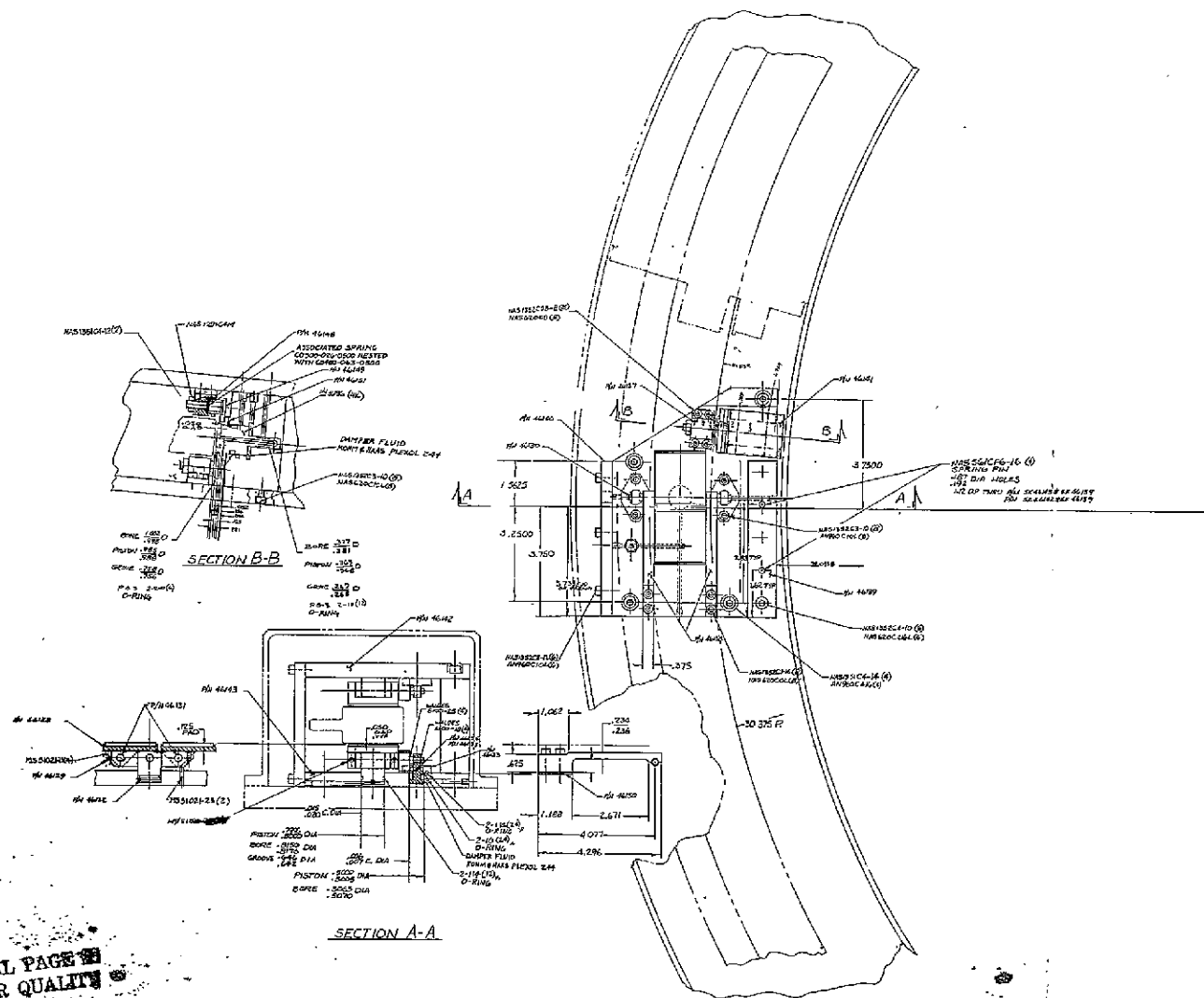
Figure 3-10 shows the relationship of transverse stress components with speed.

Since the material, void free, is capable of withstanding  $110,400 \text{ N/cm}^2$  (160,000 PSI) in tension and  $8280 \text{ N/cm}^2$  (12,000 PSI) in shear, the safety factor is 2.8 minimum. On a sample basis, the void fraction was determined to be less than 0.4 percent.

### 3.2: Back-Up Air Bearing System

The design of the back-up air bearing system was completed and analyzed by Shaker Research Corporation, Ballston Lake, New York.

The back-up air bearing (BUB) system consists of six hydro-static radial pads and twelve hydrodynamic axial pads. These are arranged in six BUB sets consisting of two axial (one upper and one lower) and one radial pad and located at either end of a magnetic support station. Each BUB set is approximately 60 degrees from the adjacent set. The bearings are deployed toward the rim by air pressure when predetermined rim displacement limits are exceeded. The introduction of air through the pads as well as through a pneumatically operated valve in the vacuum enclosure provides the fluid for the BUB system and also introduces air drag for a faster coast-down. Hydrostatic bearings were selected for radial use instead of hydrodynamic types because the rather small rim depth (1.25 inches) allows insufficient area to produce the required reaction forces. The back-up bearing system is shown in Figures 3-11 and 3-12.



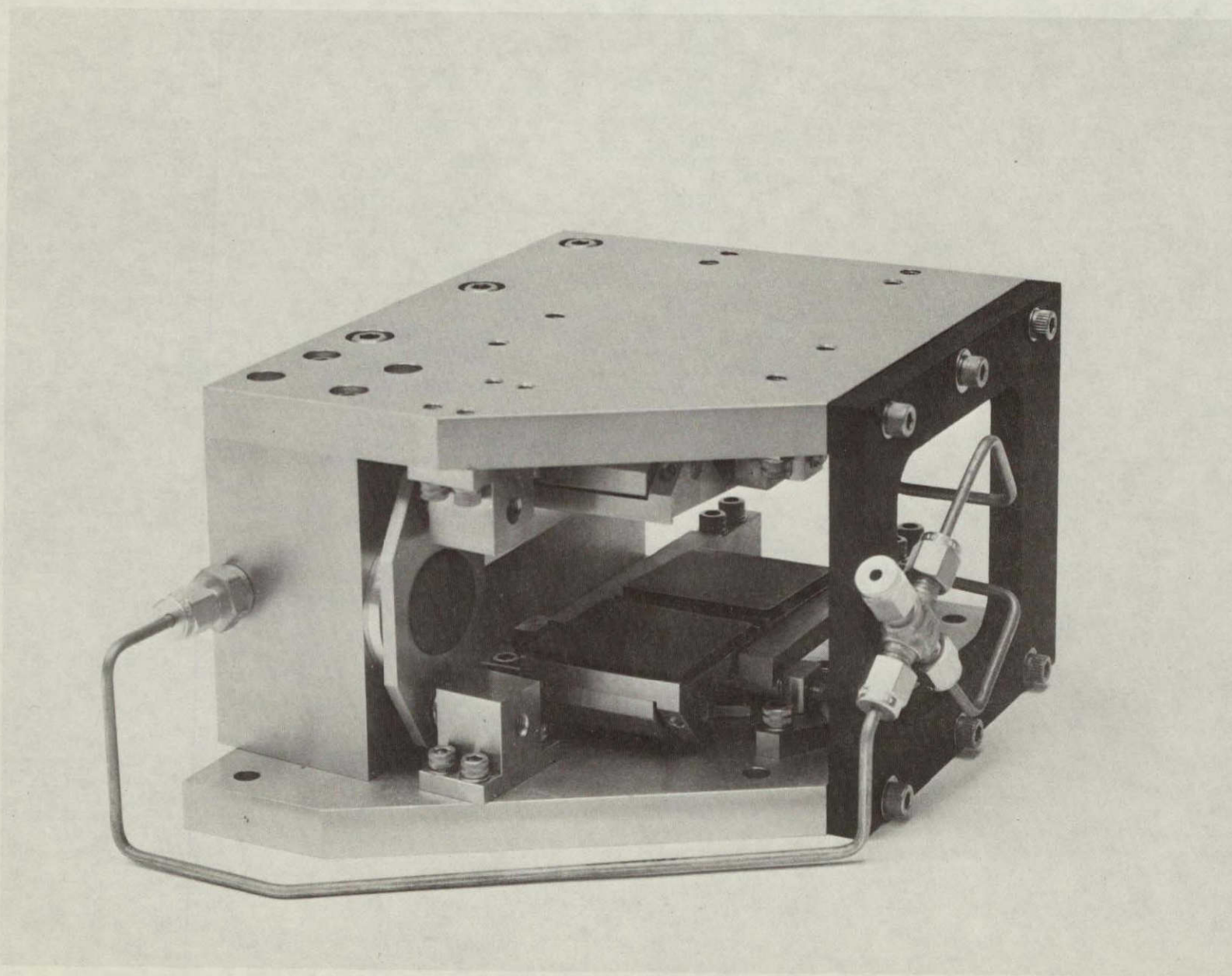


Figure 12 Back-Up Bearing System



F76-02



### 3.2.1 Hydrostatic Radial Bearings

The movable radial pads are designed to minimize air flow and maximize air bearing rim reaction forces. The radial pads provide a centering effect on the rim to minimize dynamic and magnetic unbalance forces.

In the normal magnetic suspension mode, the radial pads are held away from the rim and against stops by a set of nested compression springs (total of 22 N (5.0 pounds) of preload). When the radial system, Figure 3-11, is activated, 207 N/cm<sup>2</sup> (300 psig) air is introduced to the pad piston cylinder, which moves the pad outward toward the rim. The piston chamber is ported to the pad surface through a 0.033 cm (0.012 to 0.014 inch) diameter orifice. A sealed, oil-filled dashpot between the piston and pad controls the deployment velocity.

Figure 3-13 shows the relationship between radial pad force and gas flow versus film thickness for various orifice diameters. Because of limited gas available, the smaller orifice diameters were selected.

Since the rim is not at constant radius (because of radial growths), film thickness and flow vary with rim speed. Figure 3-14 shows the relationship of film thickness and flow versus rim speed.

### 3.2.2 Hydrodynamic Axial Bearings

Movable, tilt type, axial hydrodynamic pads were used since the rim radial width is large and because of the limited bearing air supply. The axial pads are slightly crowned and combined with the tilt feature are self aligning.

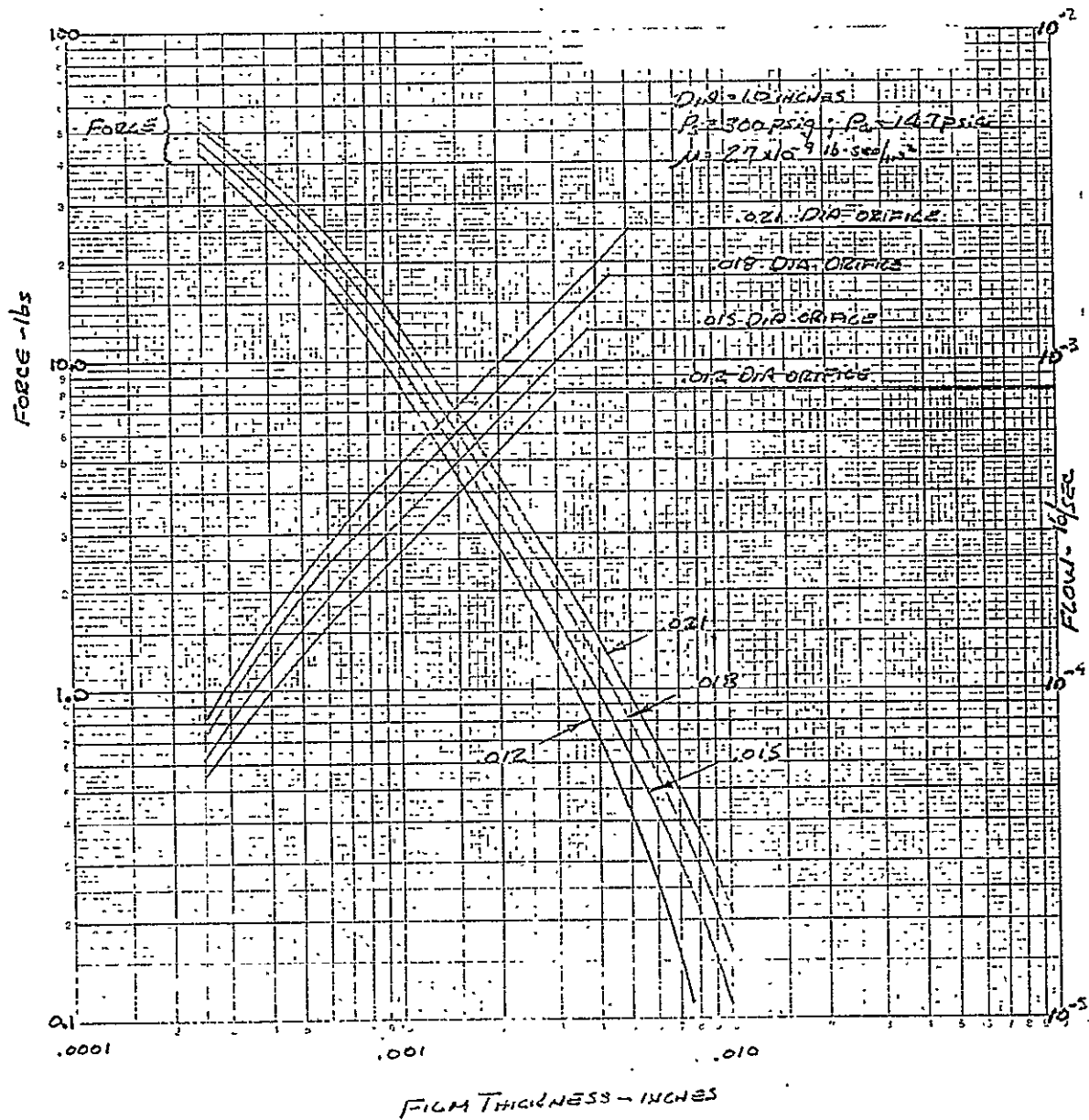


Figure 3-13 Single Pad Force and Flow



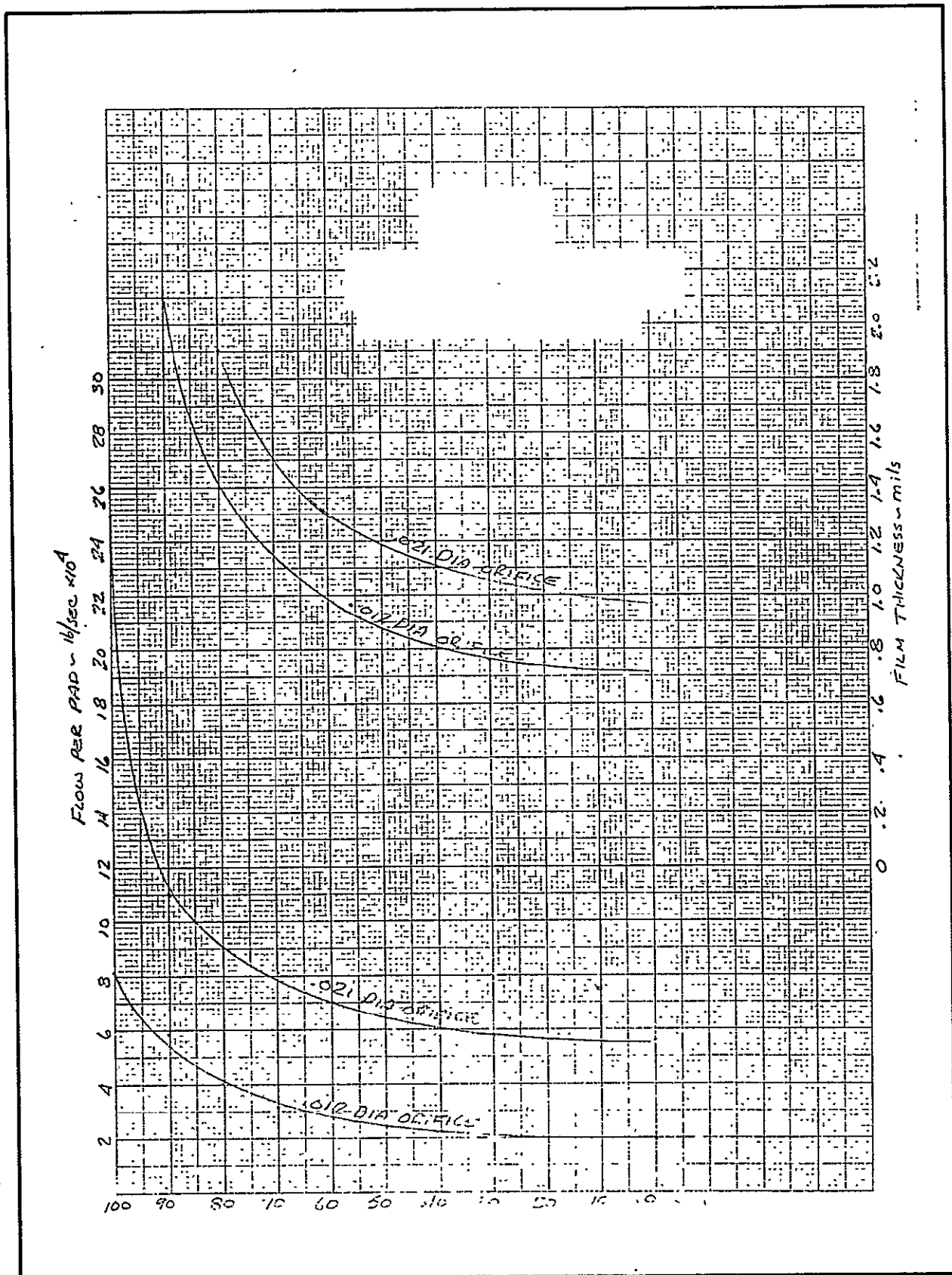


Figure 3-14 Radial Air Pad Flow and Film Thickness With Rim Centered



In the normal magnetic suspension mode, the axial pads are held against stops by a flexural spring. The axial system is deployed in much the same manner as the radial system. When a magnetic suspension anomaly is detected, the vacuum enclosure is flooded with external air thus providing the film for the axial bearings.

Figure 3-15, shows the relationship of film thickness with rim speed. Since the film will support the rim to about 15 radians per second, the pads are designed to accept several contacts before replacement is necessary.

### 3.2.3 Back-Up Bearing Pads

The primary objective in designing the pad material was to provide a material which would wear smoothly without damage to the rim or to the pad itself. Sacrificial bearing materials have been used in gas bearings in the past which exhibit the necessary qualities. The material used in the back-up bearings is an epoxy resin heavily filled with aluminum powder, aluminum oxide powder and molybdenum disulphide powder. The mixture is poured into silicone rubber molds, degassed in a vacuum chamber, then heat-cured. The pads are then machined.

When the spinning rim contacts the pads the pad will wear smoothly and rapidly, acquiring a high polish and yielding a fine dust. The rim surface should be undamaged by the contact. The aluminum filler provides high thermal conductivity to sink the heat generated by the rim contact. The aluminum oxide provides dimensional stability so the pad will withstand the thermal shock generated by the rim contact.

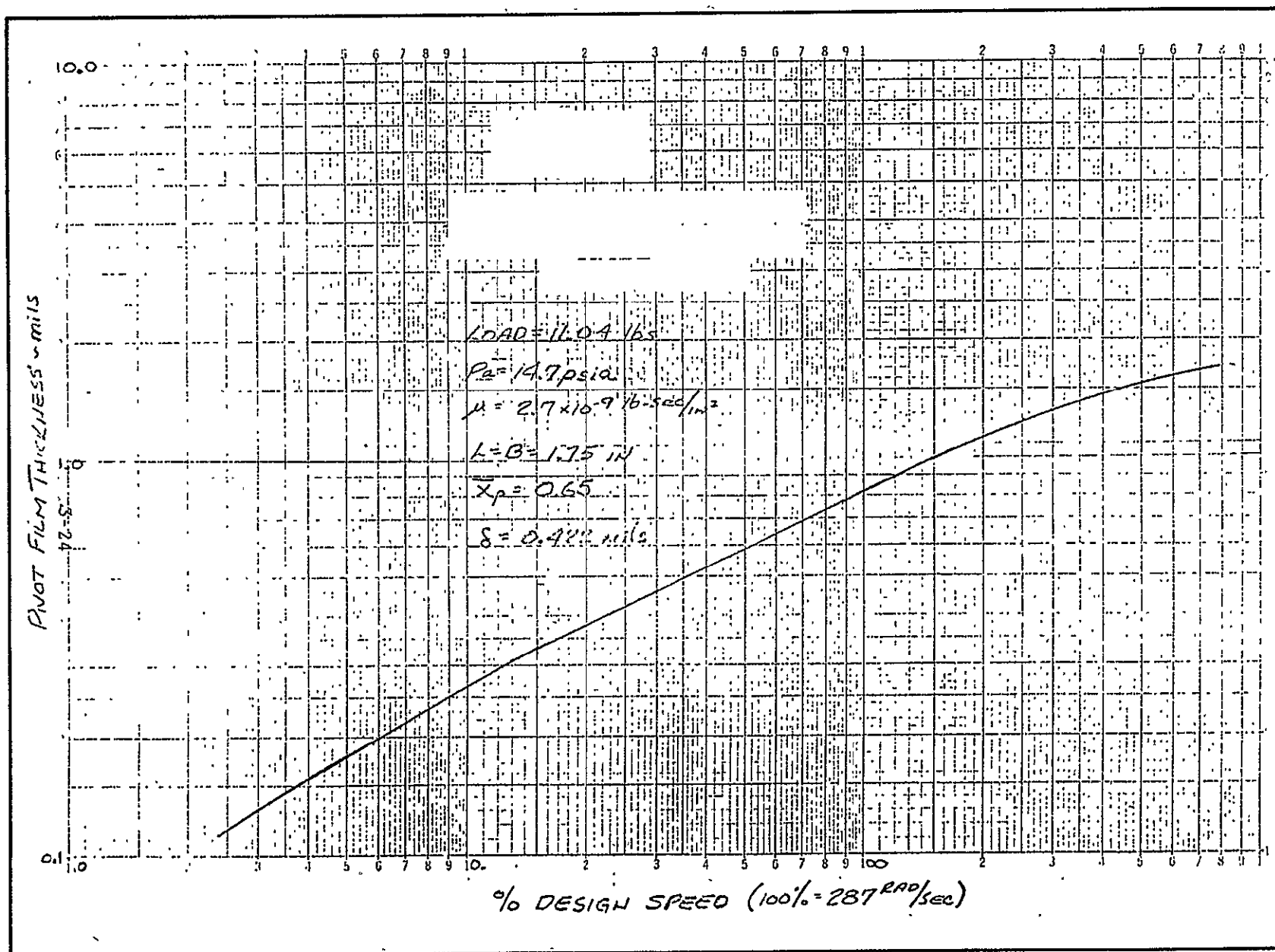


Figure 3-15 Axial Pad Film Thickness Versus Speed



## 4.0 SUSPENSION SYSTEM

### 4.1 System Description

The suspension system consists of three suspension stations placed symmetrically about the rim. At each suspension station, the rim can be pulled in either axial direction or radially inward by magnets. A total of 12 magnets are arranged in sets of four each to pull in these three directions (up, down, and inward). The eight axial magnets are driven in concert by one set of electronics. Axial error signals are developed by a position sensor located at the center of each station. The axial servo loops in each of the three stations are independent of each other. The four radial magnets in each station are also driven by a set of electronics in response to a radial position sensor located in the center of that station. But, the radial servos are interconnected from one station to another so as to prevent the servos fighting one another even in the presence of rim radial growth.

#### 4.1.1 Magnet Description

One of the unique features of the AMCD is the support magnet design. The electromagnets are flux-biased by thin wafers of samarium cobalt permanent magnet material placed in series in the magnetic circuit. This has the advantage of (1) providing a high force per unit current sensitivity at zero current, (2) providing a linear relationship between force and current, and (3) providing the static field required for zero power operation.

The support magnet geometry is seen in Figure 4-1. The permanent magnet biasing is achieved by slanted wafers of samarium cobalt in the legs. The wafers are as thin and wide as possible to

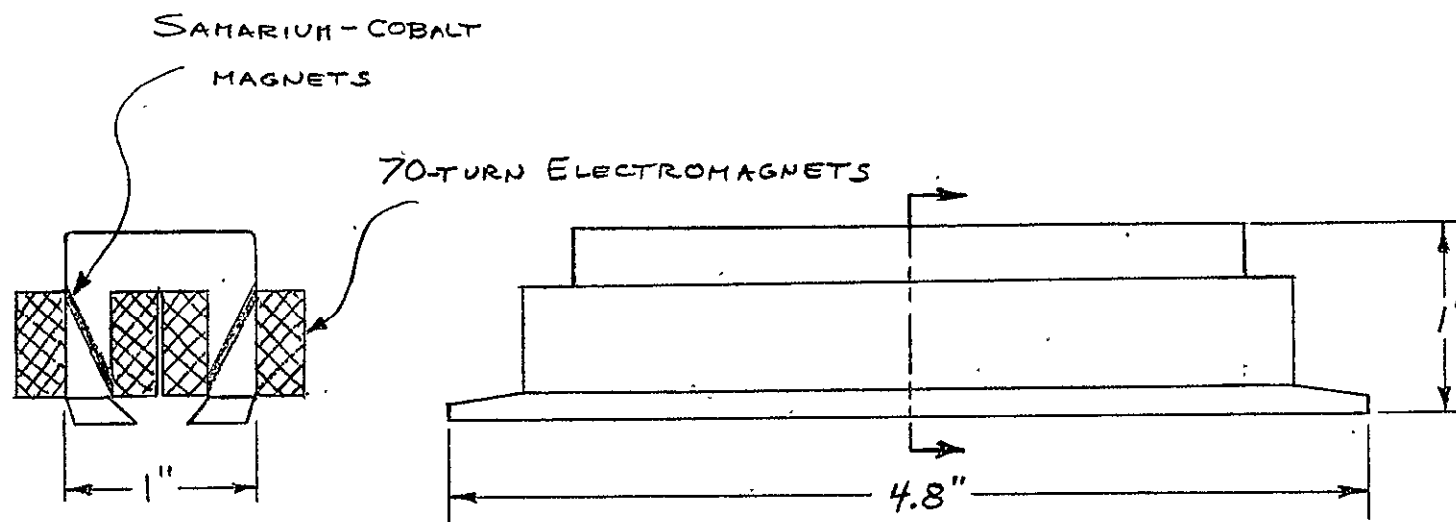
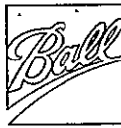


Figure 4-1 Support Magnet Geometry



minimize their reluctance in the magnetic circuit.. The volume of permanent magnet material is sufficient, however, to provide adequate flux-biasing and static lift. The reluctance of the permanent magnets is large but does not more than double the total reluctance since the air gap in this system is large. In many other magnet suspension systems, the gaps are small (about 0.1 mm) and this sort of series flux biasing would greatly increase the total reluctance in the circuit. Control power would thus be large and the systems would be impractical.

The effect of flux-biasing on the force versus current characteristics of the magnets is shown in Figure 4-2. With no biasing, current in either direction produces force of the same sign, with poor "gain" and low efficiency in the vicinity of zero current. Force is simply a function of the square of the current. With biasing, the slope of force versus current is greatly increased at zero current. In the AMCD, top and bottom magnets operate together in a push-pull type of operation. The coils are in series, hence both coils have zero current at the same time. The resultant force-current relationship is linear and has a slope double that of either magnet alone.

Figure 4-3 shows the "U" core of the magnet with the permanent magnets in place. Permanent magnet thickness is 1 mm (0.040 inches). Also shown in Figure 4-3 is a fully assembled magnet ready for potting. After potting, the units measure 4.3 cm x 10.7 cm x 2.5 cm (1.7 in x 4.2 in x .99 in) and weigh 500 grams (1.1 lbs.).

#### 4.1.2 Position Sensors

The position sensors used in both the axial and radial suspension systems are "Multi-vit" sensors manufactured by Kaman Sciences

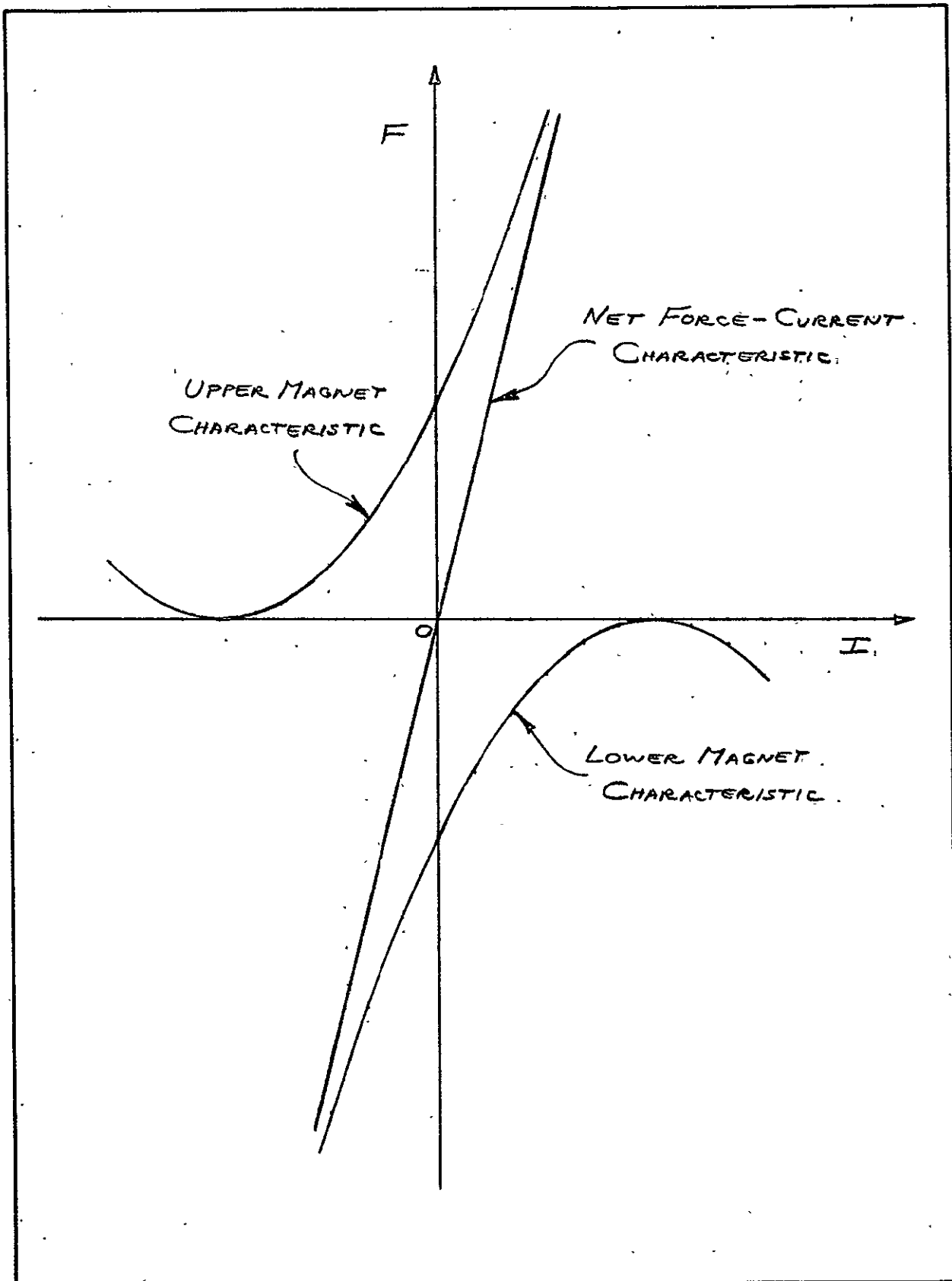


Figure 4-2 Flux-Biased Magnets in Push-Pull Operation



F76-02

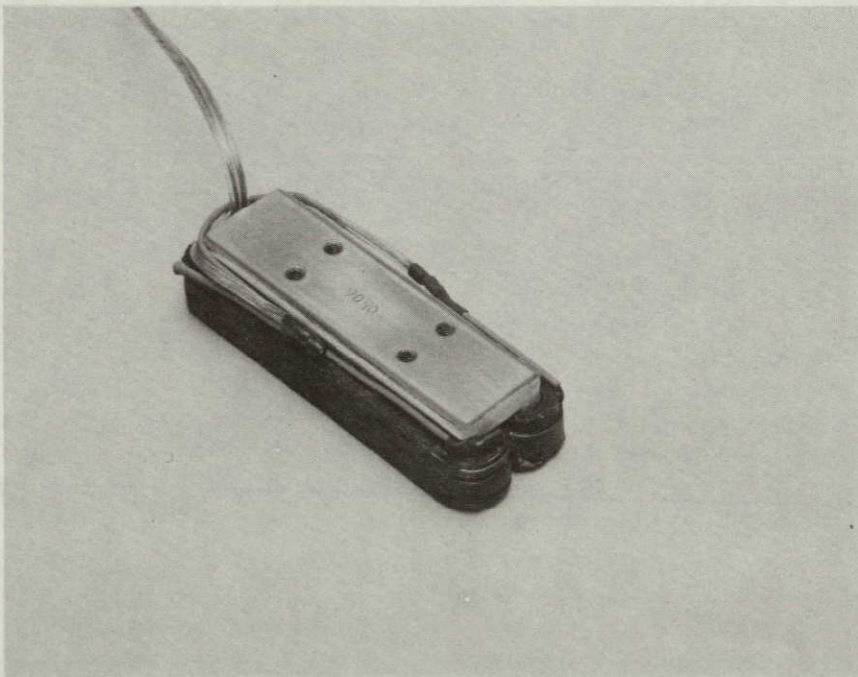
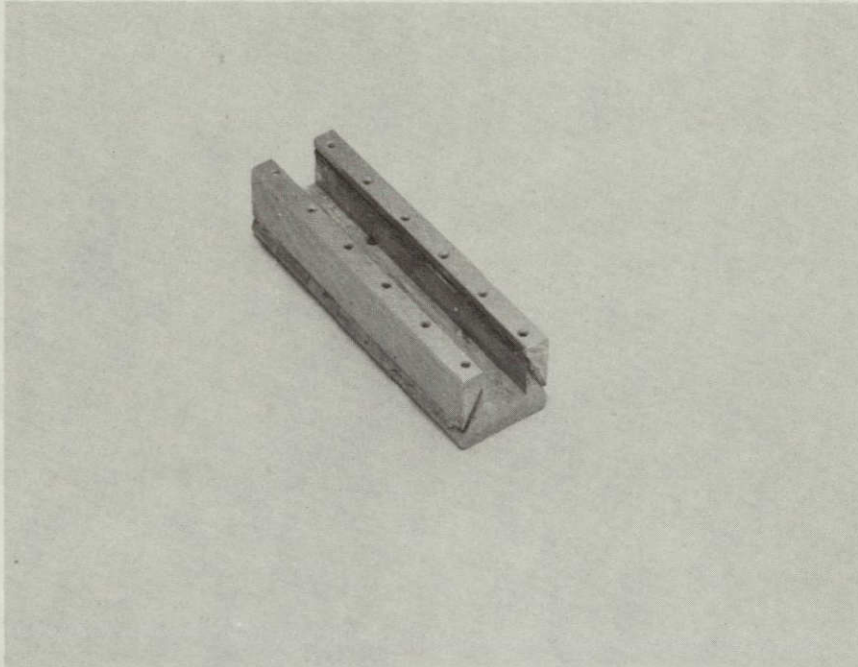


Figure 4-3 Support Magnet Construction





Corporation. These are conventionally called "eddy current" sensors although they are actually sensitive to anything that changes the inductance of the test coil in the probe. Hence, either eddy currents in a conductor or the permeability of a magnetic material can be sensed. In the AMCD, the sensors "look at" the ferrite bands and therefore are operating entirely in a non-eddy-current, magnetic permeability mode. Special calibration of the sensors was required in order to operate in this mode. Linear range of the AMCD sensors is 0.25 cm (0.1 inches) and scale factor was set at 4 volts/cm (10 volts/in.).

#### 4.1.3 Control System

The axial suspension system uses three independent servo loops to control electromagnet currents. An electronic diagram of one of these loops is shown in Figure 4-4. The heart of the electronics is an Inland Controls MA-1 DC servo amplifier which is operated as a current driver to reduce the effects of electromagnet inductance. Equations of motion of this driver and an analysis of the voltage feedback used to damp high frequency roots are given in Appendix A. An analytical block diagram of the entire servo loop is shown in Figure 4-5. Equivalent points on the electronic and analytical diagrams are indicated by letters within hexagons.

The axial suspension system has two modes of operation, a "position" mode and a "virtually zero power" (VZP) mode. In the position mode, rim position error is used to command electromagnet current. The rim has high static and dynamic stiffness about any desired point in the gap. In the VZP mode, the rim position set point is modified by positive feedback of the integral of electromagnet current. The result is that the set point is moved until steady-state current is zero. The permanent magnets are



F76-02

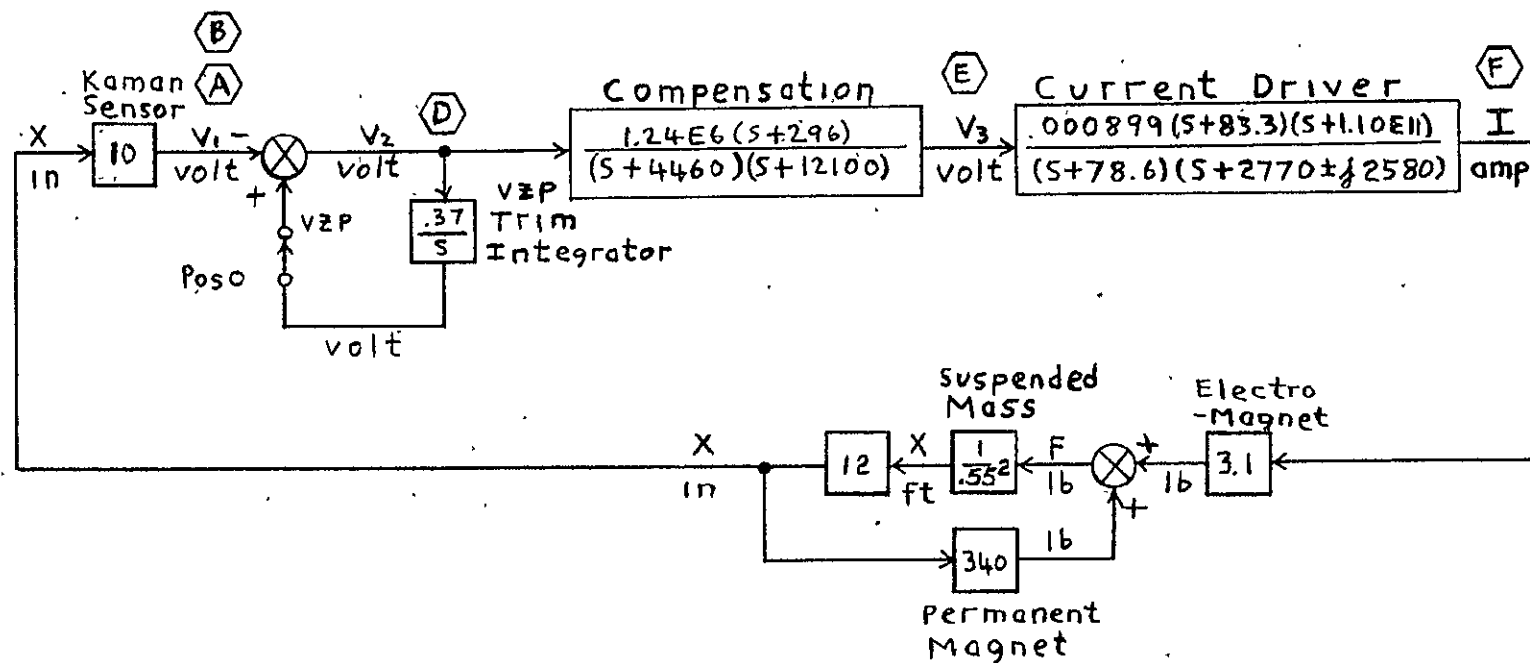
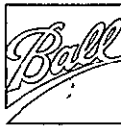


Figure 4-5 AMCD Axial Suspension Station.



then providing all of the support of the rim. Dynamic stiffness is nearly the same as in the position mode but static stiffness is actual negative. If a downward force is applied to the rim in the VZP mode, it initially moves downward but then slowly rises to assume a new zero power position above the old equilibrium position.

The electronic circuit diagram for a radial servo station is shown in Figure 4-6 and the corresponding highly coupled analytical block diagram is shown in Figure 4-7. Again, equivalent points on the two diagrams are indicated by letters in hexagons. The large amount of coupling results from three servos controlling only two degrees of freedom.

Two modes of operation are available, a position mode and a WAHOO mode. The position mode is similar to the axial position mode. The WAHOO mode is a zero power mode that produces zero power operation in the presence of both static loads and rim expansion. This is accomplished by adjusting the position set point at each station as a function of the integral of the sum of the electromagnet currents at the other two stations.

The name WAHOO is derived from the poker game WAHOO. This game is played in a manner such that each player knows what every other player holds but does not know what he himself holds. Inspection of the WAHOO trim loops of Figure 4-7 reveals that for VZP trim purposes, each servo only looks at what the other two are doing. This innovation was developed by BBRC to meet the unique requirements of the AMCD.

The derivation of the WAHOO concept is given in Appendix B. There, it is shown that only the WAHOO concept produces zero power operation for both rim expansion and force disturbances.

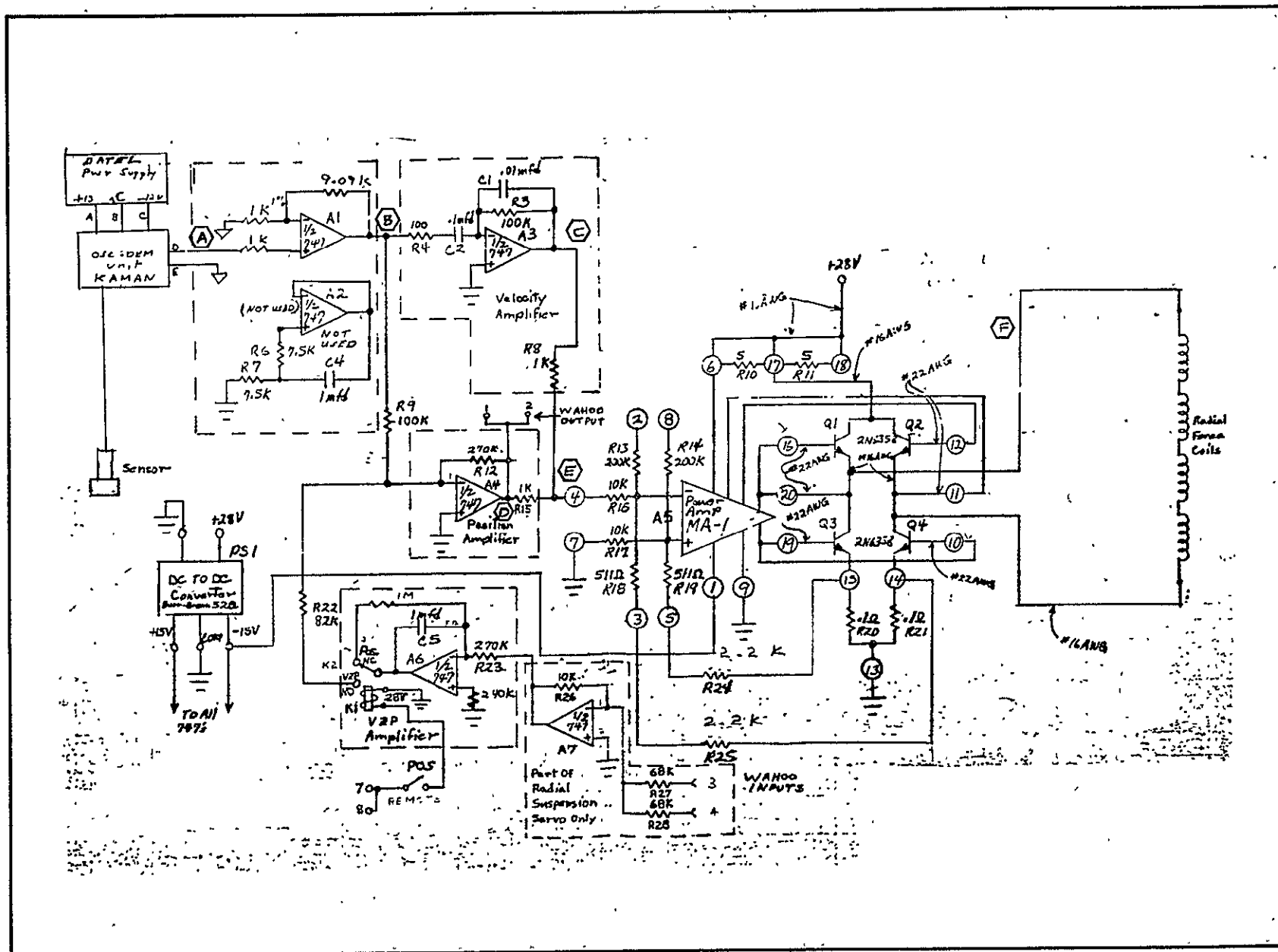


Figure 4-6 Radial Suspension Electronics

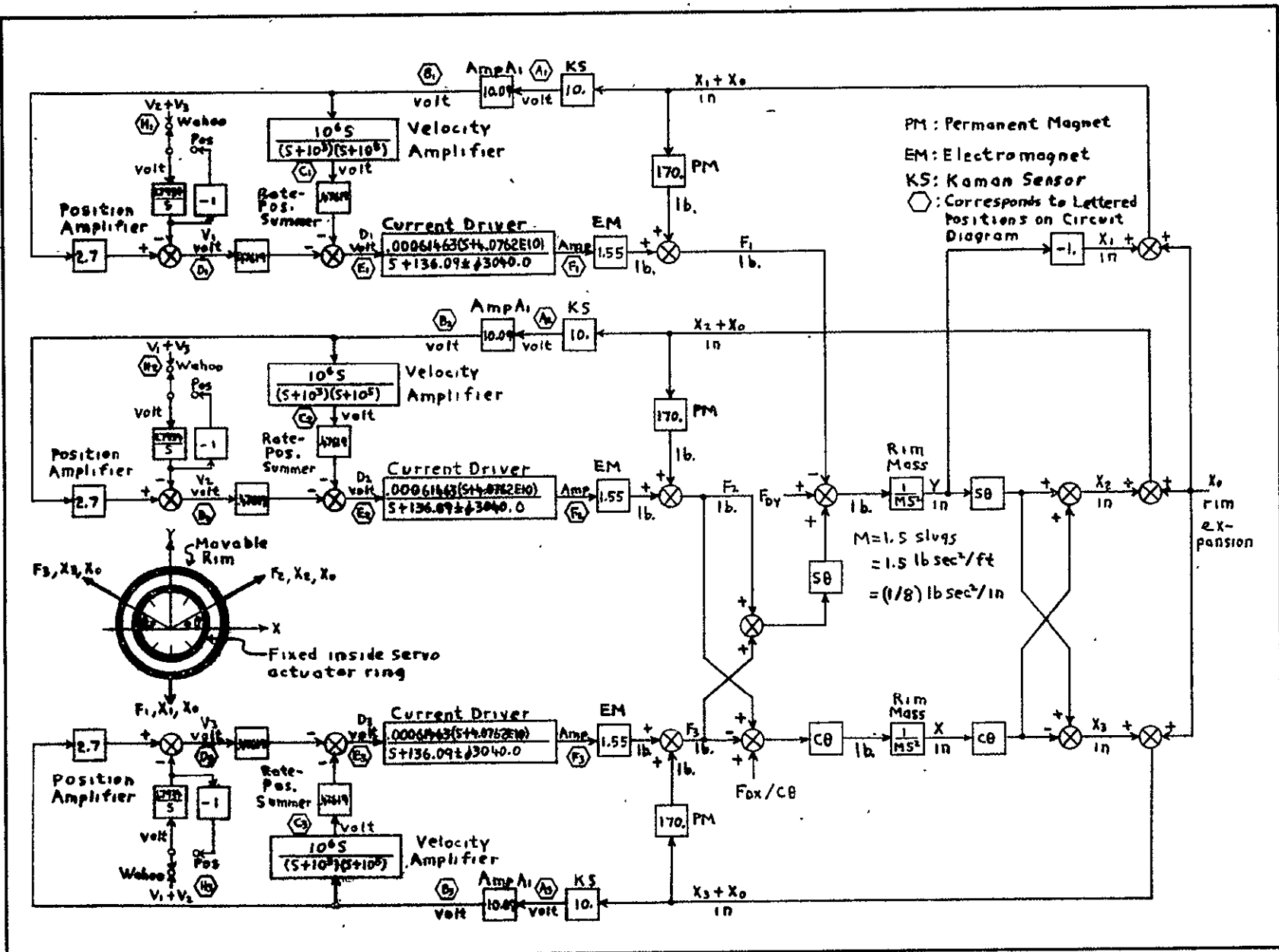
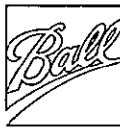


Figure 4-7 AMCD Radial Servos



Appendix B also shows that for single station design purposes, a single station can be represented as shown in Figure 4-8. Two points of interest are immediately evident. The equivalent mass for a single station representation is  $2/3$  the total rim mass. The WAHOO concept which involves negative feedback to each station from the sum of the other two stations resolves to a positive feedback in the single station representation exactly like VZP in the axial mode. This representation can be used for designing the system characteristic root locations. If the characteristic roots from the single station representation are given by  $\Delta$  and the WAHOO gain is  $K_C$ , it is shown in Appendix B that the three station highly coupled set of characteristic roots are given by  $(S + 2K_C)\Delta^2$ .

## 4.2 Performance

### 4.2.1 Static Performance

At each suspension station, the rim will seek an axial equilibrium position based on the applied load and the control system mode ("position" or "VZP"). These equilibrium positions can be presented in one plot as shown in Figure 4-9. The VZP line is a zero current line and has a slope that indicates static instability, however as shown in the next section, the system can operate in a stable manner along this line. The most usual operating position mode point is about 0.01 cm (.025 inches) above the center of the gap. At this point, the slope  $P$  of the VZP line is about 595 newtons/cm (340 lb/in).

In the position mode, an operating line exists for each set point of the position sensor. A family of these is shown in Figure 4-9. The lines are finite in length because of the limited current drive capability of the electronics. The slopes of the lines are approximately 2600 newtons/cm (1500 lb/in).



- Single station equivalent mass is  $2/3$  total mass.
- Note that single station equivalent wahoo is modelled as a positive feedback self loop. We would therefore expect it to act like VZP in the Axial Servos. It does, and furthermore it is not only VZP to disturbance forces, but also to rim expansion.

Figure 4-8 Equivalent Single Radial Servo Station



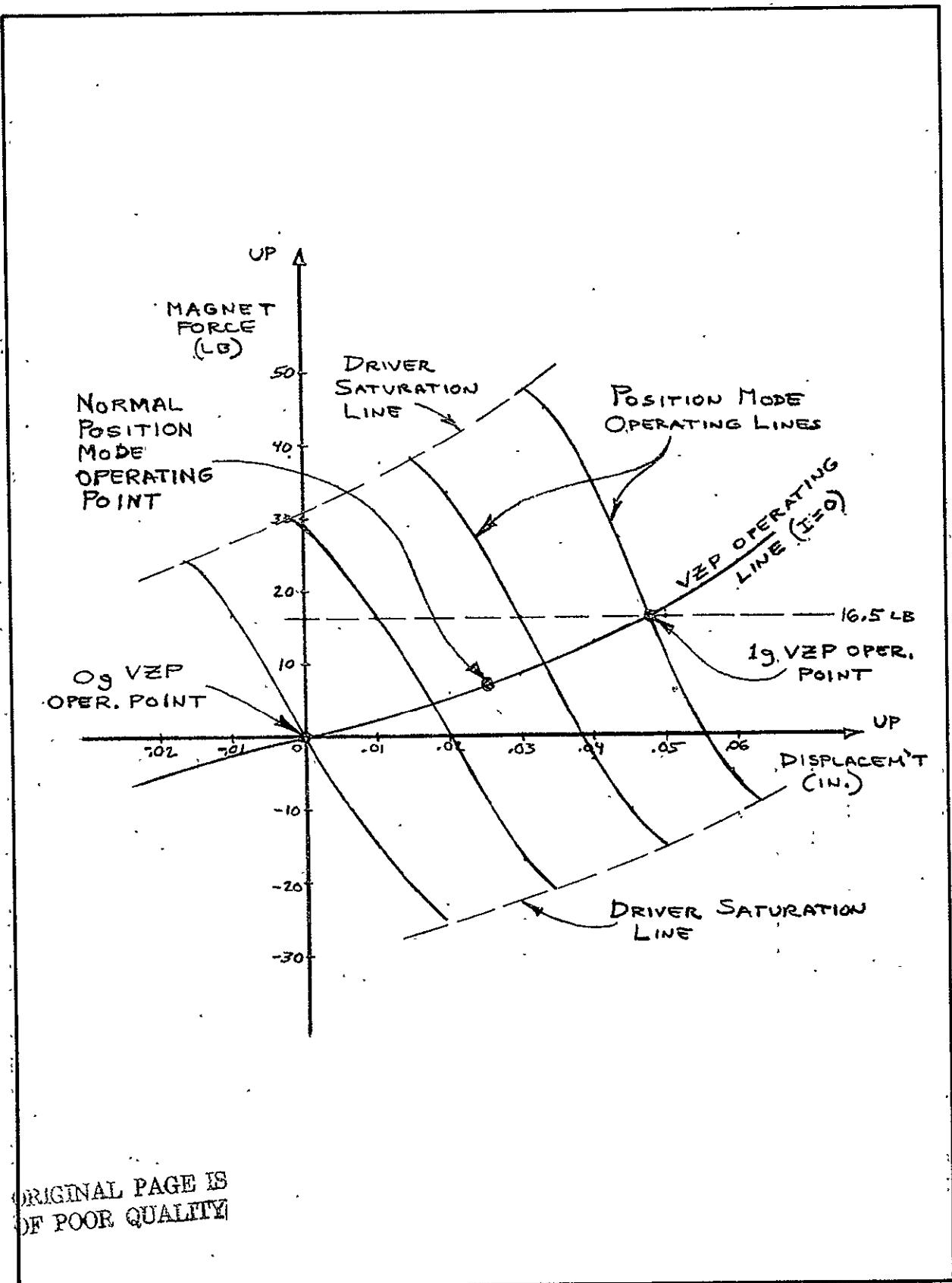


Figure 4-9 Typical Static Suspension System Performance



The force sensitivity  $F$  of each station is about 13.8 newtons/ampere (3.1 lb/amp.). Hence, the force produced by a station is given by (in English units):

$$F = 340X + 3.1I.$$

#### 4.2.2 Dynamic Performance

The analytical block diagram for an axial suspension station is shown in Figure 4-5. For the position mode, the root locus and Bode plots are shown respectively in Figures 4-10 and 4-11. The root locus plot shows that the dominant pole pair has an undamped natural frequency  $\omega_N$  (which we define as bandwidth) of 171 rad/sec (27.2 hertz) and a damping ratio  $\zeta$  of .28. The Bode plot shows that the gain crossover frequency  $\omega_c$  (which some define as bandwidth) is 182.7 rad/sec (29.0 hertz) and that the system phase margin is 23.2°. Both plots show that the lower gain margin is .22 (-13.1 db) and that the upper gain margin is 20.1 (26.1 db).

For the VZP mode, the root locus and Bode plots are shown respectively in Figures 4-12 and 4-13. The root locus plot shows that the dominant pole pair has the same undamped natural frequency and damping ratio as the position mode, that is,  $\omega_N = 171$  rad/sec,  $\zeta = .28$ . The Bode plot shows that two gain crossover frequencies exist, one at .0838 rad/sec (.013 hertz) and one at 182.3 rad/sec (29.03 hertz). The phase margin at the lower crossover frequency is -77.2° and that at the upper crossover frequency is 23.0°. Both plots show that the lower gain margin is .226 (-12.9 db) and that the upper gain margin is 20.11 (26.1 db).

The response due to the step application of a one pound weight is shown for the position mode in Figure 4-14 and for the VZP

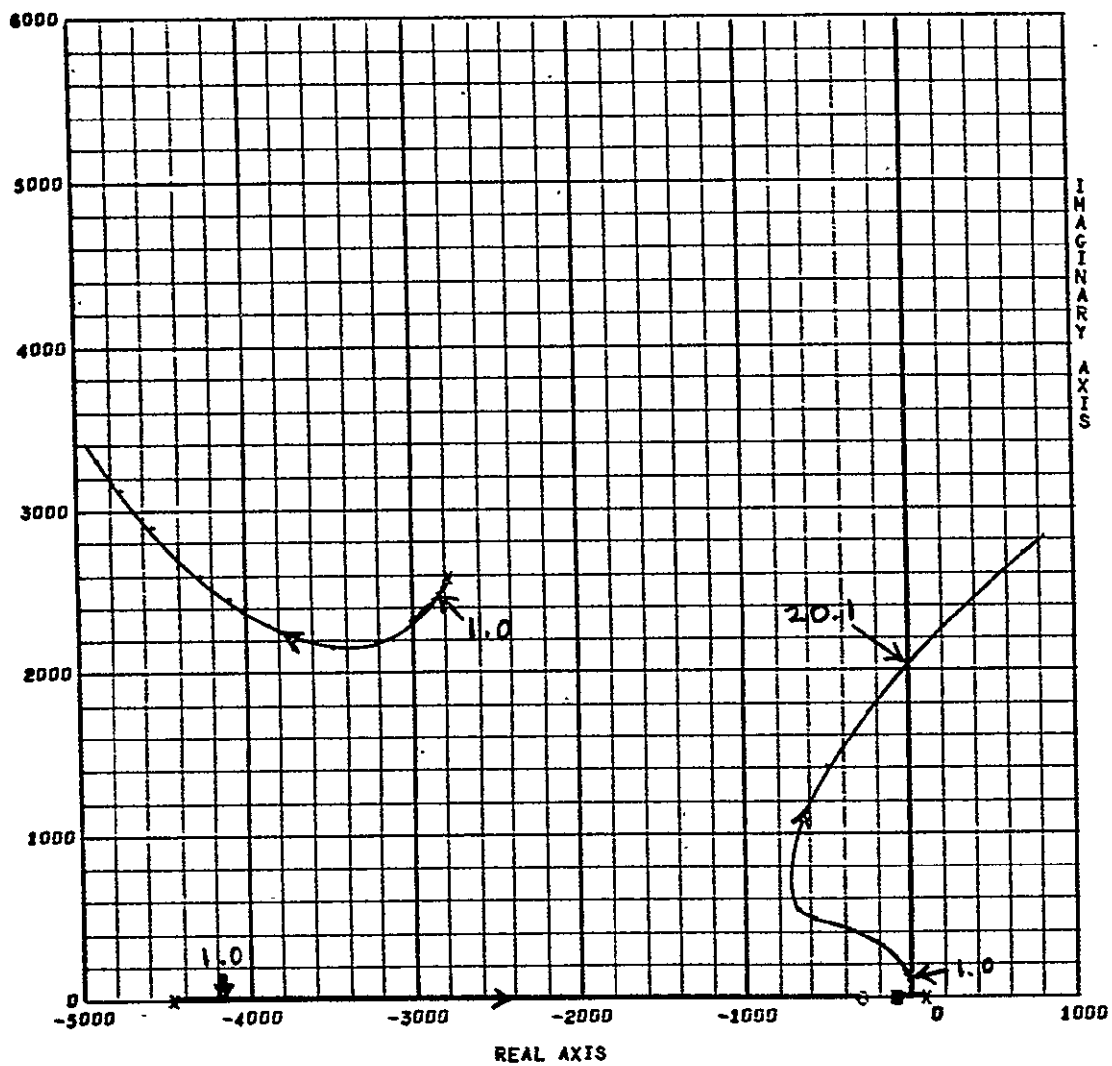


Figure 4-10(A) Root Locus Plot - Nonideal Current Driver With Voltage Feedback

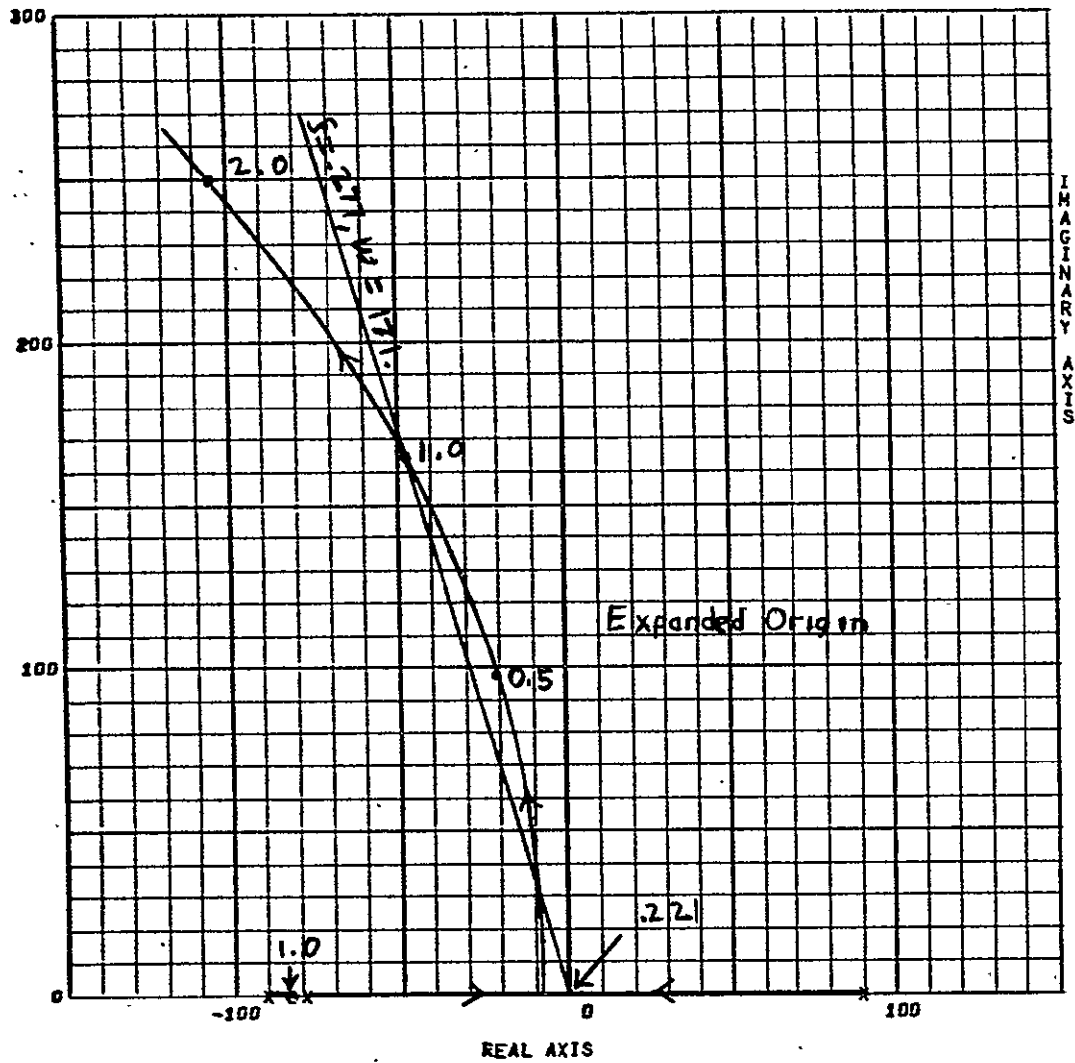


Figure 4-10(B) Root Locus Plot - Nonideal Current Driver With Voltage Feedback

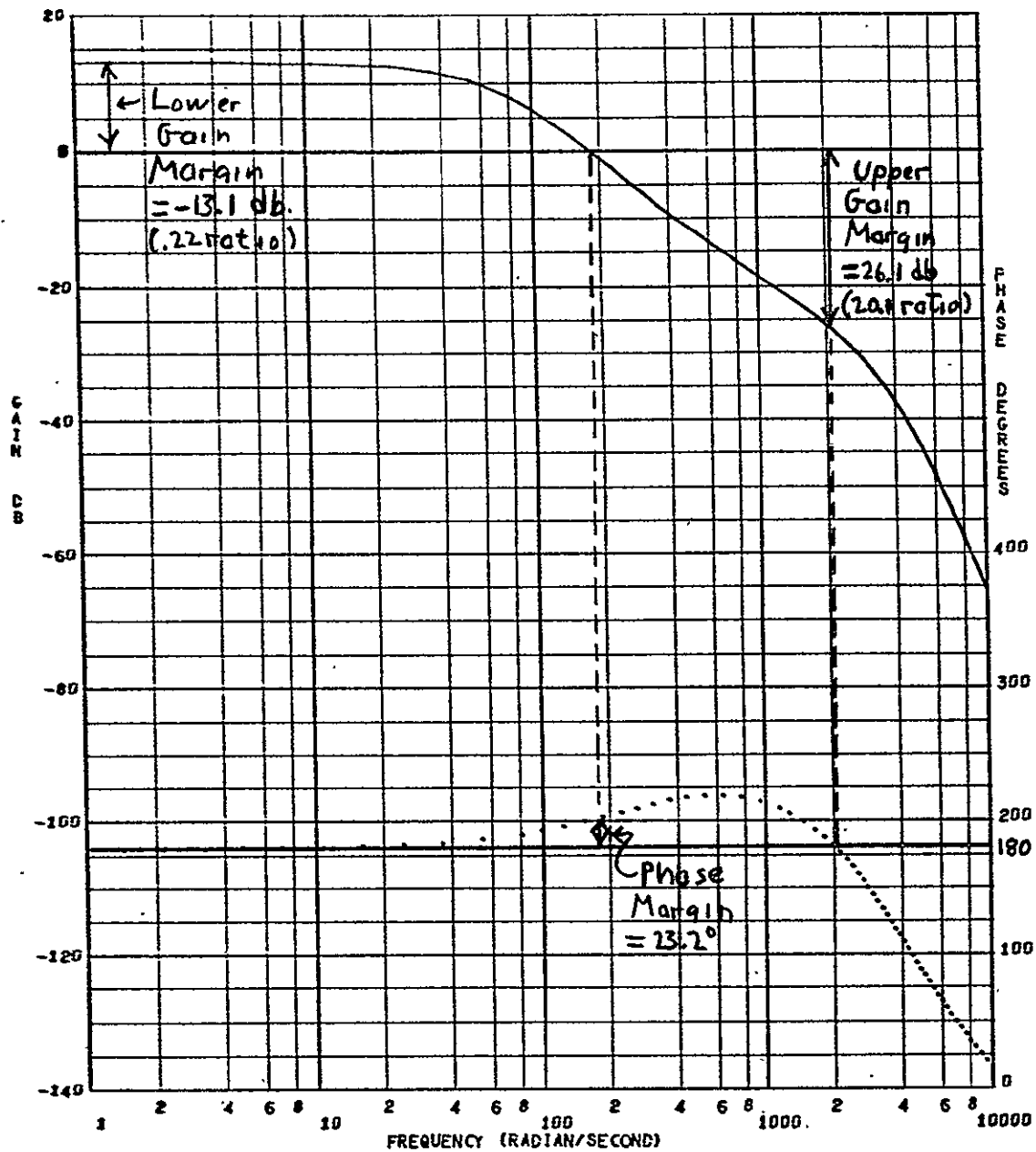


Figure 4-11 Bode Plot - Nonideal Current Driver With Voltage Feedback

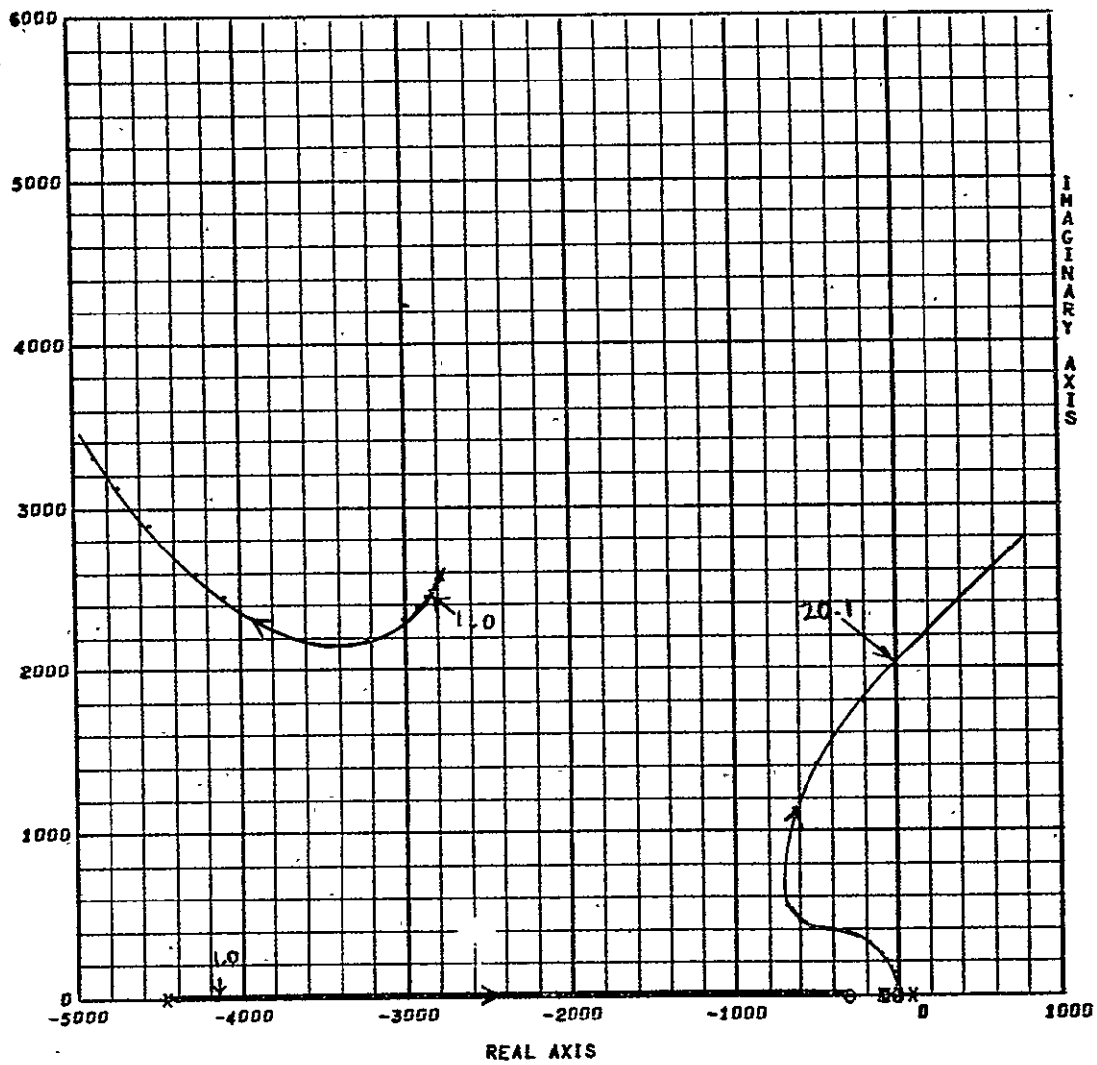


Figure 4-12(A). Root Locus Plot - Nonideal Current Driver With Voltage Feedback

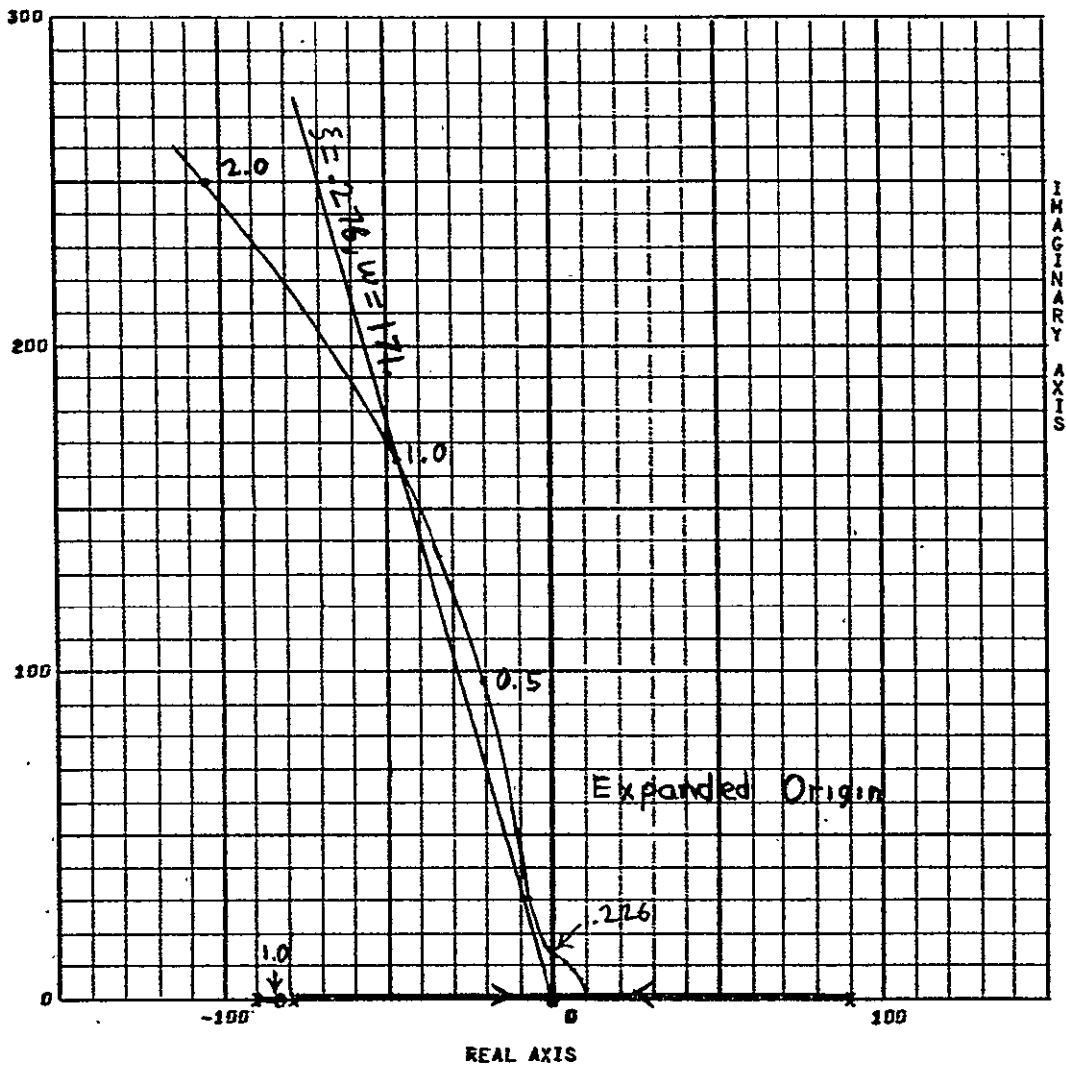


Figure 4-12(B) Root Locus Plot - Nonideal Current Driver With Voltage Feedback



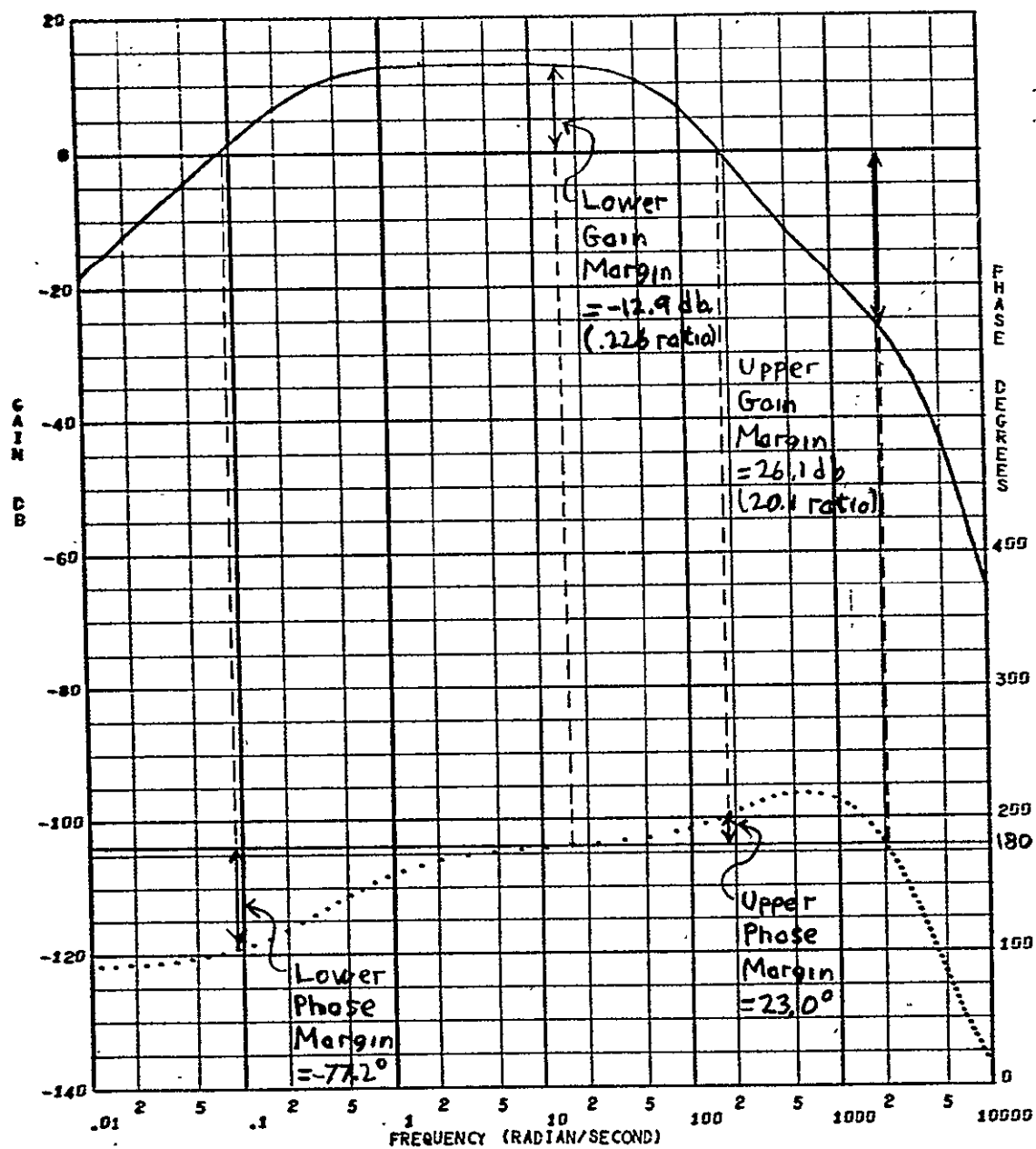


Figure 4-13 Bode Plot - Nonideal Current Driver With Voltage Feedback

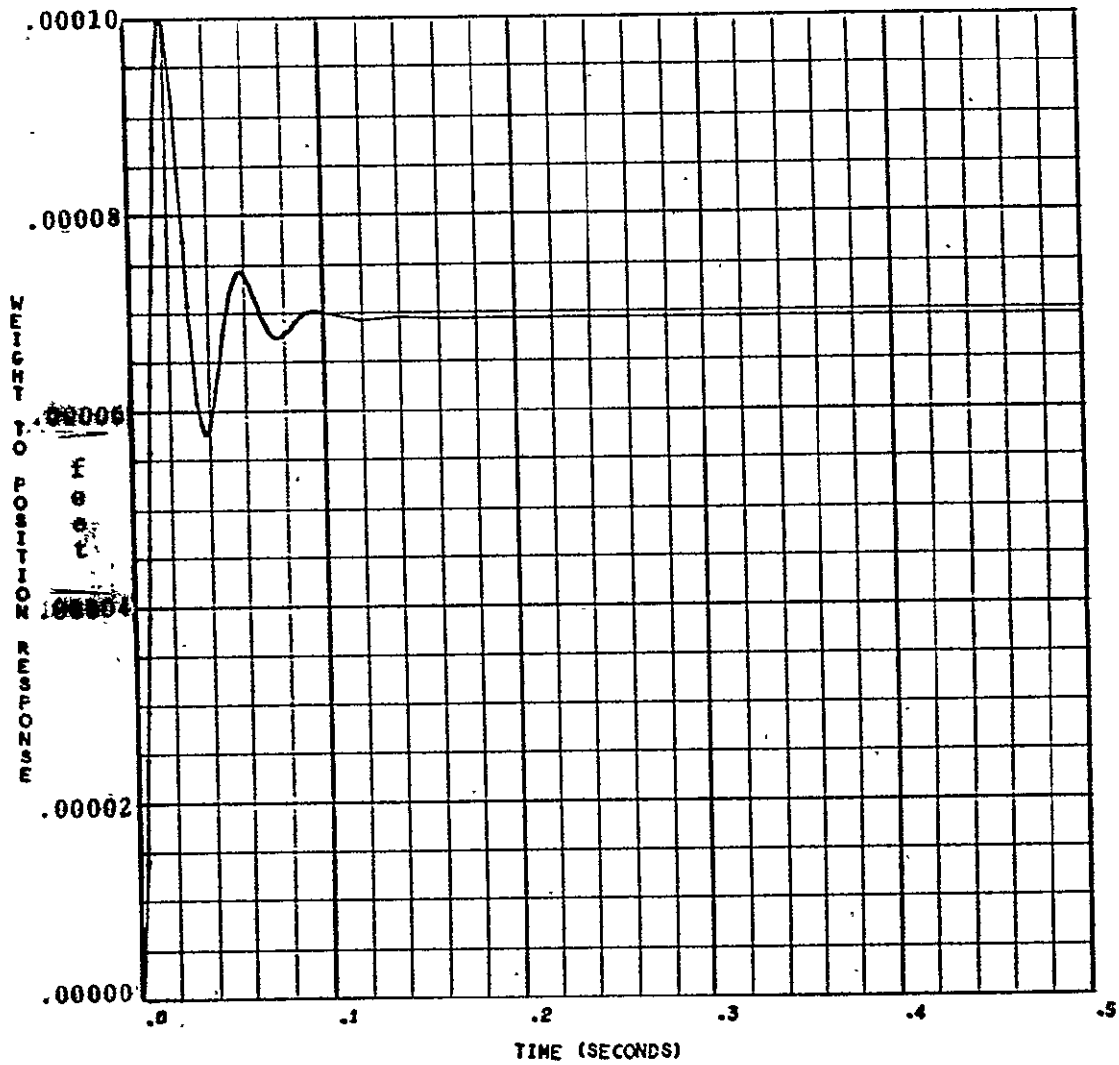


Figure 4-14 Nonideal Current Driver With Voltage Feedback



mode in Figure 4-15. The response for the position mode settles out at  $6.941\text{E-}5$  feet (.002 cm). This yields a position mode stiffness of

$$\text{Stiffness} = \frac{1 \text{ lb.}}{6.941\text{E-}5 \text{ ft.}} \times \frac{\text{feet}}{12 \text{ in.}} = 1200.6 \frac{\text{lb.}}{\text{in.}} (2102 \frac{\text{N}}{\text{cm}})$$

The response for the VZP mode settles out at  $-2.451\text{E-}4$  feet. This yields a VZP mode stiffness of

$$\text{Stiffness} = \frac{1 \text{ lb.}}{-2.451\text{E-}4 \text{ ft.}} \times \frac{\text{feet}}{12 \text{ in.}} = -340.0 \frac{\text{lb.}}{\text{in.}} (-595 \frac{\text{N}}{\text{cm}})$$

Note that the stiffness in the VZP mode is just that of the permanent magnet and that the movement in this mode is toward the applied force. That is, if a weight is placed on the rim in the VZP mode, the rim will move up.

Further insight into the system can be found by examining Appendix C. When using current drivers, the usual tendency is to ignore the high frequency dynamics and simply say that the output current is the input voltage times a constant. This can be very misleading in the case of AMCD. In Appendix C are shown root locus plots using both an ideal current driver and a non-ideal current driver without voltage feedback. It shows that voltage feedback is necessary for the axial suspension. Also shown in Appendix C are Nyquist plots and phase-gain root locus plots of the nominal axial system, that is, the system using current drivers with voltage feedback. The esoteric phase-gain root locus plot shows on one plot the sensitivity of the system roots to change in both gain and phase. For example, it shows what would happen if an additional  $30^\circ$  of phase lag were added to the system from some unknown source.

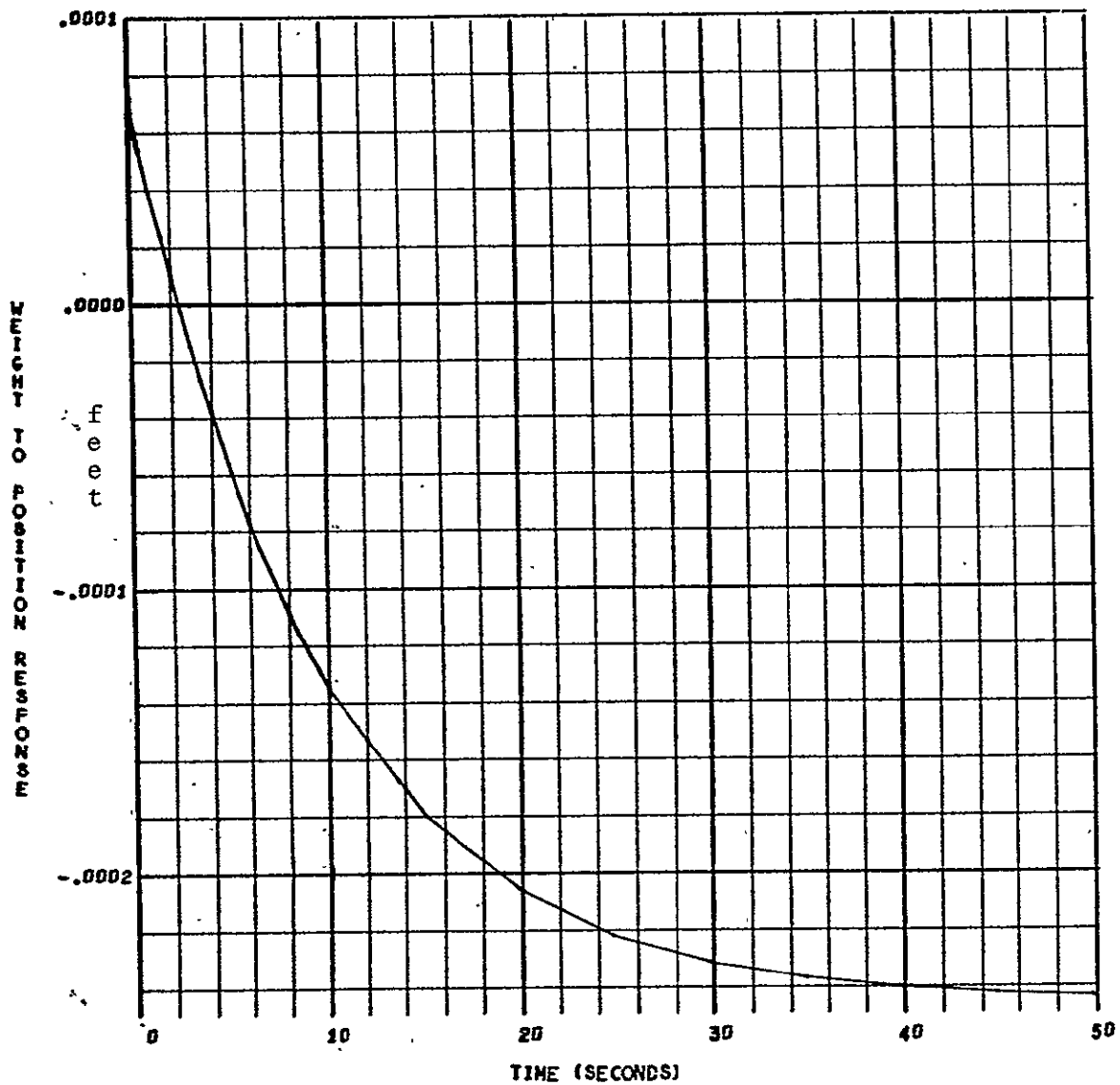


Figure 4-15. Nonideal Current Driver With Voltage Feedback



The equivalent single station radial analytic block diagram is shown in Figure 4-8. It is very similar to an axial station. The root locus and Bode plots for the position mode are shown respectively in Figures 4-16 and 4-17. The root locus plot shows that the dominant pole pair has an undamped natural frequency (bandwidth)  $\omega_N$  of 65.3 rad/sec (10.4 hertz) and damping ratio  $\zeta$  of .18. The Bode plot shows that the gain crossover frequency is 66.6 rad/sec (10.6 hertz) and that the phase margin is 13.5°. Both plots show that the lower gain margin is .329 (-9.65 db) and that the upper gain margin is 70.54 (36.97 db).

The root locus and Bode plots for the WAHOO mode is shown in Figures 4-18 and 4-19. The root locus shows that the dominant pole pair has an undamped natural frequency of 67.4 rad/sec (10.7 hertz) and damping ratio of .16. The Bode plot shows that the upper gain crossover frequency is 69.1 rad/sec (11.0 hertz). At this frequency, the phase margin is 12.6°. Not shown is the fact that the system also has a lower gain crossover frequency of .594 rad/sec (.095 hertz). At this frequency the phase margin is -71.5°. Both plots show that the lower gain margin is .389 (-8.21 db) and that the upper gain margin is 67.01 (36.5 db).

The large upper gain margins for both the position and the VZP modes indicate that current driver voltage feedback is not needed.

Considerable rim bending instabilities were encountered during the design. Early in the development, the axial system was designed to be overdamped. This caused a bending mode to be driven unstable. The compensation was adjusted experimentally until the bending became stable. Unfortunately, this reduced the lead in the system resulting in the present underdamped system. It is believed that bending will present no problem at high spin rates because of the effective stiffening of the rim



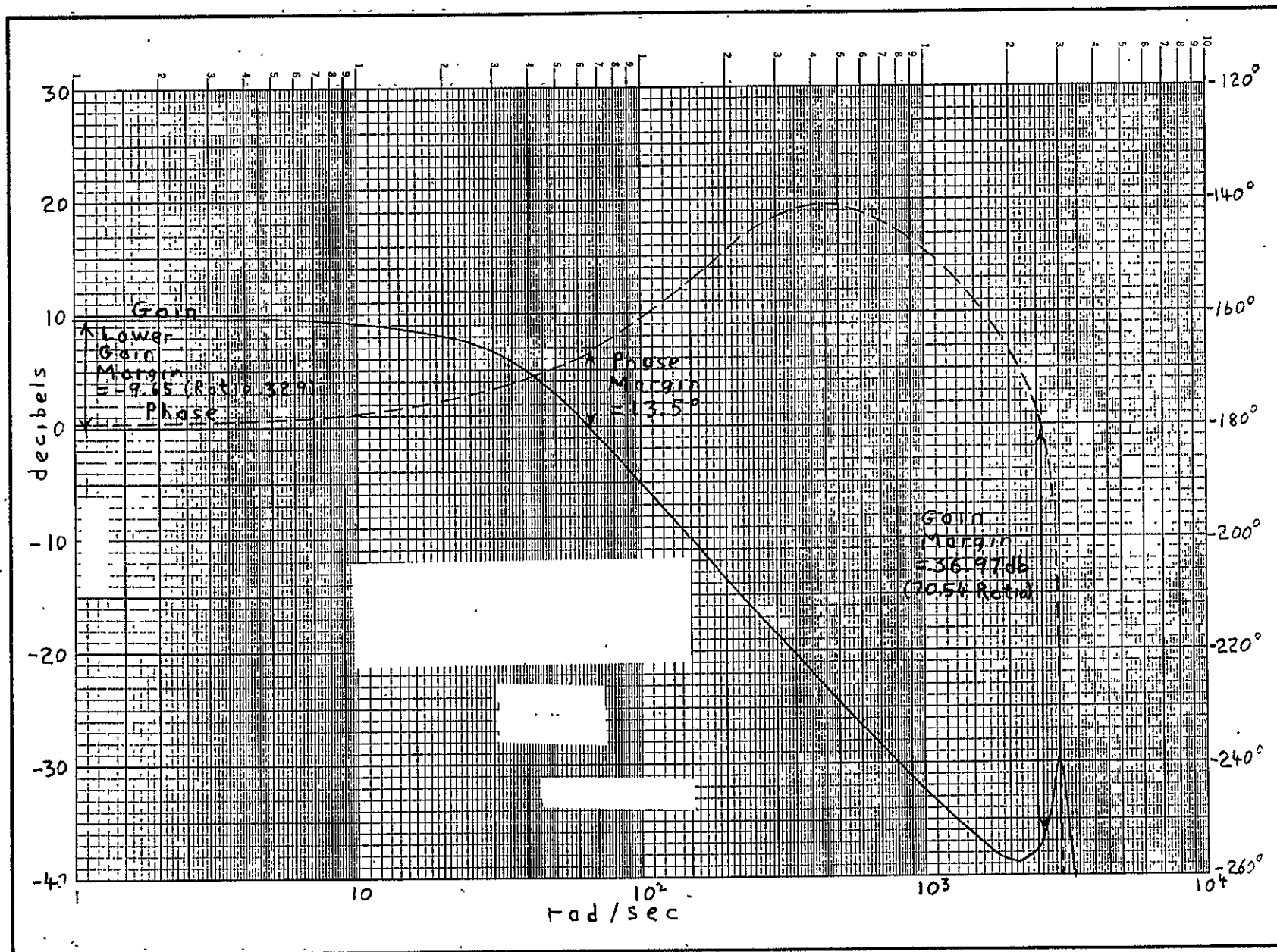


Figure 4-17 AMCD Radial Suspension Equivalent Single Station  
o Position Mode





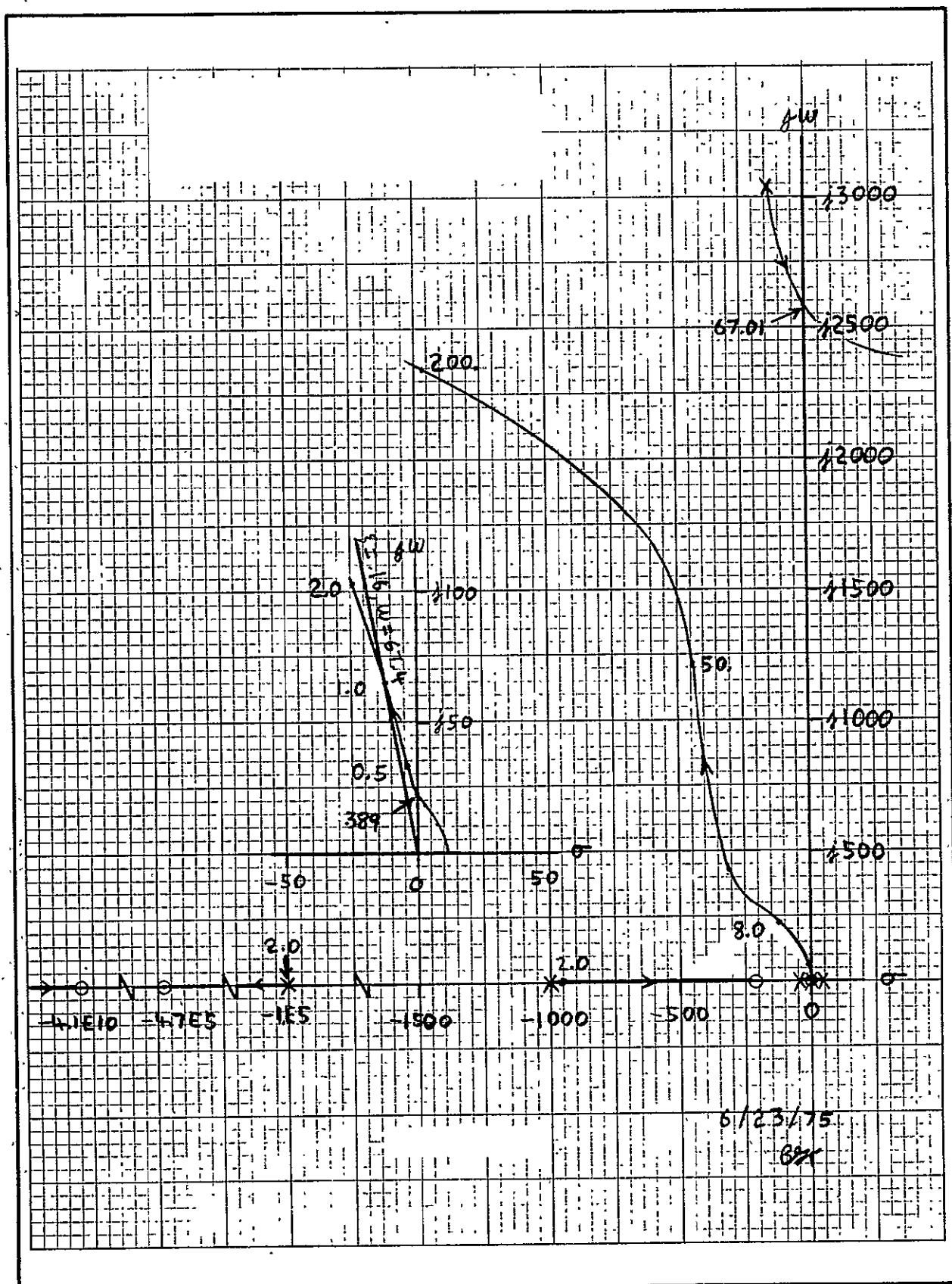


Figure 4-18 AMCD Radial Suspension Equivalent Single Station  
o Wahoo Mode

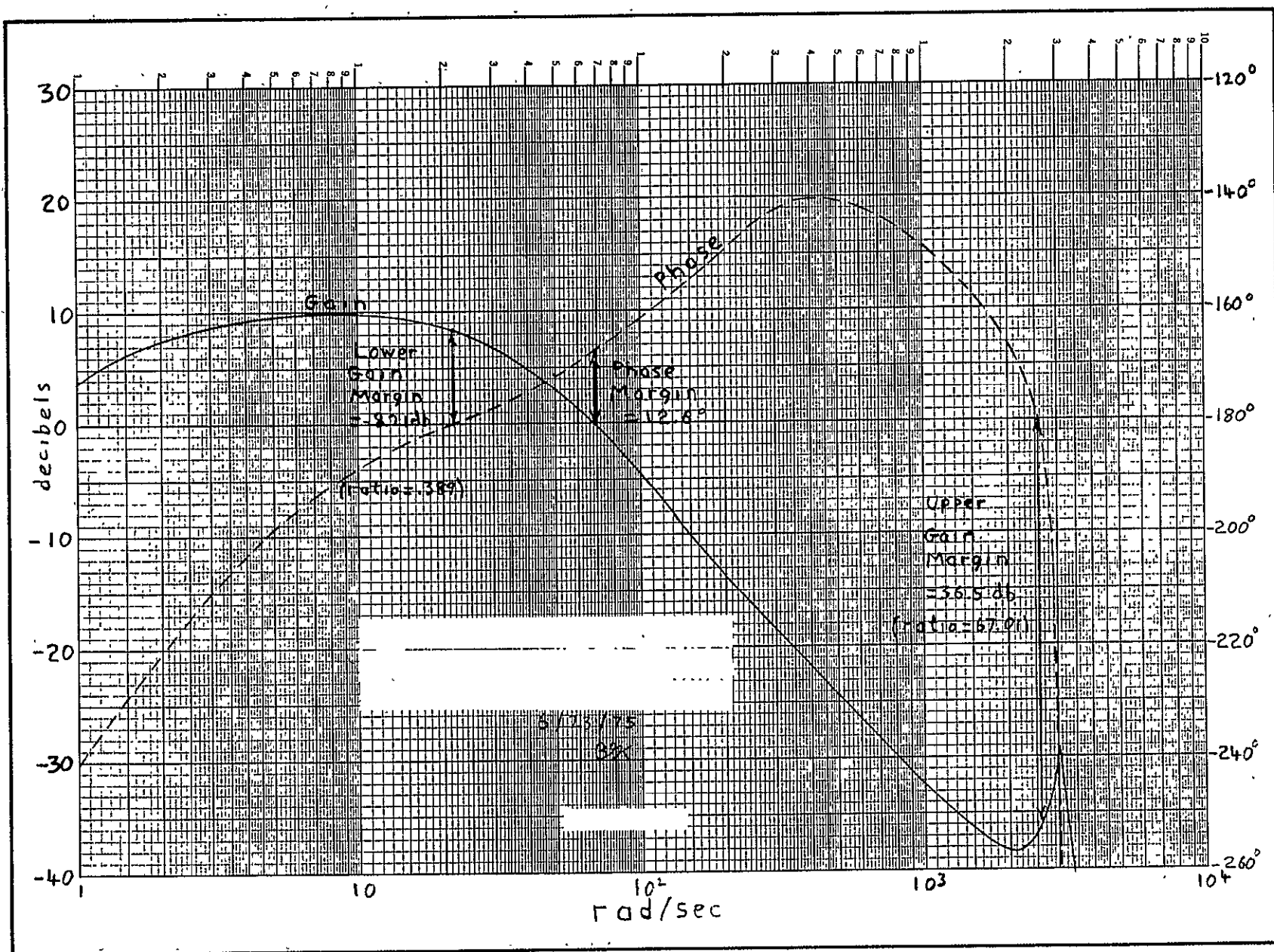


Figure 4-19 AMCD Radial Suspension Equivalent Single Station  
o Wahoo Mode





and the averaging effect on modal pick-up caused by the bending modes moving rapidly past each position sensor.

As the rim is spun up, the three axial stations become more and more coupled by nutational effects. The result of the coupling is to reduce the dominant roots damping ratios more and more to the point the system could go unstable if the rim is spun fast enough. It is believed that this tendency could be greatly reduced or possibly eliminated by the proper combination of cross feeds from one axial suspension station to the others.



## 5.0 DRIVE SYSTEM

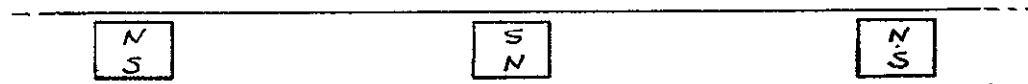
### 5.1 System Description

The AMCD drive motor can be thought of as a large permanent magnet, brushless, d.c. torque motor. Samarium cobalt magnets are bonded into the rim at regular intervals. The two phase armature is segmented with a winding set at each of the three suspension stations. Commutation is controlled by Hall effect sensors mounted near the rim which sense position of the samarium cobalt motor magnets.

### 5.2 Magnet Selection

Alnico was considered along with samarium cobalt for the permanent magnets. The large air gap and segmented winding structure mean the magnets will become nearly air stabilized. The rim was designed with a small outer lip to hold the magnets. This was done to isolate the drive from the suspension as much as possible without adding more mass and complexity to the rim than necessary. This small lip implies a short magnet. Samarium cobalt has high strength for short lengths and does not pay a penalty for air stabilization. In fact it is very difficult to demagnetize this material.

Samarium cobalt magnets 1.4 cm (.55 inches) diameter by .64 cm (.25 inches) length were selected and bonded into the rim with polarities alternated.

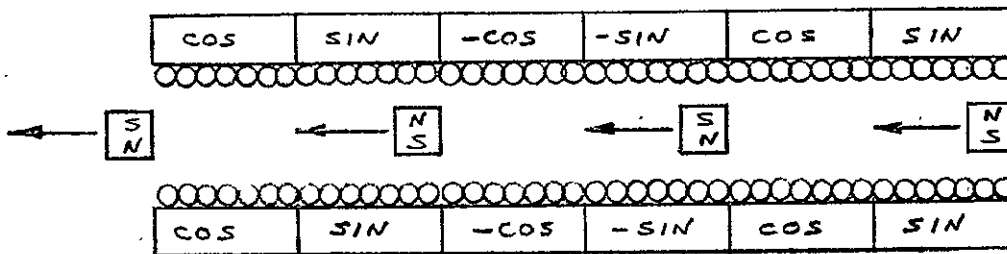


The rim contains a total of 72 magnets spaced 7.3 cm (2.88 inches) apart.



### 5.3 Core and Winding Design

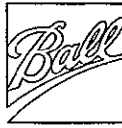
Each armature segment consists of a pair of bar-shaped winding assemblies, one above and one below the rim.



The windings are wound toroidally around the cores in a single layer. The figure above shows only the cross-section of conductors in the air gap as the conductors passing around the other side of the core add nothing to torque and serve only a connecting purpose. The bar-shaped cores are easy to wind and result in a compact structure. The single layer of #18 conductors adds very little to the overall air gap. This effective electro-magnet design was suggested by P. A. Studer of Goddard Space Flight Center.

Ferrite material was chosen for the core to reduce losses. Ferrite also is easily machined into the required irregular shapes.

The windings are grouped into two phases, SINE and COSINE, each of which acts upon three magnets at each motor segment. In operation, current in one phase is acting on the magnets while current in the other phase is reversing in preparation for a magnet of opposite polarity.



#### 5.4 Motor Commutation

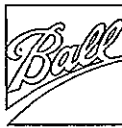
Hall sensors act as commutation devices for the motor. They sense the position of the permanent magnets in the rim and cause the drive coil currents to be switched according to magnet position. The sensors are mounted in pairs, one above the rim and one below, for each winding phase. Outputs from each pair are summed so that the switching position is not affected if the rim moves up or down within the air gap. The SIN pair controls current on the SIN windings of all three motor segments and likewise, the COS pair of Hall sensors controls all COS windings.

#### 5.5 Motor Control Electronics

A block diagram of the motor control electronics is shown in Figure 5-1. For each phase, the Hall sensor outputs are summed and amplified to drive threshold detectors. These detectors sense magnet position and polarity. The phase control logic determines the timing and polarity of the motor coil drivers. Interconnections between the two phase control logic blocks provide positive direction and start-up information.

Each of the six coil drivers controls a phase at one of the motor segments. Associated with each driver is a coil current sensor which monitors the current in that winding. All six of these current sensors receive a common reference from the speed control potentiometer. When current in that particular winding reaches the reference level, the driver turns off until the current decreases. This prevents the current from reaching destructive levels at low speeds and acts as a speed control at high rim speeds.

Since the coil drivers are either full on or off, a very efficient drive is achieved. At low rim speeds the drivers operate as a



conventional PWM (pulse width modulated) amplifier. A quite faithful square wave current of controlled amplitude is fed to the coils. At high speeds, high acceleration (or deceleration) is possible with the drivers full on for the period between magnets with current rise and fall limited by the inductance of the coils.

## 5.6 Torque Calculations

The equation for the force between a magnetic field and a current carrying conductor is:

$$F = BLI$$

where

F = Force in Newtons .

B = Flux Density in Teslas (Webers/Meter<sup>2</sup>)

L = Conductor Length in Meters

I = Current in Amps

If the magnetic field is created by a permanent magnet the force can be considered to act on the magnet if the conductor is held stationary which is the case with the AMCD motor.

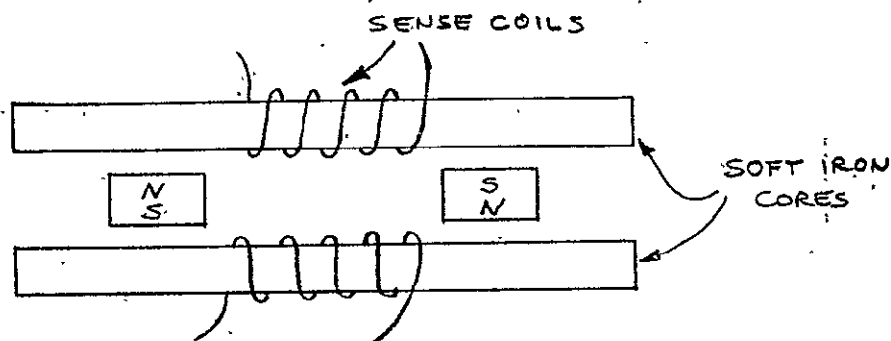
To arrive at design force, each of the factors B, L, and I must be evaluated.

A force calculation will be made for one magnet face interacting with a coil. This can be then doubled to account for both ends of the magnet, next tripled to take into account the three magnets in one motor segment, and tripled again to realize the total force for the three motor segments. Then using the radius of the rim, we can calculate developed torque.



### Flux Density Calculation (B)

The large air gap makes it difficult to estimate how much of the magnet flux will couple through the winding core and how much will be lost to leakage. A measurement of coupling flux was made using a pair of soft iron bars similar to the ferrite cores:



The flux measured was  $0.375 \times 10^{-4}$  Webers with magnets of average strength.

This flux that couples through the ferrite core must be converted to flux density (B) in the air gap where it interacts with the coil windings. There are two practical choices for doing this. We can assume all the flux goes straight up from the surface of the magnet and reacts with only those turns above the magnet or we can assume the flux spreads out evenly over the winding area and reacts with all the turns equally. Of course, the truth lies somewhere in between but the second approach gives an adequate approximation.

The winding area in the air gap for one magnet coil phase is  $1.9 \times 3.6$  cm or  $6.8 \text{ cm}^2$ .

Flux density then is

$$B = \frac{\phi_m}{A} = \frac{0.375 \times 10^{-4} \text{ Webers}}{6.8 \times 10^{-4} \text{ m}^2} = 0.055 \text{ Web/M}^2.$$





### Conductor Length Calculation (L)

In the winding phase area there are 28 turns with an effective length of 1.9 cm each.

Total effective length is then

$$L = 1.9 \times 28 = 53.2 \text{ cm} = 0.532 \text{ M.}$$

### Current (I)

The electronics are designed so that the coil drivers and wiring can handle 4 amperes. Also, the inductance of the coils was examined to be sure that currents of this magnitude can be reversed at maximum rim speed frequencies with a 60 volt power supply. Force (and torque) will then be calculated for the design maximum of 4 amps.

### Force

We can now calculate force from the equation

$$\begin{aligned} F &= BLI \\ &= 0.055 \times 0.532 \times 4 = 0.117 \text{ Newtons.} \end{aligned}$$

Recall that this is the force for a single magnet surface interface. For the total motor this is multiplied by 18.

$$\text{Total Force} = 0.117 \times 18 = 1.76 \text{ Newtons.}$$



This times the magnet radius (0.838 meters) gives total torque.

$$\text{Total Torque} = 1.76 \times 0.838 = 1.76 \text{ Newton-Meters.}$$

(1.3 lb-ft)

A small (1/4 diameter) test wheel was built to check the above torque calculations. Acceleration measurements were made and from the known wheel inertia, torque was determined. Correlation within 10% of the calculated torque was achieved.

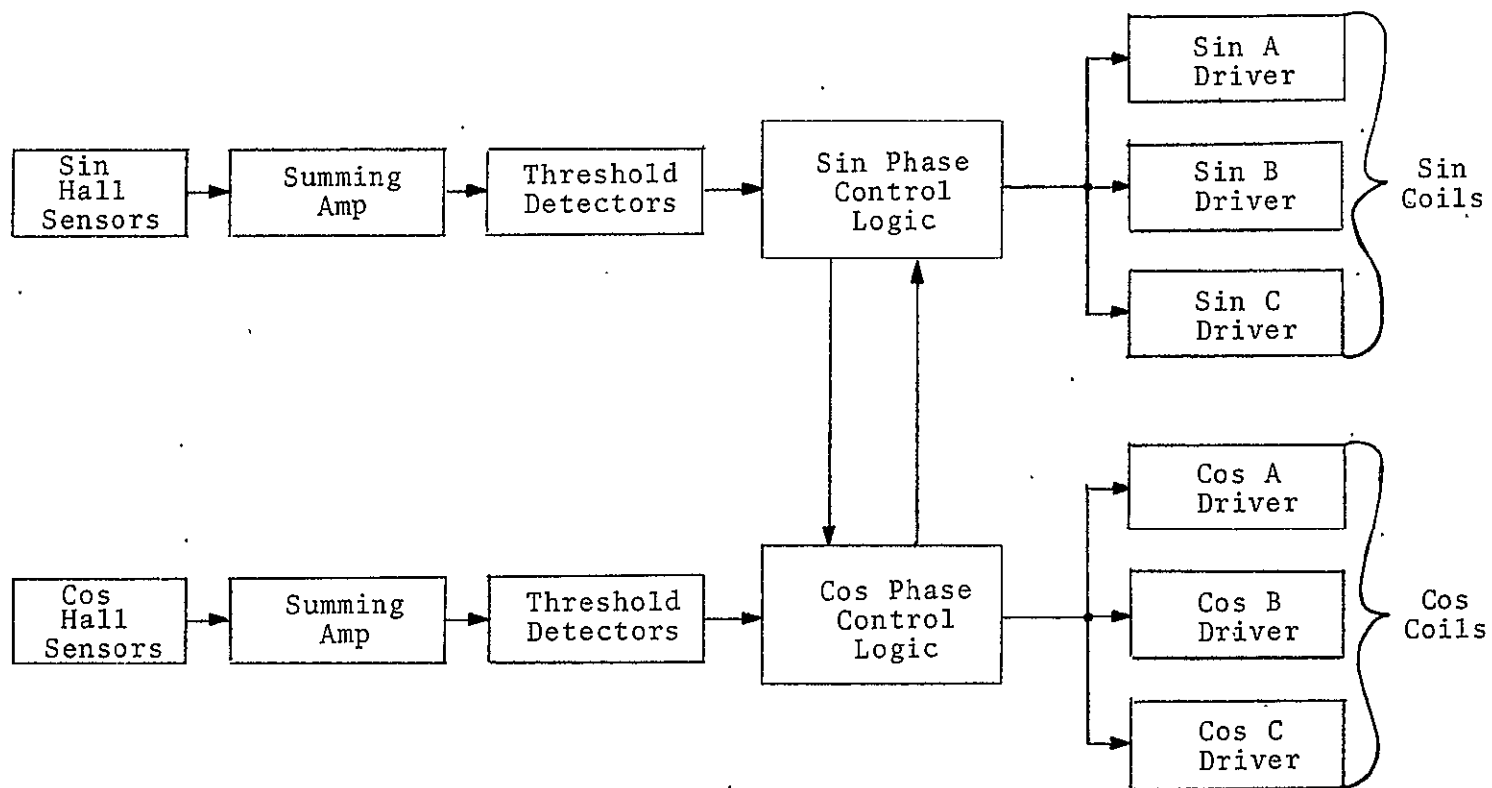


Figure 5-1 Motor Control Electronics.



## 6.0 REFERENCES

1. Anderson, Willard W.; and Groom, Nelson J.: The Annular Momentum Control Device (AMCD) and Potential Applications. NASA TN D-7866, 1975.



APPENDIX A  
CURRENT DRIVER EQUATIONS AND TRANSFER FUNCTIONS



# Appendix A Current Driver Equations and Transfer Functions

When using current drivers, the usual tendency is to ignore the high frequency dynamics and simply say that the output current is just the input voltage times a constant. This was very misleading in the case of AMCD as shown in Appendix C. The circuit diagram of a current driver with voltage feedback and its equivalent diagram are shown in Figure A-1.

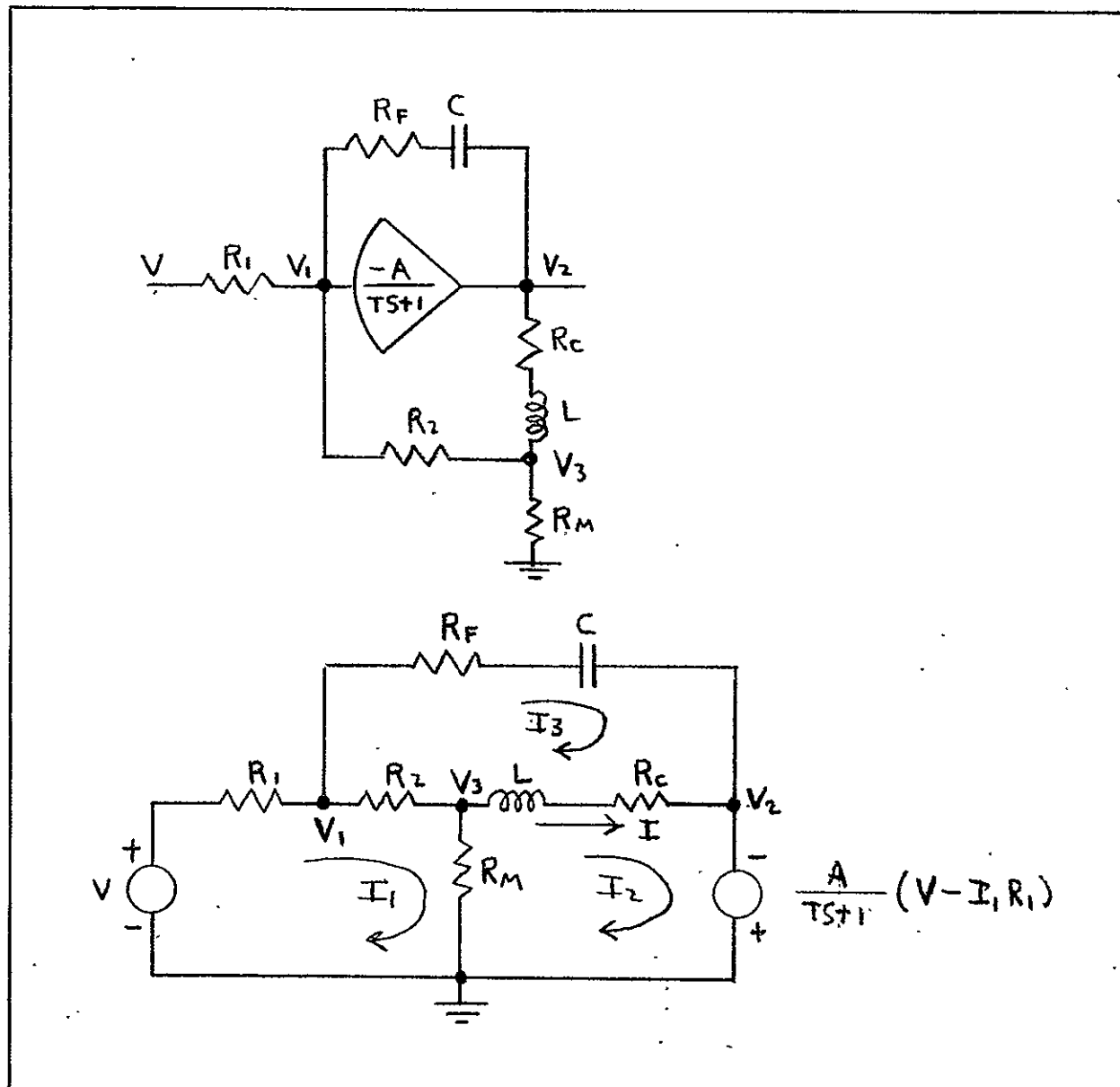


Figure A-1 Current Driver and Equivalent Circuit



The beginning equations of motion are the following:

$$\begin{bmatrix} R_{11} & -R_M & -R_2 \\ -R_M & SL + R_{22} & -(SL + R_C) \\ -R_2 & -(SL + R_C) & SL + R_{33} + S^{-1}C^{-1} \end{bmatrix} \begin{pmatrix} I_1 \\ I_2 \\ I_3 \end{pmatrix} = \begin{pmatrix} 1 \\ A(TS+1)^{-1} \\ 0 \end{pmatrix} V + \begin{pmatrix} 0 \\ -AR_1(TS+1)^{-1} \\ 0 \end{pmatrix} I_1$$

where

$$R_{11} \triangleq R_1 + R_2 + R_M$$

$$R_{22} \triangleq R_M + R_C$$

$$R_{33} \triangleq R_2 + R_F + R_C$$

Transposing  $I_1$  to the left hand side we obtain:

$$\begin{bmatrix} R_{11} & -R_M & -R_2 \\ -R_M(TS+1) + AR_1 & (TS+1)(SL+R_{22}) & -(TS+1)(SL+R_C) \\ -SR_2 & -S(SL+R_C) & S^2L+SR_{33}+C^{-1} \end{bmatrix} \begin{pmatrix} I_1 \\ I_2 \\ I_3 \end{pmatrix} = \begin{pmatrix} 1 \\ A \\ 0 \end{pmatrix} V$$

What we really want is the current through the inductance:

$$= I_2 - I_3$$

Adding this equation to the system we obtain:

$$\begin{bmatrix} C_{11} & C_{12} & C_{13} & 0 \\ B_{21}S+C_{21} & A_{22}S^2+B_{22}S+C_{22} & A_{23}S^2+B_{23}S+C_{23} & 0 \\ B_{31}S & A_{32}S^2+B_{32}S & A_{33}S^2+B_{33}S+C_{33} & 0 \\ 0 & -1 & 1 & 1 \end{bmatrix} \begin{pmatrix} I_1 \\ I_2 \\ I_3 \\ I \end{pmatrix} = \begin{pmatrix} 1 \\ A \\ 0 \\ 0 \end{pmatrix} V$$



where by definition

$$\begin{aligned}
 C_{11} &= R_{11} & B_{22} &= L + TR_{22} & A_{32} &= -L \\
 C_{12} &= -R_M & C_{22} &= R_{22} & B_{32} &= -R_C \\
 C_{13} &= -R_2 & A_{23} &= -TL & A_{33} &= L \\
 B_{21} &= -R_M^T & B_{23} &= -L - TR_C & B_{33} &= R_{33} \\
 C_{21} &= AR_1 - R_M & C_{23} &= -R_C & C_{33} &= C^{-1} \\
 A_{22} &= TL & B_{31} &= -R_2
 \end{aligned}$$

If the voltage feedback is removed, these equations reduce very simply to:

$$\begin{bmatrix} R_1 + R_2 + R_M & -R_M \\ -R_M(TS+1) + AR_1 & (SL + R_C + R_M)(TS+1) \end{bmatrix} \begin{pmatrix} I_1 \\ I_2 \end{pmatrix} = \begin{pmatrix} 1 \\ A \end{pmatrix} V$$

where  $I_2$  is the current through the inductance. We want the transfer function  $I_2/V$ . First divide the second equation through by  $LT$  to obtain

$$\begin{bmatrix} R_1 + R_2 + R_M & -R_M \\ -R_M L^{-1}(S+T^{-1}) + L^{-1}T^{-1}AR_1 & [S + L^{-1}(R_C + R_M)](S+T^{-1}) \end{bmatrix} \begin{pmatrix} I_1 \\ I_2 \end{pmatrix} = \begin{pmatrix} 1 \\ AL^{-1}T^{-1} \end{pmatrix} V$$





Then, by Cramer's rule

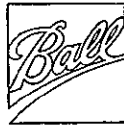
$$\begin{aligned} \frac{I_2}{V} &= \frac{(R_1 + R_2 + R_M) A L^{-1} T^{-1} + R_M L^{-1} (S + T^{-1}) - L^{-1} T^{-1} A R_1}{(R_1 + R_2 + R_M) (S + T^{-1}) \left[ S + L^{-1} (R_C + R_M) \right] - R_M^2 L^{-1} (S + T^{-1}) + L^{-1} T^{-1} A R_1 R_M} \\ &= \frac{(R_2 + R_M) A L^{-1} T^{-1} + R_M L^{-1} (S + T^{-1})}{(R_1 + R_2 + R_M) (S + T^{-1}) (S + L^{-1} R_C) + L^{-1} R_M (R_1 + R_2) (S + T^{-1}) + L^{-1} T^{-1} A R_1 R_M} \end{aligned}$$

Further manipulation yields

$$\frac{I_2}{V} = \frac{R_M L^{-1}}{(R_1 + R_2 + R_M)} \frac{S + T^{-1} + (R_2 + R_M) A R_M^{-1} T^{-1}}{(S + T^{-1}) (S + L^{-1} R_C) + \frac{L^{-1} R_M (R_1 + R_2)}{R_1 + R_2 + R_M} \left[ S + T^{-1} + \frac{L^{-1} T^{-1} A R_1 R_M}{L^{-1} R_M (R_1 + R_2)} \right]}$$

Finally, the desired current driver without voltage feedback transfer function is given by

$$\frac{I_2}{V} = \frac{R_M L^{-1}}{(R_1 + R_2 + R_M)} \frac{S + T^{-1} \left[ 1 + A (1 + R_2 R_M^{-1}) \right]}{(S + T^{-1}) (S + L^{-1} R_C) + \frac{L^{-1} R_M (R_1 + R_2)}{R_1 + R_2 + R_M} \left\{ S + T^{-1} \left[ 1 + \frac{A R_1}{R_1 + R_2} \right] \right\}}$$



For infinite amplifier open loop gain,  $A = \infty$ , the transfer function reduces to

$$\begin{aligned} \lim_{A \rightarrow \infty} \frac{I_2}{V} &= \frac{\cancel{R_M} \cancel{L^{-1}}}{\cancel{R_1 + R_2 + R_M}} \cdot \frac{\cancel{T^{-1}} (1 + R_2 R_M^{-1})}{\cancel{L^{-1} R_M (R_1 + R_2) T^{-1} R_1}} \cdot \frac{\cancel{(R_1 + R_2 + R_M) (R_1 + R_2)}}{\cancel{(R_1 + R_2 + R_M) (R_1 + R_2)}} \\ &= \frac{(1 + R_2 R_M^{-1})}{R_1} = \frac{R_2}{R_1} \left( \frac{1}{R_2} + \frac{1}{R_M} \right) \approx \frac{R_2}{R_1 R_M} \text{ for } R_2 \gg R_M \end{aligned}$$

This is the transfer function which is used

$$\frac{I_2}{V} = \frac{R_2}{R_1 R_M}$$

if the high frequency roots may be ignored.

When the high frequency roots are not to be ignored and

$$\text{if } A, R_2, R_1 \gg \max(R_M, R_C, 1)$$

$$\text{and } \frac{R_M A R_1}{R_1 + R_2} \gg R_C$$



The transfer function simplifies to

$$\begin{aligned} \frac{I_2}{V} &= \frac{R_M L^{-1}}{R_1 + R_2} \frac{S + T^{-1} A R_2 R_M^{-1}}{(S + T^{-1})(S + L^{-1} R_C) + L^{-1} R_M (S + T^{-1} A R_1 / (R_1 + R_2))} \\ &= \frac{R_M L^{-1}}{R_1 + R_2} \frac{S + T^{-1} A R_2 R_M^{-1}}{S^2 + (T^{-1} + L^{-1} R_C + L^{-1} R_M) S + \frac{T^{-1} L^{-1} R_M A R_1}{R_1 + R_2}} \\ &\cong S + \frac{T^{-1} + L^{-1} (R_C + R_M)}{2} \pm \sqrt{j \frac{R_M A R_1}{T L (R_1 + R_2)}} \end{aligned}$$

The dc gain of this transfer function reduces to the same transfer function used if the high frequency roots may be ignored, that is

$$\frac{I_2}{V} = \frac{R_2}{R_1 R_M}$$

For the radial MA-1 Current Driver

$$\begin{aligned} R_1 &= 10. \text{ K}\Omega & R_2 &= 2.711 \text{ K}\Omega & R_M &= .1\Omega \\ R_C &= 3.0 \Omega & L &= .0128 \text{ h} & T^{-1} &= 30. & A &= 50119 \end{aligned}$$

Then the radial current driver without voltage feedback has the transfer function

$$\frac{I_2}{V} = \frac{.00061463(S + 4.0762E10)}{S + 136.09 \pm j3040.0}$$



For the axial MA-1 current driver

$$\begin{aligned} R_1 &= 10K & R_2 &= 7.311K & C &= .01 \mu f & R_{11} &= 1.7311E4 \\ L &= .0064 & R_F &= 1.2M & R_C &= 1.4 & R_{22} &= 1.5 \\ A &= 50119 & R_M &= .1 & T^{-1} &= .30 & R_{33} &= 1.2073E6 \end{aligned}$$

Then

$$\begin{aligned} C_{11} &= 1.7311E4 & B_{22} &= 5.64E-2 & A_{32} &= -.0064 \\ C_{12} &= -.1 & C_{22} &= 1.5 & B_{32} &= -1.4 \\ C_{13} &= -7.311E3 & A_{23} &= -2.1333E-4 & A_{33} &= .0064 \\ B_{21} &= -3.3333E-3 & B_{23} &= -5.3067E-2 & B_{33} &= 1.2073E6 \\ C_{21} &= 5.0119E8 & C_{23} &= -1.4 & C_{33} &= 1.0E8 \\ A_{22} &= 2.1333E-4 & B_{31} &= -7.311E3 \end{aligned}$$

Without voltage feedback, the axial current driver has the transfer function

$$\frac{I_2}{V} = \frac{.00090261(S+1.0993E11)}{S+132.19 \pm j3683.9}$$



Note that without voltage feedback the damping ratio on both the radial and axial current driver high frequency roots is less than .05. This appears to be all right for the radial servos but is very bad for the axial servos as shown in Appendix C. Consequently, voltage feedback has not been employed for the radial servo's current drivers but has for the axial servo's current drivers.

The effects of this feedback has been determined numerically. Figure A-2(A) shows the effect of increasing  $R_F$ ; the voltage feedback resistor, from zero to infinity with the feedback capacitor  $C$  held at .01  $\mu\text{f}$ . If only the capacitor is used for voltage feedback, the current driver roots are still lightly damped but at a much lower frequency. As the resistance is increased the roots increase in damping, become real, then decrease in damping at a high frequency, finally moving to the no voltage feedback position for  $R_F = \infty$ . Figure A-2(B) shows the effect of increasing the voltage feedback capacitor  $C$  from zero to infinity while holding the feedback resistor at one megohm. For  $C = 0$ , the roots start at the no voltage feedback position. As  $C$  is increased the roots decrease in frequency and increase in damping ratio until  $C = .00091 \mu\text{f}$ . Further increases result in decreased damping ratio and increased frequency. At the chosen voltage feedback values of  $C = .01 \mu\text{f}$ ,  $R_F = 1.0 \text{ M}\Omega$ , the axial current driver transfer function is

$$\frac{I}{V} = \frac{.0008994(S+83.3)(S+1.099E11)}{(S+78.6)(S+2771 \pm j2583)}$$

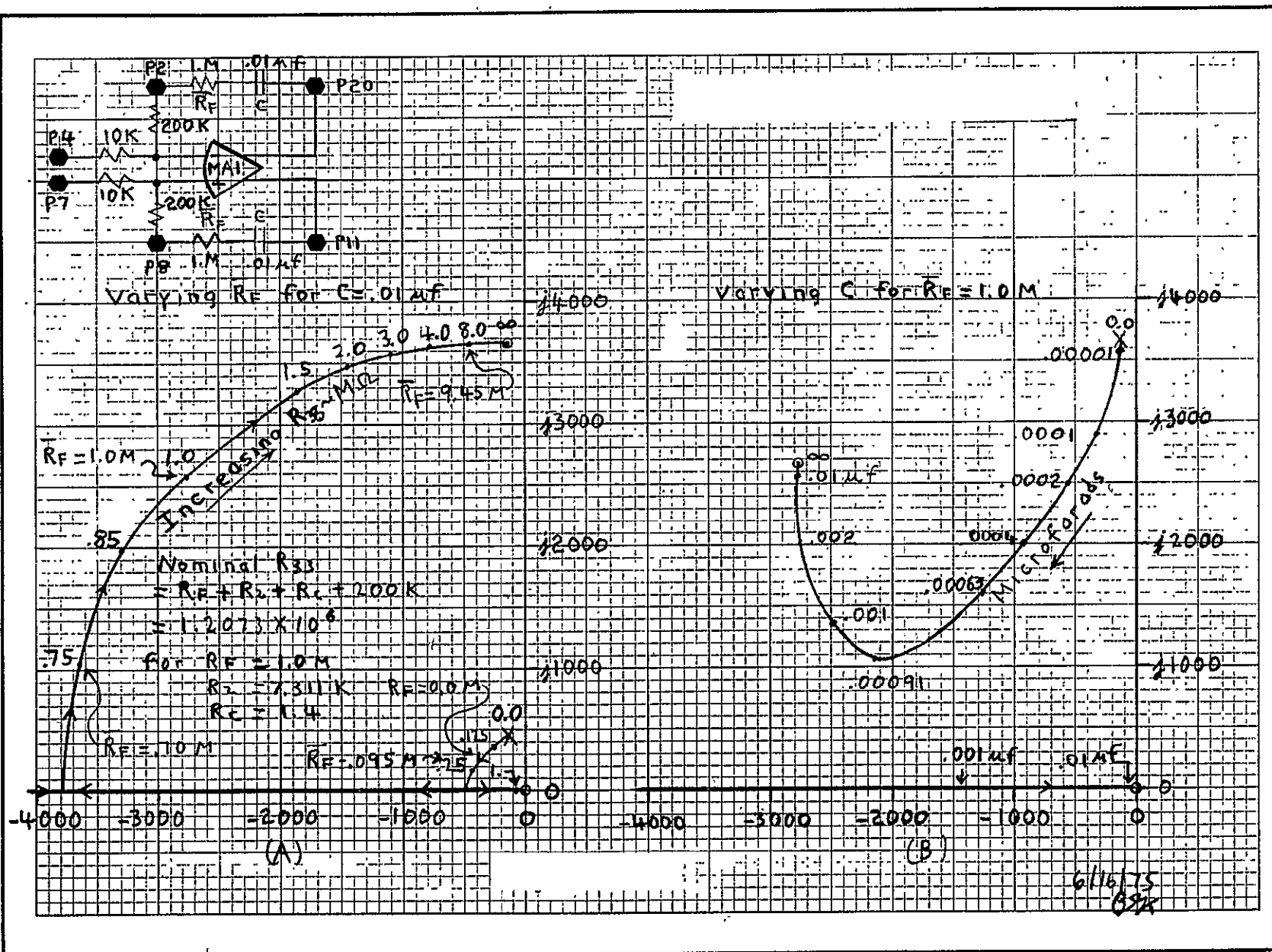


Figure A-2 Effect of Voltage Feedback on AMCD Axial Current Driver



F76-02 -

APPENDIX B  
THE WAHOO CONCEPT



## Appendix B

### The WAHOO Concept

#### Introduction

Two conditions may occur which cause the radial electromagnets to draw more current than necessary. First, if the rim is tipped, a gravitational force tends to pull the rim sideways. This force is countered by the servos at the expense of causing the electromagnets to draw more current. Second, as the rim spins up, centrifugal forces cause it to expand. To each radial sensor, this expansion is viewed as rim movement to be countered by the servos. So, each electromagnet draws more current to try to pull the rim inward. But since the forces are all directed inward and spaced  $120^\circ$  around the rim, the resultant of the forces is zero so the rim does not move. The net result of the expansion then is that only the current in the electromagnets increases. Trim loops are developed in this appendix which lead to VZP (Virtually Zero Power) operation for the radial servos when either the rim is tipped or expands or both. The system employing these trim loops is called the WAHOO system.

Because the three radial servos are controlling only two degrees of freedom, the radial servo system is very highly coupled. This very high degree of coupling makes it difficult to design each servo as a single uncoupled system. Hence, in this appendix we also develop equations to show how the three-servo radial system may be designed using a single station servo radial equivalent.

#### Development of the WAHOO Concept

The AMCD rim is suspended radially by three servos pulling on it from the inside much like shown in Figure B-1.



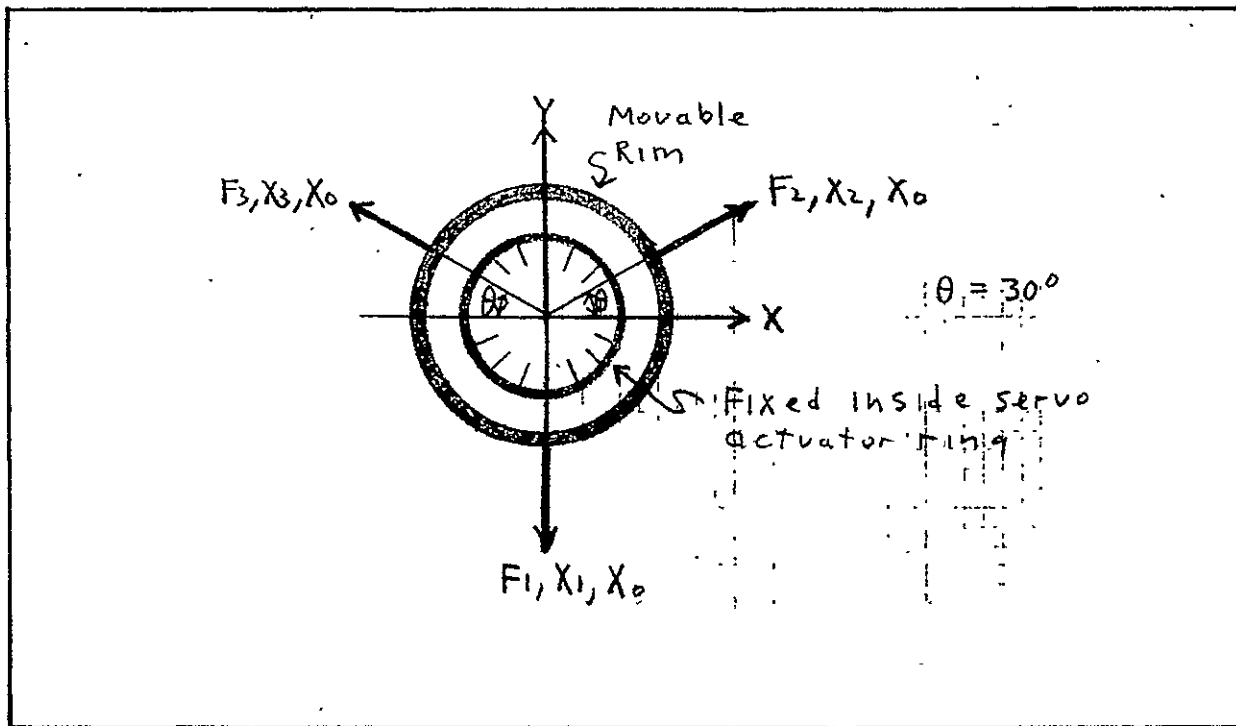


Figure B-1 Radial Servo Sign Convention

The sensor outputs are denoted by  $X_1$ ,  $X_2$ , and  $X_3$ . As the rim spins up, it expands by the amount  $X_0$ . The sign convention is chosen such that positive forces and displacements are outwards. The equations of motion of the rim are:

$$(F_2 - F_3)C\theta = M\ddot{X}$$

$$(F_2 + F_3)S\theta - F_1 = M\ddot{Y}$$

$$X_2 = XC\theta + YS\theta$$

$$X_3 = -XC\theta + YS\theta$$

$$X_1 = -Y$$

(B-1)



The force acting at each station is composed of a permanent magnet force and an electromagnet force. That is:

$$\begin{aligned} F_1 &= P(X_1 + X_0) + E D_1 \\ F_2 &= P(X_2 + X_0) + E D_2 \\ F_3 &= P(X_3 + X_0) + E D_3 \end{aligned} \quad (B-2)$$

These equations are combined with the servo equations in Figure B-2.

From the block diagram, the equations of motion using five variables are:

$$\begin{aligned} V_1 &= K_P(-Y + X_0) - (1/S)(K_S V_1 + K_C V_2 + K_C V_3) \\ \ddot{Y} &= M^{-1} \left\{ -P(-Y + X_0) + \frac{EK_R N}{D}(-Y + X_0) + EV_1 + PS\theta(YS\theta + XC\theta + X_0) \right. \\ &\quad - \frac{EK_R N}{D} S\theta(YS\theta + XC\theta + X_0) - ES\theta V_2 + PS\theta(YS\theta - XC\theta + X_0) \\ &\quad \left. - \frac{EK_R N}{D} S\theta(YS\theta - XC\theta + X_0) - ES\theta V_3 + F_Y \right\} \\ V_2 &= K_P(YS\theta + XC\theta + X_0) - (1/S)(K_S V_2 + K_C V_1 + K_C V_3) \\ \ddot{X} &= M^{-1} \left\{ PC\theta(YS\theta + XC\theta + X_0) - \frac{EK_R N}{D} C\theta(YS\theta + XC\theta + X_0) - EC\theta V_2 \right. \\ &\quad \left. - PC\theta(YS\theta - XC\theta + X_0) + \frac{EK_R N}{D} C\theta(YS\theta - XC\theta + X_0) + EC\theta V_3 \right\} \\ V_3 &= K_P(YS\theta - XC\theta + X_0) - (1/S)(K_S V_3 + K_C V_1 + K_C V_2) \end{aligned} \quad (B-3)$$

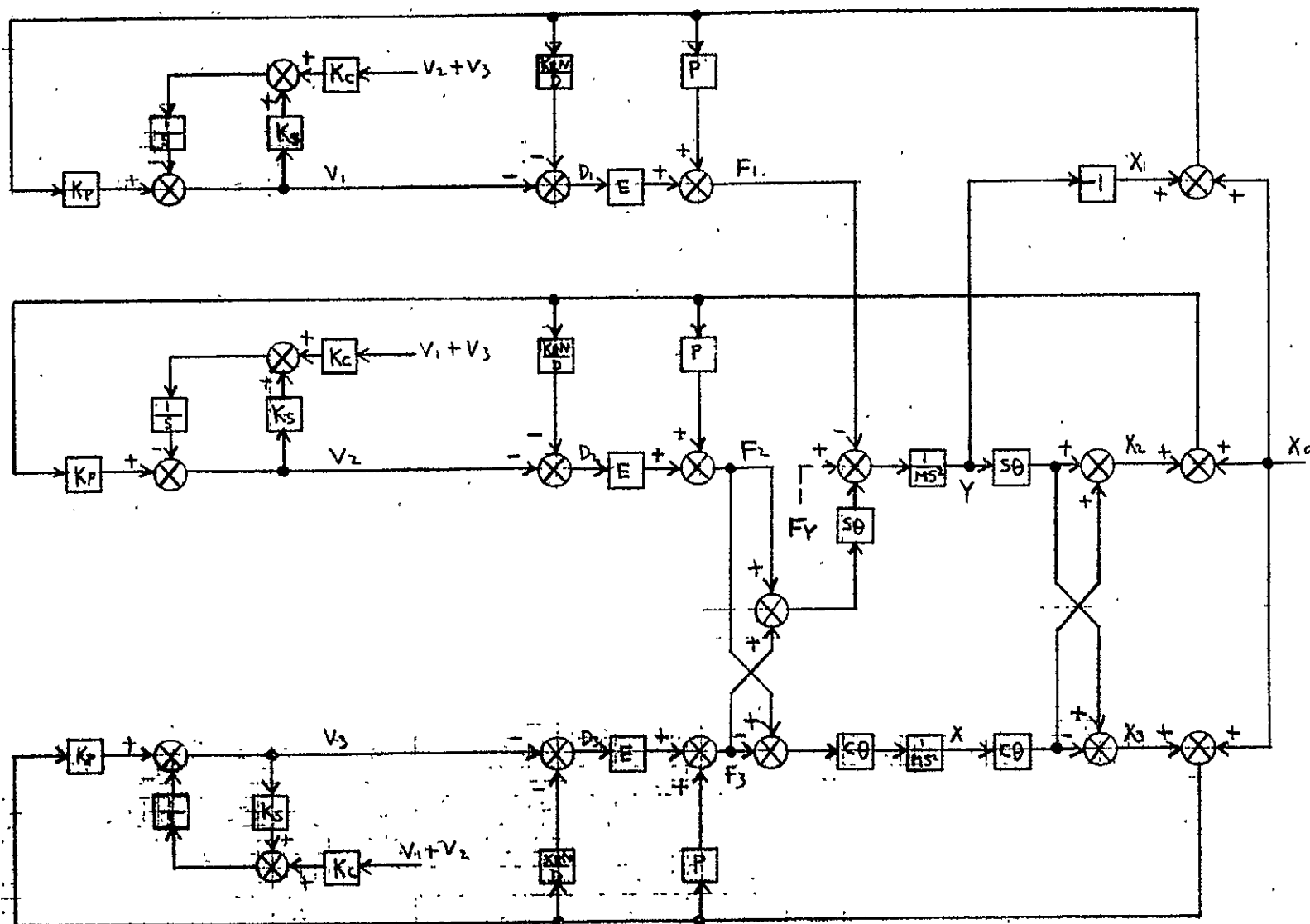
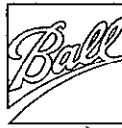


Figure B-2 AMCD Radial Servos With Trim Loops!



Rearranging,

- $(S+K_S)V_1 + K_P SY + K_C V_2 + K_C V_3 = K_P SX_0$
- $-M^{-1}DEV_1 + [DS^2 - DM^{-1}P(1+2S^2\theta) + M^{-1}EK_R N(1+2S^2\theta)]Y$   
 $+M^{-1}DES\theta V_2 + M^{-1}DES\theta V_3 = [M^{-1}DP(-1+2S\theta) + M^{-1}EK_R N(1-2S\theta)]X_0 + M^{-1}DF_Y$
- $K_C V_1 - K_P S\theta SY + (S+K_S)V_2 - K_P C\theta SX + K_C V_3 = K_P SX_0$
- $M^{-1}DEC\theta V_2 + [DS^2 - DM^{-1}P(2C^2\theta) + M^{-1}EK_R N(2C^2\theta)]X - M^{-1}DEC\theta V_3 = 0$
- $K_C V_1 - K_P S\theta SY + K_C V_2 + K_P C\theta SX + (S+K_S)V_3 = K_P SX_0$  (B-4)

Since  $\theta = 30^\circ$

$$1+2S^2\theta = 1+2(.5)^2 = 1.5$$

$$-1+2S\theta = -1+2(.5) = 0$$

$$2C^2\theta = 2\left(\frac{\sqrt{3}}{2}\right)^2 = 1.5$$
 (B-5)

Using these simplifications, the Laplace transformed radial servo equations of motion in matrix form are:

|             |                                      |                      |                                      |                       |       |         |           |
|-------------|--------------------------------------|----------------------|--------------------------------------|-----------------------|-------|---------|-----------|
| $(S+K_S)$   | $K_P S$                              | $K_C$                | 0                                    | $K_C$                 | $V_1$ | $K_P S$ | 0         |
| $-M^{-1}DE$ | $+1.5M^{-1}EK_R N$<br>$-1.5M^{-1}DP$ | $.5M^{-1}DE$         | 0                                    | $.5M^{-1}DE$          | Y     | 0       | $M^{-1}D$ |
| $K_C$       | $-.5K_P S$                           | $(S+K_S)$            | $-.5\sqrt{3} K_P S$                  | $K_C$                 | $V_2$ | $K_P S$ | 0         |
| 0           | 0                                    | $.5\sqrt{3}M^{-1}DE$ | $+1.5M^{-1}EK_R N$<br>$-1.5M^{-1}DP$ | $-.5\sqrt{3}M^{-1}DE$ | X     | 0       | 0         |
| $K_C$       | $-.5K_P S$                           | $K_C$                | $.5\sqrt{3} K_P S$                   | $(S+K_S)$             | $V_3$ | $K_P S$ | 0         |

$$= X_0 + F_Y$$



The system characteristic equation is the determinant of the coefficient matrix. With much algebraic effort, it can be reduced to

$$\Delta = (S+K_S+2K_C)X$$

$$[(S+K_S-K_C)(DS^2+1.5M^{-1}EK_RN-1.5M^{-1}DP)+1.5K_P M^{-1}DES]^2 \quad (B-7)$$

Now, let's simplify the expression by removing the high frequency roots. In the Cambion hardware.

$$\frac{K_R N}{D} = \frac{10^7 S}{(S+1000)(S+10000)} \approx S \text{ for low frequencies}$$

With this approximation  $K_R = D = 1$  and  $N = S$ . Then,

$$\Delta = (S+K_S+2K_C)[(S+K_S-K_C)(S^2+1.5M^{-1}ES-1.5M^{-1}P)+1.5K_P M^{-1}ES]^2$$

So the roots separate into  $-(K_S+2K_C)$  and two identical sets within the brackets. Immediately, we see that  $K_S+2K_C \geq 0$  for stability. Now looking within the brackets, we see that  $S^2+1.5M^{-1}ES-1.5M^{-1}P$  represents the permanent magnet roots at  $\pm\sqrt{1.5M^{-1}P}$  moved to the left some by the rate feedback; however one remains in the right half plane. Taking these roots and the one at  $-(K_S-K_C)$  as poles of a root locus plot and  $S$  as the zero, Figure B-3 shows that for stability  $K_C \geq K_S$ .

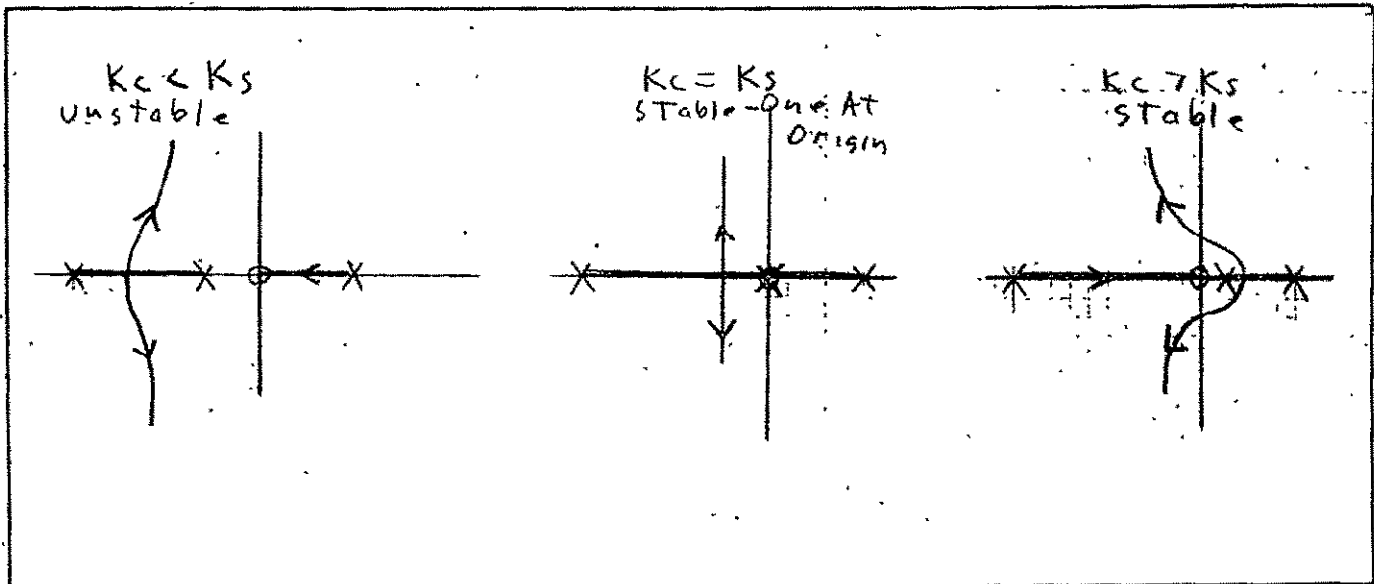


Figure B-3 Effect of Trim Loop Gains

Let's look at three special cases:

I. No Trim Loop:  $K_C = K_S = 0$  : No VZP

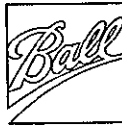
$$\Delta = S^3 [(S^2 + 1.5M^{-1}ES - 1.5M^{-1}P) + 1.5K_P M^{-1}E]^2 \quad (B-8)$$

There are three roots at the origin from the three unconnected integrators and two identical quadratic pairs. The system is stable.

II. No Cross Feed Trims:  $K_C = 0$

$$\Delta = (S + K_S) [(S + K_S) (S^2 + 1.5M^{-1}ES - 1.5M^{-1}P) + 1.5K_P M^{-1}ES]^2 \quad (B-9)$$

This is unstable for both signs of  $K_S$  ∴ self trim loops alone will not work.



III. No Self Feed Trim:  $K_S = 0$  : WAHOO SERVO

$$\Delta = (S+2K_C) [(S-K_C)(S^2+1.5M^{-1}ES-1.5M^{-1}P)+1.5K_P M^{-1}ES]^2$$

This can be made stable for all positive values of  $K_C$ .

IV. One Integrator Trim:  $K_C = K_S \triangleq K$

$$\Delta = (S+3K)S^2 [(S^2+1.5M^{-1}ES-1.5M^{-1}P)+1.5K_P M^{-1}E]^2 \quad (B-10)$$

This can be made stable for all positive values of  $K$ .

- Main conclusion to here: Cross Feed is necessary for stability if VZP is needed.  
Self Feed is not.

Now a question arises. Do the two stable systems (III and IV) provide zero power operation in the face of both rim expansion and force disturbances and do they translate due to these effects? To answer this, look at the transfer function  $V_1/X_0$ ,  $V_1/F_y$ ,  $Y/X_0$ , and  $Y/F_y$ . From (B-6), after much algebraic manipulation, we obtain the numerators:

$$\text{Num } (V_1/X_0) = K_P S [(S+K_S-K_C)(DS^2+1.5M^{-1}EK_R N-1.5M^{-1}DP)+1.5K_P M^{-1}DES]^2 \quad (B-11)$$

$$\begin{aligned} \text{Num } (V_1/F_y) = & -M^{-1}DK_P S(S+K_S+2K_C)X \\ & [(S+K_S-K_C)(DS^2+1.5M^{-1}EK_R N-1.5M^{-1}DP)+1.5K_P M^{-1}DES] \end{aligned} \quad (B-12)$$



$$\text{Num } (Y/X_0) = 0 \quad (\text{B-13})$$

$$\begin{aligned} \text{Num } (Y/F_y) &= M^{-1}D(S+K_S+2K_C)(S+K_S-K_C)X \\ &\quad [(S+K_S-K_C)(DS^2+1.5M^{-1}EK_RN-1.5M^{-1}DP)+1.5K_P M^{-1}DES] \end{aligned} \quad (\text{B-14})$$

Repeating (B-7)

$$\Delta = (S+K_S+2K_C) [(S+K_S-K_C)(DS^2+1.5M^{-1}EK_RN-1.5M^{-1}DP)+1.5K_P M^{-1}DES]^2 \quad (\text{B-7})$$

Then the transfer functions are

$$\frac{V_1}{X_0} = \frac{\text{Num } (V_1/X_0)}{\Delta} = \frac{K_P S}{(S+K_S+2K_C)} \quad (\text{B-15})$$

$$\frac{V_1}{F_y} = \frac{\text{Num } (V_1/F_y)}{\Delta} = \frac{-M^{-1}DK_P S}{(S+K_S-K_C)(DS^2+1.5M^{-1}EK_RN-1.5M^{-1}DP)+1.5K_P M^{-1}DES} \quad (\text{B-16})$$

$$\frac{Y}{X_0} = \frac{\text{Num } (Y/X_0)}{\Delta} = 0 \quad (\text{B-17})$$





$$\frac{Y}{F_y} = \frac{M^{-1}D(S+K_S-K_C)}{(S+K_S-K_C)(DS^2+1.5M^{-1}EK_RN-1.5M^{-1}DP)+1.5K_P M^{-1}DES} \quad (B-18)$$

Now we can answer the question.

- WAHOO Servo:  $K_S = 0$

Because of the  $S$  in the numerators of  $V_1/X_0$  and  $V_1/F_y$  the steady state power goes to zero for both rim expansion and force disturbances. From  $Y/X_0$ , the rim does not translate for rim expansion. From  $Y/F_y$ , the rim does translate for disturbance forces with a stiffness of

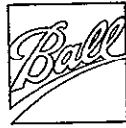
$$\left. \frac{F_y}{Y} \right|_{S=0} = -1.5P \quad (B-19)$$

Therefore, the rim translates toward the disturbance.

- Single Integrator Trim:  $K_C = K_S$

From  $V_1/X_0$ , the steady-state power goes to zero for rim expansion. With  $K_C = K_S$ , the  $S$  cancels out of the numerator of  $V_1/F_y$ ; therefore, the system power is not zero for force disturbances. From  $Y/X_0$ , the system does not translate for rim expansion. From  $Y/F_y$ , the rim does translate for force disturbances with a stiffness of

$$\left. \frac{F_y}{Y} \right|_{S=0} = 1.5(K_P E - P) \quad (B-20)$$



Therefore, the rim translates away from the disturbances with the same stiffness it has with no trim.

### Radial Single Station Servo Equivalent

Because three servos are controlling only two degrees of freedom, the radial servo system is very highly coupled. This makes it difficult to design each servo as a single uncoupled system. From the characteristic equation  $\Delta=0$  derived in the preceding section we may deduce a single station equivalent. From (B-7), considering only the WAHOO servo,

$$\Delta = (S+2K_C) [(S-K_C)(DS^2+1.5M^{-1}EK_RN-1.5M^{-1}DP)+1.5K_PM^{-1}DES]^2 \quad (B-21)$$

We note that there is one root at  $-2K_C$  and a repeated set of roots within the brackets. We would expect only two repeated sets because we are only controlling two degrees of freedom even though three servos are used to accomplish it. Looking at the quantity within the brackets

$$(S-K_C)(DS^2+1.5M^{-1}EK_RN-1.5M^{-1}DP)+1.5K_PM^{-1}DES = 0 \quad (B-22)$$

we first divide through by  $S^2D(S-K_C)$  to obtain

$$1 + \frac{E}{2/3 M} \frac{K_R N}{DS^2} - \frac{P}{2/3 MS^2} + \frac{K_P E}{2/3 MS^2} \frac{S}{S-K_C} = 0 \quad (B-23)$$



This is just the characteristic equation of the following servo, which is the single station equivalent.

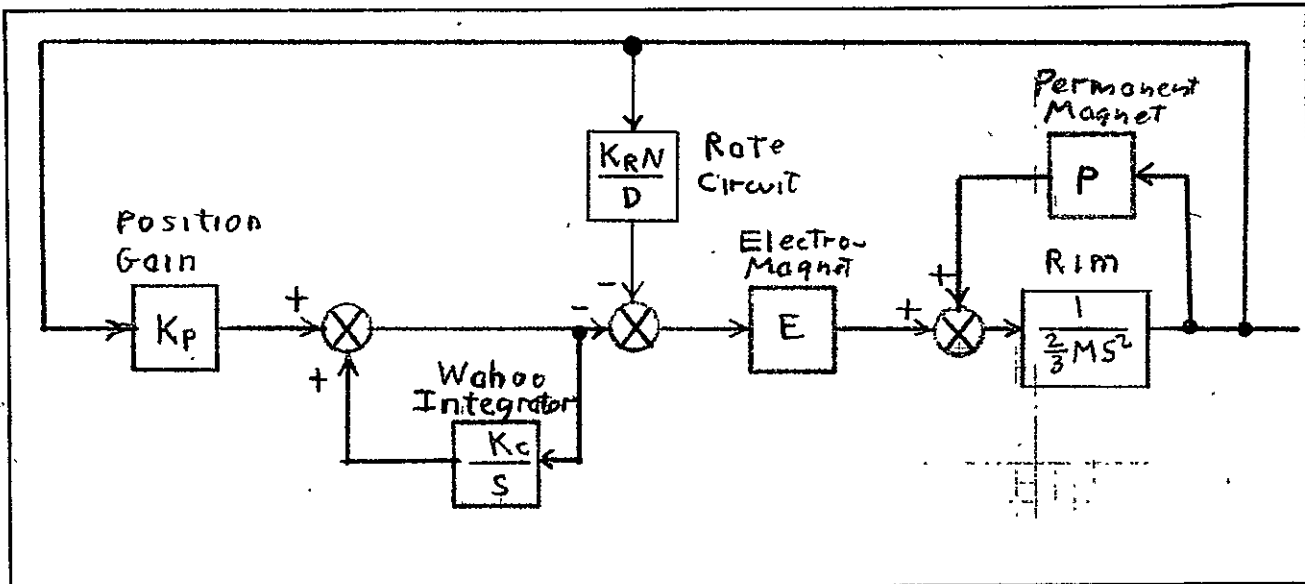
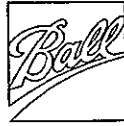


Figure B-4 Equivalent Single Radial Servo Station

Two points of interest are immediately evident. The equivalent mass is  $2/3$  the total rim mass. The WAHOO concept which involves negative feedback to each station from the sum of the other two stations resolves to a positive feedback in the single station representation exactly like VZP in the axial mode. Using this single station equivalent, the system may be designed just like an uncoupled servo, the final three-servo coupled system roots being given by (B-21).

### Conclusions

- Only the WAHOO trim system is stable and produces zero steady-state power for both force disturbances and rim expansion. WAHOO trim consists of the sum of voltages from servos  $i$  and  $j$  being fed back to servo  $k$  in a negative sense for each  $i$ ,  $j$ , and  $k$ . That is, for trim purposes, each servo only monitors what the other two are doing-not itself. The system stiffness is  $-1.5P$  where  $P$  is the permanent magnet stiffness at each station.



. F76-02

- The highly coupled three servo radial systems may be designed using a single station servo radial equivalent.



F76-02

APPENDIX C  
SOME ADDITIONAL SERVO INSIGHTS



## Appendix C

### Some Additional Servo Insights

The purpose of this appendix is to provide additional insight into the inner workings of the system. To build up a feel for the final axial system, a series of stability plots are shown to show the state of the system at various stages of its design.

The axial servos were originally designed assuming an ideal current driver, that is, one whose output current is just a constant times the input voltage. This is what is usually assumed concerning current drivers. Figure C-1 is the axial position mode root locus plot of such a system. It indicates that no stability problems exist, an upper gain margin of 120.6 and a lower gain margin of .22 being evident. The actual servo did not exhibit such stability.

Figure C-2 shows the same root locus plot (that is, axial position mode) if a realistic current driver is used. The realistic current driver has low damped ( $\zeta = .036$ ) high frequency roots ( $\omega = 3685$  rad/sec) which are driven unstable at a gain of 4.79 (compared with 120.6 above). The actual servo exhibited this instability at even lower gain margins. At the times we were experiencing this instability, the root locus plot of Figure C-2 had not been made. Indeed, the realistic current driver transfer function had not even been derived. We did, however, suspect the current driver and fixed the problem experimentally by trying different values of components in the voltage feedback circuit. We eventually arrived at  $C = .01 \mu\text{f}$  and  $R_F = 1.0 \text{ M}\Omega$  for feedback components. Appendix A shows that this was a near optimum choice. Figure 4-10 shows that this fix increased the systems upper gain margin from 4.79 to 20.1.



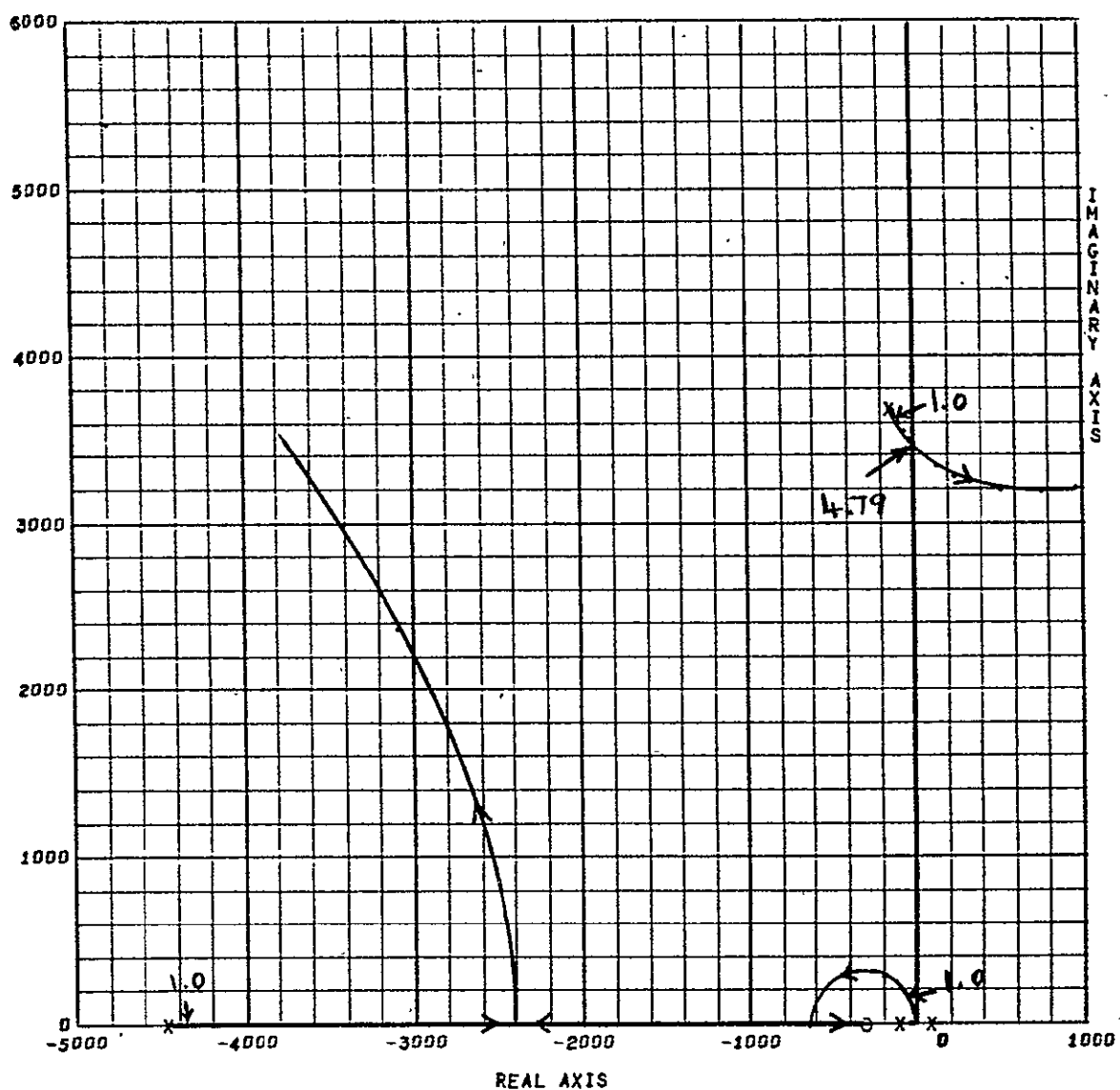


Figure C-2 Root Locus Plot Nonideal Current Driver Without Voltage Feedback



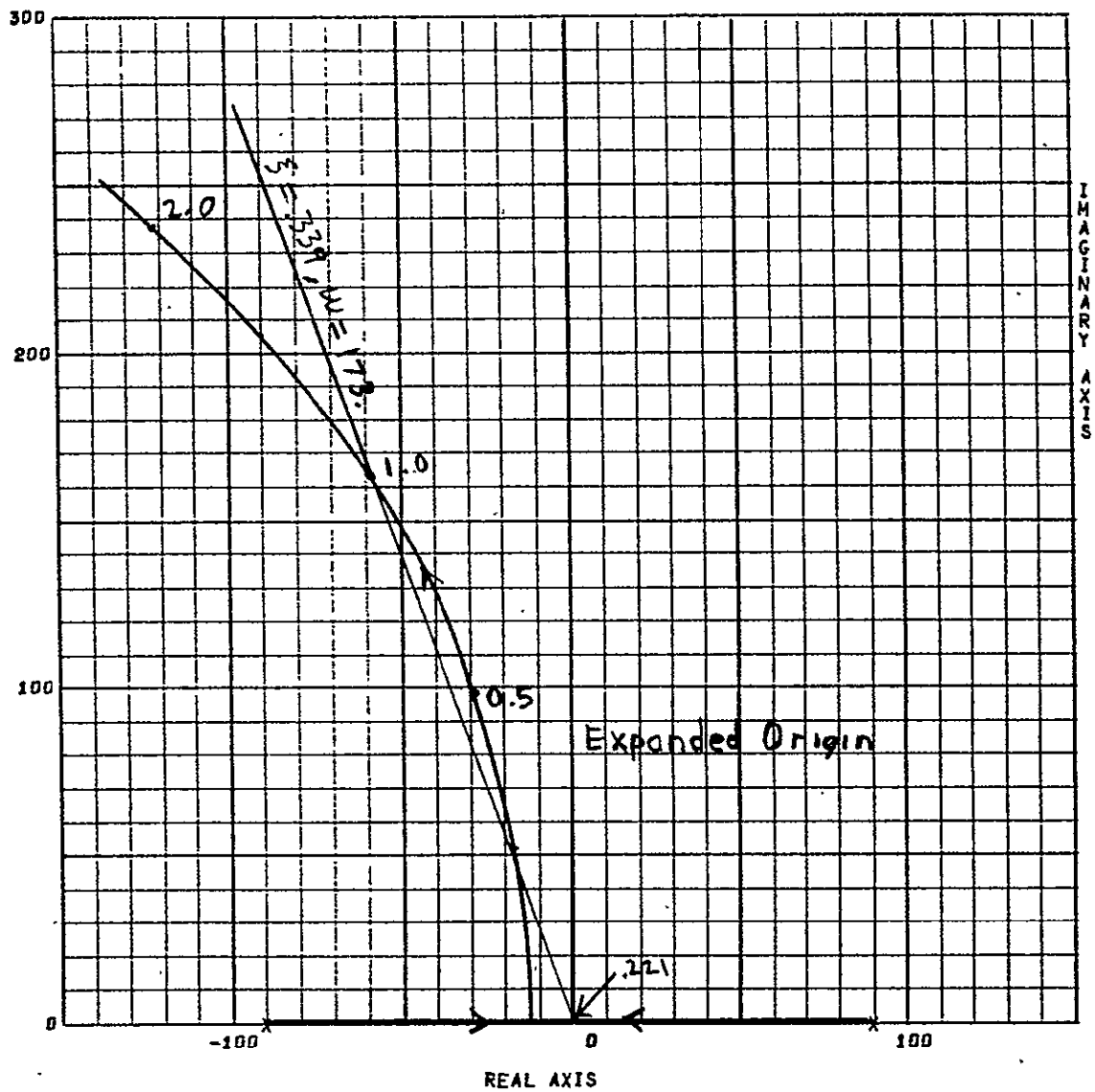
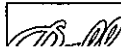


Figure C-2(B) Root Locus Plot - Nonideal Current Driver Without Voltage Feedback



The final axial system root locus and Bode plots are shown in Figures 4-10 and 4-11 for the position mode and in Figures 4-12 and 4-13 for the VZP mode. Sometimes, additional insight may be obtained from other stability plots. The axial position mode and VZP mode Nyquist plots are shown in Figures C-3 and C-4. A plot which yields root sensitivity information from both changes in gain and phase is the gain phase root locus plot. Gain-phase root locus plots for the axial position and VZP modes appears in Figures C-5 and C-6. For example, Figure C-5 reveals that if the gain remained nominal and for some unknown reason an additional  $23.2^\circ$  of phase lag were introduced, the axial position mode would go unstable.

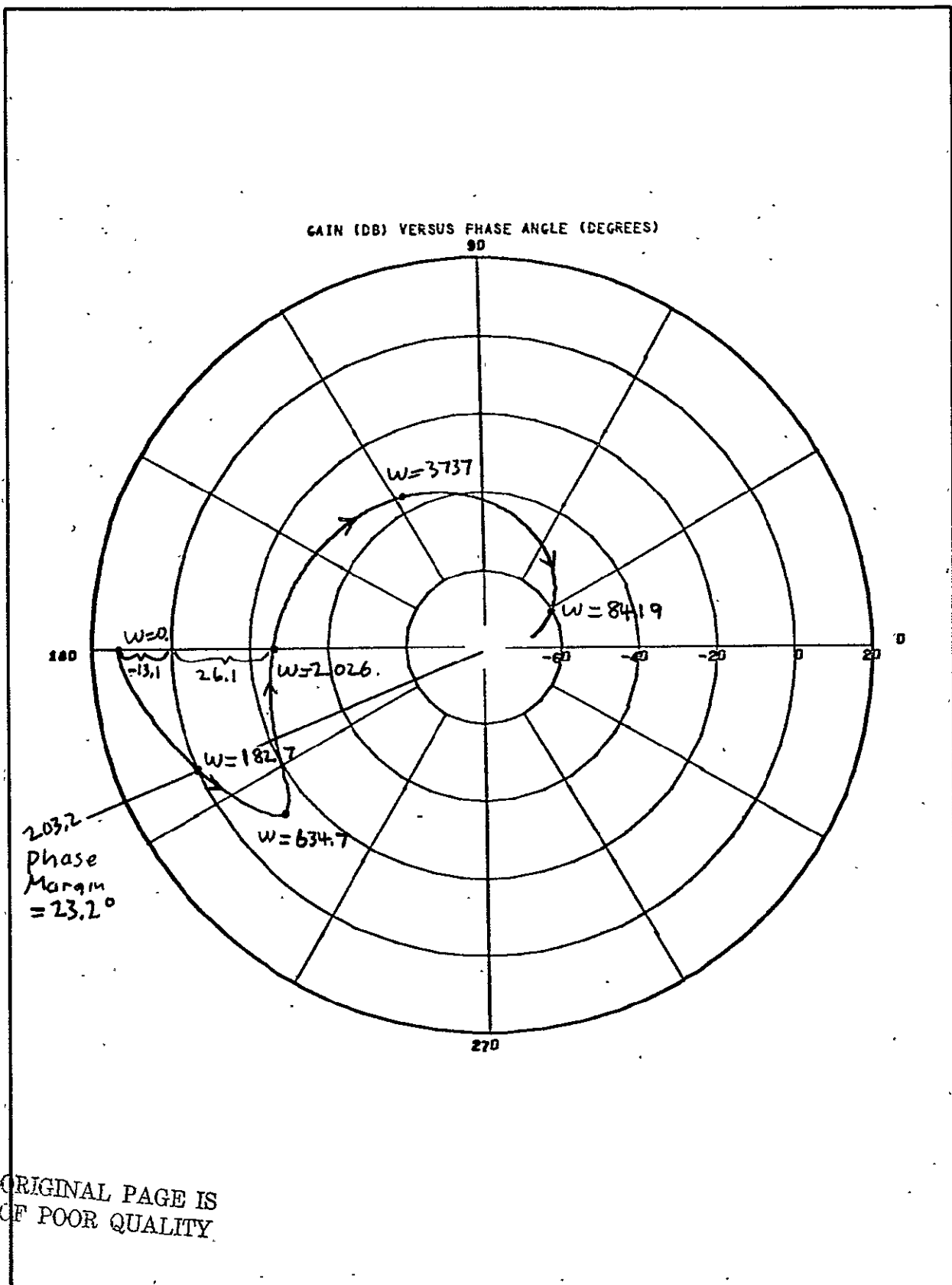
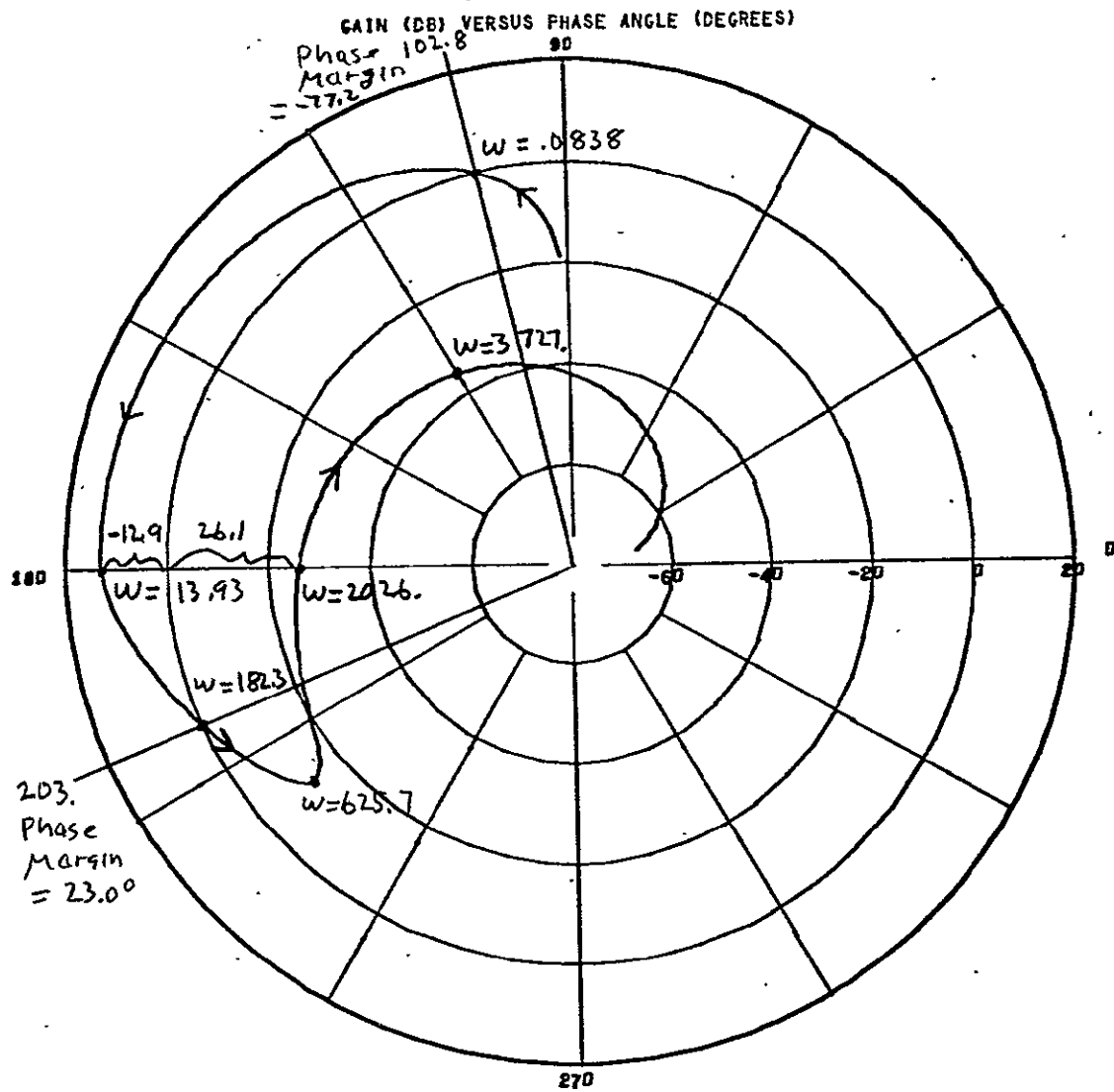


Figure C-3 Nyquist Plot - Nonideal Current Driver With Voltage Feedback



ORIGINAL PAGE IS  
OF POOR QUALITY

Figure C-4 Nyquist Plot - Nonideal Current Driver With  
Voltage Feedback

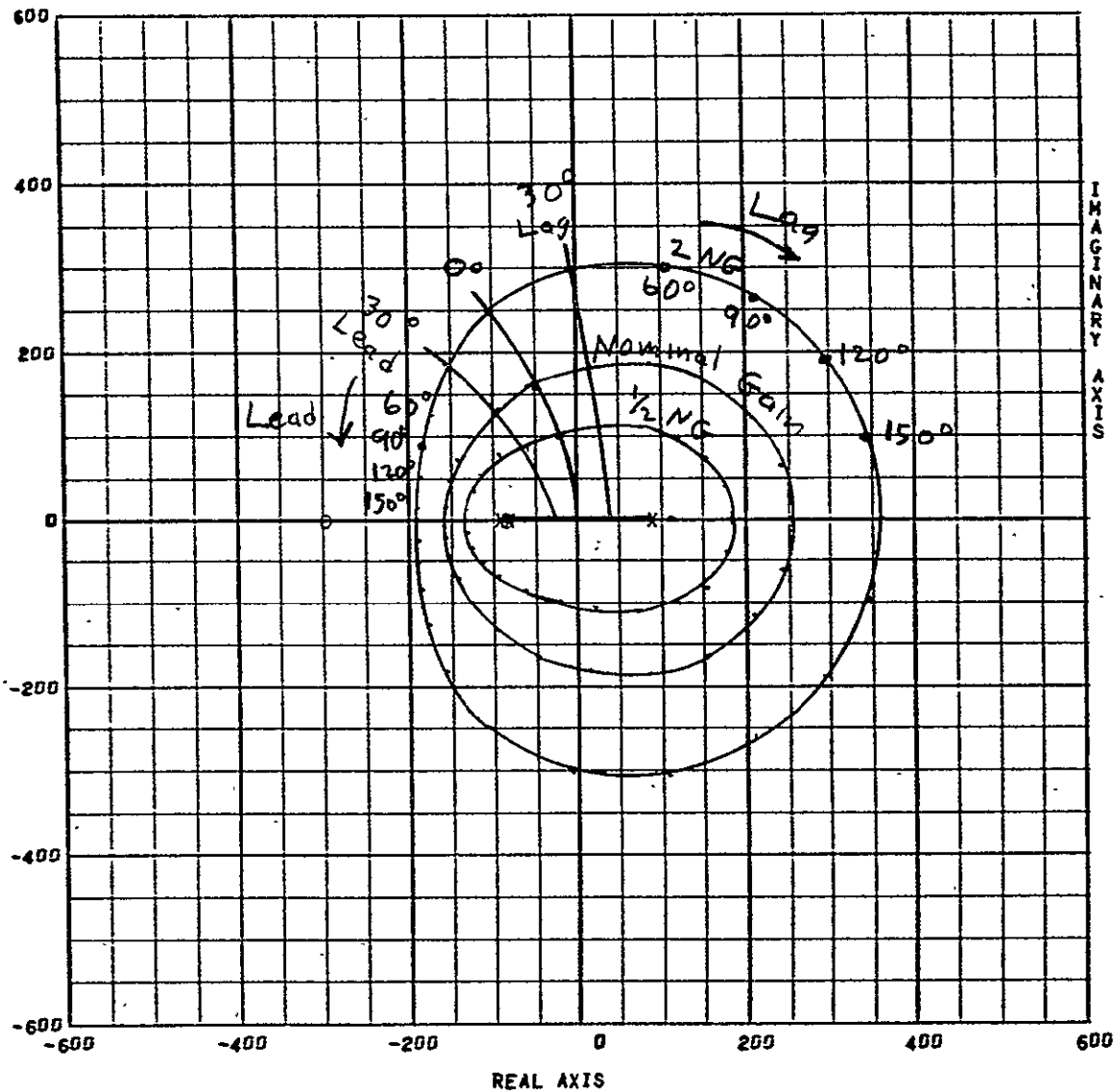


Figure C-5 Gain-Phase Root Locus Plot - Nonideal Current Driver With Voltage Feedback

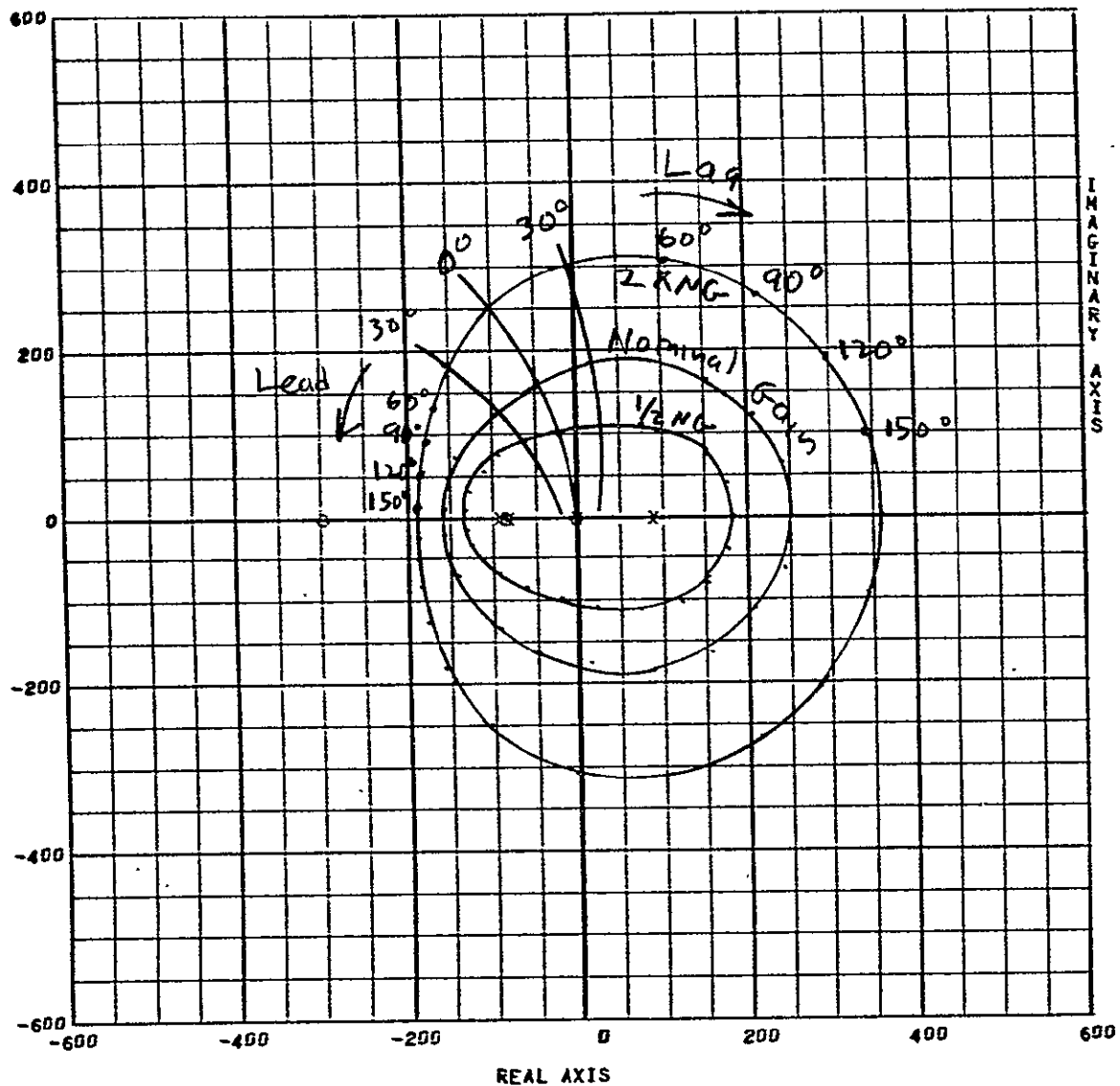


Figure C-6 Gain-Phase Root Locus Plot - Nonideal Current Driver With Voltage Feedback